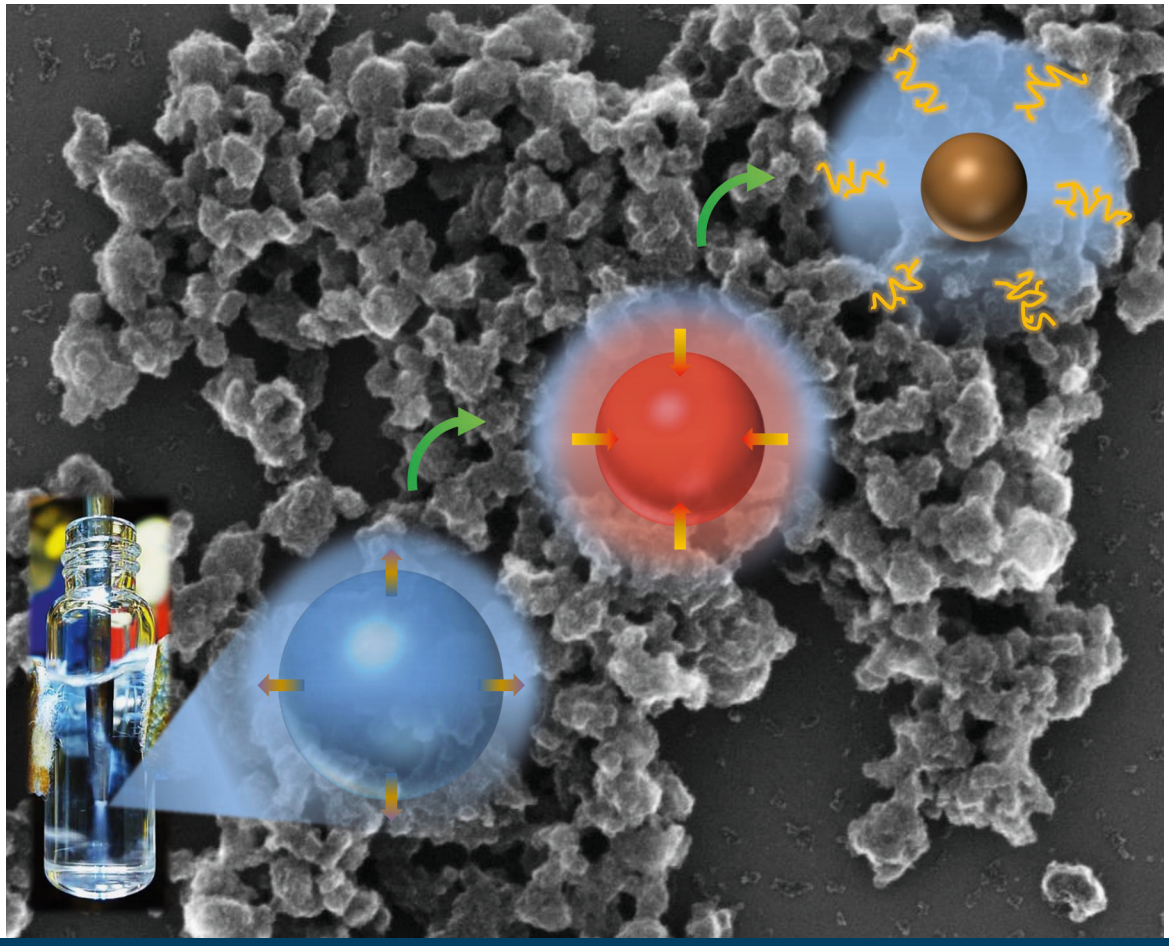

Sonochemical Synthesis of Silicon Hydride Polymers and Silicon Nanoparticles from Liquid Silanes

Andrew Paolo Cádiz Bedini

Energie & Umwelt / Energy & Environment
Band / Volume 423
ISBN 978-3-95806-329-7

Mitglied der Helmholtz-Gemeinschaft

JÜLICH
Forschungszentrum

Schriften des Forschungszentrums Jülich
Reihe Energie & Umwelt / Energy & Environment Band / Volume 423

Forschungszentrum Jülich GmbH
Institut für Energie- und Klimaforschung
IEK-5 Photovoltaik

Sonochemical Synthesis of Silicon Hydride Polymers and Silicon Nanoparticles from Liquid Silanes

Andrew Paolo Cádiz Bedini

Schriften des Forschungszentrums Jülich
Reihe Energie & Umwelt / Energy & Environment Band / Volume 423

ISSN 1866-1793 ISBN 978-3-95806-329-7

Bibliografische Information der Deutschen Nationalbibliothek.
Die Deutsche Nationalbibliothek verzeichnet diese Publikation in der
Deutschen Nationalbibliografie; detaillierte Bibliografische Daten
sind im Internet über http://dnb.d-nb.de abrufbar.

Herausgeber und Vertrieb:	Forschungszentrum Jülich GmbH Zentralbibliothek, Verlag 52425 Jülich Tel.: +49 2461 61-5368 Fax: +49 2461 61-6103 zb-publikation@fz-juelich.de www.fz-juelich.de/zb
Umschlaggestaltung:	Grafische Medien, Forschungszentrum Jülich GmbH
Druck:	Grafische Medien, Forschungszentrum Jülich GmbH
Copyright:	Forschungszentrum Jülich 2018

Schriften des Forschungszentrums Jülich
Reihe Energie & Umwelt / Energy & Environment, Band / Volume 423

D 82 (Diss., RWTH Aachen, Univ., 2017)

ISSN 1866-1793
ISBN 978-3-95806-329-7

Vollständig frei verfügbar über das Publikationsportal des Forschungszentrums Jülich (JuSER)
unter www.fz-juelich.de/zb/openaccess.

In loving memory of a beautiful and gentle soul,

Carina Pullen (1988-2014)

Abstract

The present thesis is concerned with the use of ultrasound for the treatment of liquid silanes with the objective of fabricating solution-processable inks containing silicon hydride polymers and silicon nanoparticles. Also demonstrated is the subsequent use of the inks to deposit semiconducting hydrogenated amorphous silicon (a-Si:H) thin films and for fabricating passivation layers and thin-film photovoltaic devices.

The sonochemical effects of ultrasound on two lower silanes, namely cyclopentasilane (Si_5H_{10}) and trisilane (Si_3H_8) were studied. The processing of the silanes was carried out in the inert N_2-atmosphere and in solution using cyclooctane (C_8H_{16}) as solvent at ambient pressure, and at temperatures between −15–70 °C.

Using cyclopentasilane as monomer molecule it was shown via size exclusion chromatography and optical transmission measurements that sonication of 8–15 wt% solutions results in ring-opening polymerization without the need to use ultraviolet light. In addition, through comparisons to purely thermally treated solutions it was demonstrated that the polymerization process is not initiated pyrolytically due to the "macroscopic" temperature of the solution itself, but rather that microscopic effects associated with acoustic cavitation are most likely responsible for triggering polymer growth.

The sonication of trisilane solutions was found to result in the production of two primary silicon-containing species. Firstly, using gas chromatography-mass spectrometry it was shown that ultrasonic treatment produced higher order branched and linear silanes from tetrasilane (Si_4H_{10}) to octasilane (Si_8H_{18}). Secondly, ultrasound was found to produce silicon nanoparticles. Electron microscopy techniques

(SEM, TEM, and STEM) were used to acquire images of the particles and demonstrate size variability in the range ca. 1.5–50 nm via variation of the sonication conditions. Spectroscopic techniques such as Fourier transform infrared spectroscopy, Raman scattering, and x-ray photoelectron spectroscopy were used to ascertain that the particles are amorphous, hydrogenated, unoxidised and composed of solely of hydrogen and silicon. It was additionally revealed that irradiation of sonicated trisilane solutions with ultraviolet light produces useful amounts of a branched higher silicon hydride polymer.

The resulting solutions prepared from both cyclopentasilane and trisilane were subsequently used to deposit a-Si:H thin films. The optoelectronic and morphological properties of the layers, such as photosensitivity and microstructure, were improved via post-depositional hot-wire hydrogen radical treatment. Using inks derived from trisilane, layers deposited via spin coating and atmospheric-pressure chemical vapour deposition (APCVD) were implemented as intrinsic absorber layers in n-i-p type thin-film solar cells exhibiting efficiencies of 0.49 % and 3.41 %, respectively. Furthermore, APCVD films were used as surface defect passivation layers on both sides of a crystalline silicon wafer resulting in effective minority carrier lifetimes exceeding 400 µs.

Kurzfassung

Die vorliegende Arbeit beschäftigt sich mit der Verwendung von Ultraschall zur Behandlung von flüssigen Silanen mit dem Ziel, lösungsverarbeitbare Tinten bestehend aus Siliziumhydridpolymeren und Silizium-Nanopartikeln herzustellen. Darüber hinaus wird die nachfolgende Verwendung solcher Tinten für die Abscheidung von Halbleiter-Dünnschichten aus hydrogeniertem amorphen Silizium (a-Si:H) und die Herstellung von Passivierungsschichten und Dünnschichtsolarzellen demonstriert.

Die sonochemische Wirkung von Ultraschall auf zwei niedere Silane, namentlich Cyclopentasilan (Si_5H_{10}) und Trisilan (Si_3H_8) wurden untersucht. Die Verarbeitung der Silane wurde in inerter N_2-Atmosphäre bei Umgebungsdruck unter Verwendung von Cyclooctan (C_8H_{16}) als Lösungsmittel und bei Temperaturen zwischen -15–$70\,^{\circ}C$ durchgeführt.

Mit Cyclopentasilan als Monomermolekül wurde durch optische Transmissionsmessungen und Gel-Permeations-Chromatographie gezeigt, dass die Beschallung von 8–15 Gew %en Lösungen zu einer ringöffnenden Polymerisation führt. Dieser Prozess ist ohne zusätzliches ultraviolettes Licht möglich. Darüber hinaus wird durch Vergleiche mit rein thermisch behandelten Lösungen nachgewiesen, dass die Polymerisation nicht pyrolytisch aufgrund der "makroskopischen" Temperatur der Lösung selbst ausgelöst wird. Vielmehr ist das Polymerwachstum wahrscheinlich durch einen mikroskopischen Effekt - der akustischen Kavitation - zu erklären.

Es wurde festgestellt, dass die Beschallung von Trisilanlösungen zur Herstellung von zwei primären siliziumhaltigen Spezies führt. Erstens wird mittels Gaschromatographie mit Massenspektrometrie-Kopplung gezeigt, dass die Ultraschallbehandlung verzweigte und lineare Silane höherer Ordnung von Tetrasilan (Si_4H_{10})

bis zu Octasilan (Si_8H_{18}) erzeugt. Zweitens wurde festgestellt, dass die Ultraschallbehandlung zur Bildung von Silizium-Nanopartikeln führt. Elektronenmikroskopie (REM, TEM und STEM) wurde verwendet, um Abbildungen der Partikel aufzunehmen. Hiermit konnte gezeigt werden, dass eine Variation der Beschallungsbedingungen zu Partikeln mit einstellbaren Größen im Bereich von ca. 1,5–50 nm führt. Spektroskopische Methoden wie Fourier-Transform-Infrarotspektroskopie, Raman-Streuung und Röntgenphotoelektronenspektroskopie wurden genutzt, um zu zeigen, dass die Nanopartikel amorph, hydriert, nicht oxidiert und nur aus Wasserstoff und Silizium bestehen. Es wurde zusätzlich gezeigt, dass die Bestrahlung mit ultraviolettem Licht von mit Ultraschall behandelten Trisilanlösungen nützliche Mengen eines verzweigten höheren Siliziumhydridpolymers erzeugt.

Die verschiedenen Lösungen, die sowohl aus Cyclopentasilan als auch Trisilan hergestellt wurden, wurden anschließend zur Abscheidung von a-Si:H Dünnschichten verwendet. Die optoelektronischen und morphologischen Eigenschaften der Schichten, wie Lichtempfindlichkeit und Mikrostruktur, wurden durch Heißdraht-Radikalbehandlung verbessert. Insbesondere konnten aus Trisilan hergestellte Tinten verwendet werden, um sowohl mittels Rotationsbeschichtung als auch chemischer Gasphasenabscheidung bei Atmosphärendruck (APCVD) intrinsische Absorberschichten für nip-Typ Si-Dünnschichtsolarzellen herzustellen. Diese Solarzellen erreichten Wirkungsgrade von 0,49 % bzw. 3,41 %. Darüber hinaus wurden APCVD-Schichten als Passivierungsschichten für Oberflächendefekte auf beiden Seiten eines kristallinen Siliziumwafers verwendet, welche zu effektiven Minoritätladungsträgerlebensdauern von mehr als 400 µs führte.

Contents

Chapter 1

Introduction

After oxygen, silicon is the second most abundant element in the Earth's crust, where it predominantly occurs as silicates in sand and rock. It is also found in countless man-made materials such as ceramics, glass, and silicones. However, of all its uses it is in its elemental form that silicon has made its greatest impact on modern society. After decades of intense scientific study and industrialisation silicon is now without a doubt the quintessential semiconductor and is indispensable in most electronic devices. As a result, silicon has become ubiquitous in our daily lives: from being the light absorber material in the solar cells powering our pocket calculators and homes, to its total pre-eminence in the field of computing—from transistor to display. In recent years silicon has also gained relevance in nanotechnology, where silicon nanoparticles have been applied as the basis of alternative anode materials in lithium-ion batteries [1–4], as luminescent markers and drug carriers in biomedical and cancer research [5–7], as well as in more fundamental work such as photoluminescence and quantum confinement studies [8–11].

Conventional manufacturing technologies based on processes involving silicon in its gaseous or solid states have been around for several decades and are by now well established. The liquid phase processing of silicon at ambient temperatures and pressures, however, is relatively new. Although silicon hydride compounds (otherwise known as silanes) have a rich and long-standing history beginning in the 1850's, it was not until 2006 that Shimoda and co-workers demonstrated that

a liquid silane, namely cyclopentasilane (Si_5H_{10}), could be used to fabricate thin-film transistors via solution-processing methods such as spin coating and inkjet printing [12]. In the intervening decade the Shimoda group and a number of other groups that quickly followed suit have not only applied different solution-processing techniques, but also different precursor molecules to fabricate, i.a. thin-film solar cells [13–15], thin-film transistors [16–18], surface passivation layers for c-Si wafers [19, 20], and patterned films via imprinting [21].

Some of the major disadvantages associated with the solution-processed silicon thin films demonstrated up to now, however, are the high cost and scant commercial availability of the precursor monomers. In addition, the syntheses are usually carried out in small laboratory-scale batches ($\sim 50\,g$ or less) where the production of solar-grade or semiconductor-grade material remains a laborious task. Moreover, certain multi-step monomer synthesis routes, such as that of cyclopentasilane have poor scalability and low inherent yields [14]. Such issues may have thus far hampered the commercial viability of solution-processed silicon.

With these issues in mind, the present work focuses on developing alternative methods for processing liquid silanes in an effort to avoid some of the existing challenges limiting progress beyond the state-of-the-art. The results include new pathways for the fabrication of solution-processable silicon polymer inks and silicon nanoparticles. The findings are centred around the use of ultrasound for the synthesis of three main silicon containing species, namely higher order silanes, silicon hydride polymers, and silicon nanoparticles. The method exploits the sonochemical effects that ensue upon the collapse of microbubbles generated via ultrasound as applied to solutions of cyclopentasilane and the as yet scantly investigated alternative precursor trisilane (Si_3H_8). The use of trisilane, as opposed to cyclopentasilane or other silanes studied in the literature, is significant because it constitutes a readily available and semiconductor-grade purity industrial product. Further details and more thorough discussions on the fundamentals of liquid silanes and associated processing and characterisation techniques can be found in *Chapters 2* and *3*.

The liquid silane methods described in this work are carried out at temperatures between -15 and $75\,°C$ in the inert atmosphere of a N_2-filled glove box.

Compared to gas phase chemical vapour deposition (CVD) techniques such as plasma enhanced CVD or hot-wire CVD, the ability to work at ambient pressure and under easily accessible experimental conditions is highly advantageous. The benefits include vacuum-free processing, no intricate electronics or equipment, and the syntheses are easily upscalable. These factors make solution-processed silicon a potentially viable technology for the production of low-cost functional optoelectronics, and energy generation and storage devices via well-known methods based on, e.g laser treatment and printing techniques.

Numerous and varied topics were dealt with in the research and, as a consequence, a rather extensive assortment of analytical techniques were used. The analytical methods employed in the characterisation of the inks include chromatographic and mass spectrometric techniques to characterise the growth and molecular mass of higher order silanes and silicon hydrides. Nuclear magnetic resonance was used for the determination of polymer structure. UV-visible transmission measurements were used to optically investigate changes of solutions subjected to sonication. Suspensions and thin films of silicon nanoparticles were analysed via a variety of spectroscopic methods which include x-ray photoelectron, photoluminescence, infrared, Raman, and electron energy loss spectroscopy. Scanning and transmission electron microscopy were used to analyse the morphology and size of silicon nanoparticles as well as nanoparticle agglomerates. Solid films of amorphous silicon were characterised with respect to their microstructure, absorption properties and hydrogen content using infrared and photothermal deflection spectroscopy. Electrical conductivity measurements both in the dark and under illumination are used to show the semiconducting properties of the films. JV curves acquired using a solar simulator are used to characterise the photovoltaic devices built using solution-processed intrinsic absorber layers. Finally, charge carrier lifetimes and surface recombination velocities are estimated from transient photoconductance measurements carried out on c-Si wafer substrates passivated with APCVD films. Details on these techniques and their experimental implementation can be found in *Chapter 3*.

The results of the research are presented in *Chapter 4* and are primarily concerned with the use of ultrasound and how it enables the transformation of both

cyclopentasilane and trisilane into polymeric and/or nanoparticulate forms of hydrogenated silicon. In the case of cyclopentasilane, it is shown that this cyclic molecule can be sonochemically converted into high molecular mass polymers via ring-opening polymerisation without the action of ultraviolet light. Moreover, it is shown that the polymerisation process is not "macrothermal" in nature due to the temperature of the solution, but rather that it must stem from ultrasound-induced cavitational phenomena at the microscopic scale. In the case of trisilane, a method involving a combination of sonolytic and photolytic treatment is developed and shown to yield a solution-processable silicon polymer - silicon nanoparticle composite ink. Inks based on both of these monomers are subsequently used to fabricate amorphous silicon thin films via spin coating and atmospheric pressure CVD. The high purity of the composite ink prepared from trisilane and the slow film growth via atmospheric pressure CVD made possible the passivation of crystalline silicon (c-Si) surfaces. The films yielded good effective minority charge carrier lifetimes and surface recombination velocities of $\sim 400\,\mu s$ and $\sim 34\,cm\,s^{-1}$, respectively. With the aid of hydrogen radical treatment via hot-wire, the optoelectronic quality of the films was further improved and found to be comparable to that of similarly processed material found in the literature. This enabled the deposition of thick intrinsic absorbers (i-layers) for n-i-p type thin-film solar cells, with the best device exhibiting a promising efficiency of 3.4 %.

A separate section is allocated to the development and understanding of the curious and surprisingly simple "fusion" of silicon nanoparticles that ensues upon sonication of trisilane solutions. Here, the synthesis of discrete, unoxidised, hydrogenated, and amorphous silicon nanoparticles of tunable size in the range of 1.5–50 nm is demonstrated. In addition, it is shown that under certain conditions, sustained ultrasonic irradiation yields highly porous, sponge or coral-like silicon nanoparticle agglomerates with non-crystalline nanoscopic high specific surface area morphologies. These results are interesting because traditional methods rely on synthesis routes that yield c-Si nanoparticles and/or involve intricate electronics, expensive vacuum equipment or elaborate preparation procedures. The method developed herein employs a single liquid as both the silicon and hydrogen precursor and can be carried out in very compact spaces. In addition, the exterior surface of the particles is found to be hydrogen-terminated, which not only makes the particles directly suitable for subsequent surface functionalisation,

but in conjunction with the absence of a surface oxide, it avoids the need for oxide shell removal or surface hydrogenation via post-treatment with, for instance, hydrofluoric acid.

More in-depth discussions of these and other findings are provided in summaries at the end of each of the six main results sections comprising *Chapter 4*. The *Summary and Outlook* of *Chapter 5* include a final synopsis and discussion of the main experimental results of the thesis, the main conclusions that were drawn, as well as suggestions on the direction in which future work could head.

In summary, the work demonstrates a new solution-processing method that can be used to fabricate silicon hydride compounds of polymeric or nanoparticulate nature. The method exploits the sonochemical effects that ensue upon the collapse of microbubbles generated via ultrasound in solutions of cyclopentasilane or trisilane. The syntheses are low-temperature, vacuum-free, scalable, and the only essential piece of equipment is an ultrasonic horn. It is my hope that the employment of these hitherto unexplored experimental conditions using liquid silanes and ultrasound may open the door to a new and exciting sonochemistry of silicon.

Chapter 2

Fundamentals

This chapter provides a brief review of the main topics and characterisation methods dealt with in the thesis. The silicon hydrides are covered first, including selected chemical properties and synthesis techniques, and the methods that are most commonly used to transform them into higher silicon hydrides and silicon hydride polymers. The gas-phase and solution-processing deposition techniques used to prepare a-Si:H thin films are also discussed. This is followed by a brief discussion of the optoelectronic applications considered in the thesis. Next, the use of ultrasound and sonochemistry are discussed in the context of polymer and nanoparticle synthesis. Finally, the theoretical basics and working principles of the various analytic techniques employed in the characterisation of the samples are addressed.

2.1 Silicon Hydrides

The first report of a silicon hydride, or silane for short, stems back to Wöhler and Buff in 1857 [22]. The silane that they isolated was produced from the decomposition of silicon-contaminated aluminium in hydrochloric acid (HCl), but at the time they could not unambiguously identify its composition. About 10 years later, Friedel and Ladenburg would show that monosilane (SiH_4) was most probably the compound that was synthesised [23]. Some time later in 1902, Moissan and Smiles succeeded in synthesising disilane (Si_2H_6) [24]. Through the pioneering work of

Alfred Stock, the next two decades saw much progress in the synthesis and understanding of the chemical nature of the silanes. Between 1916–1926, with the aid of specially developed hermetic high vacuum apparatuses which enabled safer handling of the pyrophoric lower silanes, Stock and co-workers were able to synthesise and isolate additional silanes up to hexasilane (Si_6H_{14}) [25–27]. By now the silanes were known to occur as a homologous series with general formula Si_nH_{2n+2} ($n = 1, 2, 3, \dots$). While the first two members of the series, namely monosilane and disilane are gaseous, trisilane (TS, Si_3H_8) through to nonasilane (Si_9H_{20}) are liquid at stp. Higher silanes from decasilane ($Si_{11}H_{22}$) onward are solid.

From the late 1960's through to the late 1980's work by Fehér and co-workers extended the work of Stock in a number of ways. For one, larger and safer apparatuses were built that allowed for the semi-technical scale synthesis of crude silane mixtures of up to 50 litres from the decomposition of magnesium silicide (Mg_2Si) [28, 29]. Here, the "crude silane" is a blend composed of varying amounts of lower and higher silanes (i.e. silanes with $n > 5$). Their work yielded extensive understanding of silanes synthesis, pyrolytic and photolytic decomposition mechanisms, the detection and fractional distillation of higher silanes up to pentadecasilane ($Si_{15}H_{32}$), as well as invaluable analytical studies, employing methods such as gas chromatography, mass spectrometry, Raman, infrared, and nuclear magnetic resonance spectroscopy [30–32]. For instance, it was discovered that silanes from heptasilane (Si_7H_{16}) upwards are no longer spontaneously flammable in air and that while the silanes up to TS are innately linear, from tetrasilane (Si_4H_{10}) onward branched isomers are also possible. These include, for instance, iso-tetrasilane ($SiH(SiH_3)_3$) or neo-pentasilane (NPS, $Si(SiH_3)_4$). In 1973, Hengge and Bauer were able to demonstrate for the first time the synthesis of an unsubstituted (devoid of organic side-groups) cyclic silane of the form Si_nH_{2n} ($n > 2$), namely cyclopentasilane (CPS, Si_5H_{10}) via the hydrogenation of decachlorocyclopentasilane with lithium aluminium hydride [33]. Just over 30 years later, CPS would turn out to be the silicon precursor used by Shimoda et al. in their seminal work on solution-processed thin-film transistors that would usher in the field of printable silicon optoelectronics [12].

The silanes, including their synthesis, molecular properties, and decomposition and polymerisation reactions and products have now been extensively studied [34–

38]. Higher order silanes can be synthesised from lower ones (e.g. from monosilane or TS) via silene/silylene insertions and hydrogen-shift reactions [39]. Well-established techniques used to do this include silent electric discharge [40], photolysis [41], and pyrolysis [34, 42]. Two distinct synthesis routes for a larger ring molecule, cyclohexasilane (CHS, Si_6H_{12}) have also been discovered [43, 44].

The properties of polymeric silicon hydrides that are produced alongside linear and branched silanes during treatment with e.g. UV light or heat, have also been investigated. It is, for instance, known that polymer products with average stoichiometric composition -$(SiH_x)_n$-, with $1 < x < 2$ possess a bright lemon yellow colour, while those with -$(SiH_2)_n$- are light brown [45–47]. On the other hand, linear, branched, and cyclic silanes are transparent. General chemical properties of silicon hydrides such as synthesis and bonding, reactivity, and thermodynamic properties can be found in [32, 38, 45–49]. Tabulated values for density, refractive index, viscosity, and surface tension for silanes from TS to heptasilane can be found in [50]. First principles calculations on the different molecular conformations, intermolecular interaction, and ring-opening polymerisation (ROP) properties of CPS can be found in [51–53].

2.2 Solution-Processed Silicon Hydride Polymer Inks

In general, inks intended for the fabrication of thin films of silicon via solution-processing techniques such as inkjet printing or spin coating cannot be prepared by simply dissolving the pristine monomer molecules in a suitable solvent. Rather, what is required is that the starting molecule undergo some sort of polymerisation process that produces a low volatility, high molecular weight (M_w) product. There are several reasons for this. Firstly, a high M_w mitigates desorption of the silicon-containing component of the ink during deposition and pyrolytic conversion. The latter conversion step is required to transform the "wet" polymer into a solid thin film. The temperature threshold at which the thermal energy is sufficient for the scission of Si-Si and Si-H bonds lies between 250–270 °C and once exceeded, the polymer begins to cross-link into a three-dimensional amorphous matrix [54].

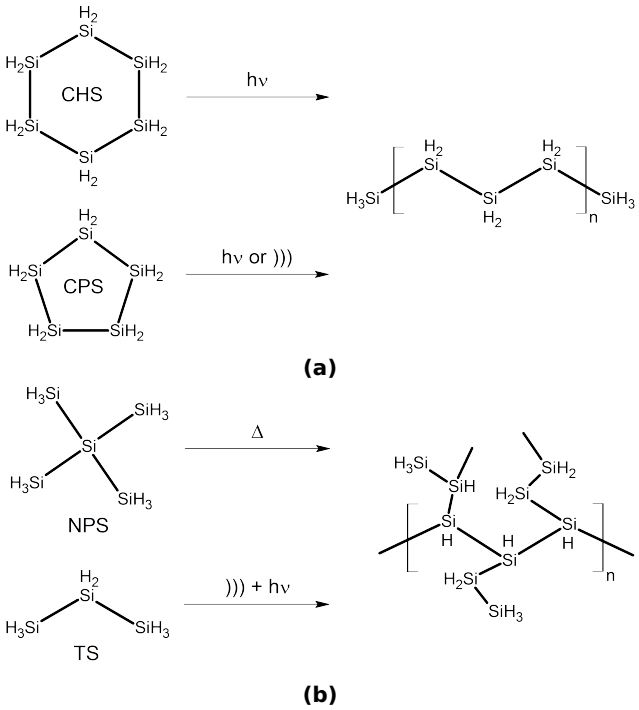

Figure 2.1: *Standard monomer molecules and polymerisation routes found in the literature as compared to our approach.* ***(a)*** *The cyclic molecules cyclohexasilane (CHS, Si_6H_{12}) and cyclopentasilane (CPS, Si_5H_{10}) and are usually photopolymerised ($h\nu$) using UV light and yield mainly polydihydrosilane products of the form -$(SiH_2)_n$-. In this work, ultrasound is shown to produce similar results (indicated by the))) symbol)* ***(b)*** *Alternatively, the branched molecule neopentasilane (NPS, Si_5H_{12}) is thermally polymerised (Δ) and gives branched polymer products of the form -$(SiH_x)_n$- with $x < 2$. As will be shown in the main text, branched polymers can also be prepared from the linear molecule trisilane (TS, Si_3H_8) using a combination of ultrasound and UV light.*

The temperature at which this transformation takes place is called the conversion temperature, T_{conv} and clearly needs to be lower than the average boiling point of the polymer chains themselves otherwise they evaporate without forming bonds to the substrate or neighbouring molecules upon thermal decomposition. For linear chains, this means that a spin coated ink containing Si_9H_{20} with an extrapolated boiling point at $\sim 280\,°C$ would, in principle, yield a solid a-Si:H film

upon annealing $\sim 270\,^{\circ}\mathrm{C}$. Lastly, in conjunction with the molecular structure of the polymer (e.g. branched or linear chains) and choice of solvent and substrate, its M_{w} also influences the wetting properties of the ink, which is critical for the preparation of homogeneous layers and fully covered surfaces [55, 56]. For further literature on liquid silicon inks the reader is referred to [57, 58].

2.2.1 Monomers and Polymerisation Techniques

In the following, several standard polymerisation techniques that are used to transform pristine monomer molecules into solution-processable polymers, as well some standard deposition techniques are briefly described.

There are several methods by which the monomer material is polymerised, the most common of which are illustrated in *Figure* 2.1. Particularly for the case of spin coated films and when highly volatile monomers are used, the increase in molecular mass brought about by the polymerisation of the monomer prior to or during deposition is necessary. It ensures good wetting and inhibits the desorption of the precursor upon coming into contact with the heated substrate or during subsequent pyrolytic conversion to a-Si:H.

In general, for applications where the ink is drop or spin coated, CPS and CHS are photopolymerised [12, 17, 59, 60] and NPS is thermally polymerised [14, 15]. There are, however, silanes that do not readily polymerise via photolyic means. As illustrated in *Figure* 2.2, many lower silanes are insensitive to UV irradiation as seen from their low extinction coefficients ϵ, and hence low absorbance for wavelengths of light λ, $< 250\,\mathrm{nm}$. For instance, the photolysis of TS dissolved in 2,3-dimethylbutane with 200 nm UV light from a mercury vapour lamp for 60 hrs leads to a mere $\approx 12\,\mathrm{rel}\%$ reduction in TS and results predomiantly in disilane and higher silanes up to heptasilane and little to -$(SiH_x)_n$- [41]. The ROP of CPS into high molecular weight, low volatility polymers by Shimoda et al. was carried out photolytically with 405 nm light and yielded a mixture of polysilanes of mass-average molecular mass $M_{\mathrm{w}} = 2600\,\mathrm{g\,mol^{-1}}$ which were found to be soluble in unreacted CPS or CPS/toluene solutions. It is interesting to note, however, that already as far back as 1974 Hengge and Bauer had reported that CPS is sensitive

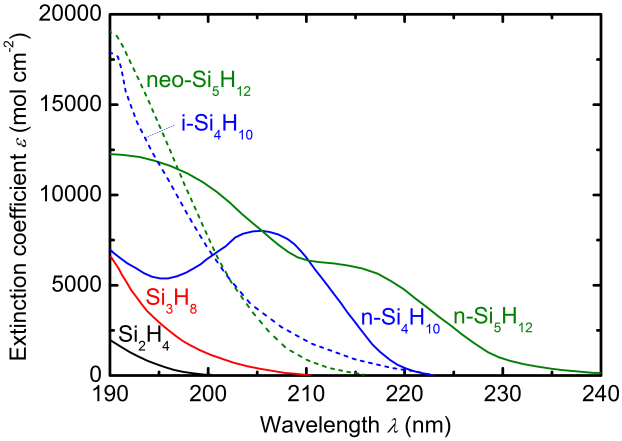

Figure 2.2: *Plot of extinction coefficient versus wavelength for several linear (solid lines) and branched (dashed lines) lower silanes. In general, the absorption edges lie below* 250 nm *rendering untreated silanes transparent in the visible range and hence also rather insensitive to conventional treatment with ultraviolet light in the range* 300–400 nm. *Note that the wavelength of the UV light source used in the thesis work was* 365 nm. *Data adapted from [32].*

to UV light and that it decomposes into monosilane and polymer products [61]. Inks prepared from CPS monomer can be doped p or n-type by adding dopant compounds of boron or phosphorous before or after UV irradiation, respectively. For instance, CPS can be mixed with white phosphorous (P_4) to produce an n-type copolymer ink upon UV irradiation (405 nm, 3500 mW cm^{-2}, 20–30 min) [62]. In a similar fashion, decaborane ($B_{10}H_{14}$) can be dissolved in CPS to prepare a p-type ink (80 °C, 365 nm, 15 mW cm^{-2}, 10–60 min) [54].

Alternative inks have also been developed using different monomer molecules, these include CHS [60] and NPS [14]. In the case of CHS, the ROP is likewise reported to be initiated photolytically, but instead of UV treatment of the CHS solution (in cyclooctane solvent) prior to deposition, the precursor is irradiated during actual spin coating. An alternative method involves the employment of pristine CHS solutions to grow thin films deposition via aerosol assisted atmospheric pressure CVD (AA-APCVD), although the film quality obtained thus far does not exceed

that of spin coated layers prepared with significantly less experimental effort [39]. In contrast, NPS is polymerised via a pyrolytical decomposition method entailing the thermal treatment of NPS in a teflon vessel at anything between 30–140 °C for 180–420 min. The method yields intrinsic and doped inks with M_w ranging from 550–2200 g mol^{-1}. The doping is achieved by adding BH_3-THF complex (borane-tetrahydrofuran, $C_4H_{11}BO$) to NPS prior to thermal treatment for p-type formulations of the ink and n-type inks are prepared by adding P_4 to already oligomerised NPS and then submitting the mixture to further heat treatment [14]. In general, unreacted monomer (CPS or NPS) is always present in excess and the polymerisation reactions are halted before the precursor is entirely consumed. This is because the monomers themselves are found to be very good solvents for their respective polymer products.

In this work (see *Chapter* 4) two monomer molecules are used, namely CPS and TS. Using CPS, the preparation of an ink via sonolytically initiated ring-opening polymerisation without the action of light [63] is demonstrated. With TS as precursor, a synthesis route for the fabrication of a silicon polymer - silicon nanoparticle (Si-NP) composite ink using a combination of sonication and subsequent irradiation with UV light is shown [64].

2.2.2 Solution-Processed Thin Film Deposition Methods

As alluded to previously, the employment of a liquid silane for depositing semiconducting thin films was first demonstrated in 2006 by Shimoda et al., where they successfully fabricated thin-film transistors by spin coating and inkjet printing a hydridosilane polymer ink made from CPS monomer [12]. In a major advancement for the field, 2012 saw the first demonstration of a fully spin coated a-Si:H single junction p-i-n photovoltaic device with an efficiency of 0.51 % [54]. This result was superseded by [14], where the fabrication of a similarly solution-processed n-i-p type solar cell was demonstrated exhibiting a significantly improved efficiency of 3.5 %.

For solution-processed silicon polymer films, the wetting properties of the ink and the stability of the films are of great importance, and have been studied previously [55, 56]. While earlier publications presented films deposited via spin coating,

more recent work has focused on developing alternative deposition methods, these include atmospheric pressure CVD (APCVD) using either a simple petri dish [65] or a more advanced gas phase reaction vessel [66], and aerosol assisted chemical vapour deposition (AACVD) [39]. Although not a classical liquid processing technique, the Shimoda group recently demonstrated the application of APCVD for the fabrication of a-Si:H of higher quality than previously possible using spin coating [65, 66]. The method entails vaporising pristine CPS monomer in a closed space containing a heated substrate (see *Figure* 3.1). The CPS molecules are thermally cracked at the substrate surface held at temperatures of around 275 °C and above, with best results at $\sim$ 360 °C.

For thermal CVD deposition techniques involving vaporised/aerosolised liquids or gas-phase transport of the silicon hydride material toward the substrate (AA-APCVD and APCVD), pre-polymerisation is not absolutely necessary since film growth presumably takes place via thermally activated reactions at the substrate [39, 66]. In the present work, the use of a Si polymer/Si-NP composite ink serves two main functions. Firstly, the ink contains higher order silanes and branched hydridosilanes (-$(SiH_x)_n$-), which compared to TS are much less volatile, have lower pyrolytic decomposition temperatures and have higher M_w, all of which mitigate evaporation/desorption losses during deposition and enhance the film growth rate. Secondly, since the ink also contains dense amorphous and hydrogenated Si-NPs, these are likewise transported toward to heated substrate and are hence also assimilated into the growing film. In particular for spin coated samples after pyrolytic conversion, the hydrogen is found not to reside at ideal bonding sites within the film. It is hence common (and necessary) practice to post-treat such films with hydrogen radicals generated via hot-wire [13, 14, 67–69] or in a plasma process [60].

Other techniques applied to the deposition of silicon hydride polymer inks include doctor blade coating for thin-film transistors [18, 70] and slot die coating for the fabrication of c-Si thin-film solar cells [15].

In this work, spin coating and APCVD using an inverted petri dish are implemented. CPS derived inks are spin coated and TS derived inks (intrinsic and p-type) are used for both spin coating and APCVD. In the latter case, instead

of using the pure and untreated monomer liquid as is conventionally the reported (e.g. when CPS is used) in the literature, an already sonophotolytically prepared TS derived silicon polymer - silicon nanoparticle composite ink is applied as the precursor. Also presented are selected properties of Si-NP thin films prepared by spin coating or drop-coating TS solutions subjecting solely to ultrasound.

2.3 Hydrogenated Amorphous Silicon

Since the material was first reported on in the late 1960's by Chittick and co-workers [71], the preparation and properties of hydrogenated amorphous silicon (a-Si:H) thin films have been extensively studied and there is a vast amount of literature on the subject, a comprehensive overview of which can be found in the book by Street [72]. Thin films of a-Si:H are conventionally deposited from the gas phase using chemical vapour deposition (CVD) techniques such as plasma enhanced CVD (PECVD) and hot-wire CVD (HWCVD).

In contrast to the ordered structure of crystalline silicon (c-Si), the morphology of a-Si:H is characterised by subtle deviations in the near and medium range atomic order (1^{st} to 3^{rd} nearest neighbours) due to variations in both bond length and angle, which in turn lead to the complete absence of long range order [73, 74]. The disorder of the a-Si:H matrix leads to unique optical and electrical properties. Bonding disorder (predominantly from deviations in bond angle) results in electronic transport characterised by low effective charge carrier mobility due to scattering in the bands and trap-release processes at localised states within shallow band edges (band tails). Structural disorder gives a-Si:H a high absorption coefficient, a quasi-direct optical band gap of $\sim 1.7\,\mathrm{eV}$ due to a relaxation of the momentum selection rules and coordination defects otherwise know as dangling (unsaturated) bonds. These defects give rise to a high density of energetically low ($\sim 0.9\,\mathrm{eV}$) electronic states within the band gap which renders unhydrogenated a-Si of little technological use in optoelectronic devices. The formation of such high defect densities is suppressed during growth via CVD due to the presence of chemically bonded hydrogen in the films at lattice sites that would otherwise constitute dangling bonds (introducing hydrogen during film deposition via sputtering has a similar effect).

Later in this work, methods such as Fourier transform infrared spectroscopy (FTIR), Raman scattering, and photothermal deflection spectroscopy (PDS) will be used to study the aforementioned absorption and structural properties of a-Si:H fabricated using solution-processing methods and how they compare to PECVD material.

Hydrogen is found to play a critical role in the production of high quality a-Si:H and has an influence not only on its optical and structural properties such as band gap and slope of the band tails, but also on its optoelectrical performance. The very low electrical conductivity in the dark ($\sim 10^{-10}\,\mathrm{S\,cm^{-1}}$) and very high photoconductivity under illumination ($\sim 10^{-5}\,\mathrm{S\,cm^{-1}}$) of state-of-the-art intrinsic a-Si:H are indicative of material with high charge carrier mobilities and/or charge carrier lifetimes (high $\mu\tau$ product). The presence of hydrogen and the nature of its bonding configuration in a-Si:H is routinely studied via infrared spectroscopy and in special cases (e.g. depth dependent bonding studies) also via Raman scattering [69, 75].

With these techniques high quality, compact material is found to almost exclusively exhibit Si-H stretching modes at $\sim 2000\,\mathrm{cm^{-1}}$ associated with a monohydride group at small monovacancy or divacancy sites (with a radius of $\sim 0.5\,\mathrm{nm}$) [72, 74]. Material of less compact morphology due to the presence of so-called microvoids ($\sim 0.1\,\mathrm{nm}$ or larger) is characterised by additional modes at higher wavenumbers between 2050–2090 $\mathrm{cm^{-1}}$ [76]. As will be discussed next, the relative ratio of these two bands provides a fast and effective measure of the material's morphology.

2.3.1 Microstructure Factor

The infrared microstructure factor, R, is defined as

$$R = \frac{I_{2080}}{I_{2000} + I_{2080}} \cdot 100\%, \tag{2.1}$$

where I_{2000} and I_{2080} are the deconvoluted intensities of the SiH and $\mathrm{SiH/SiH_2}$ stretching modes at 2000 and $2080\,\mathrm{cm^{-1}}$, respectively [77, 78]. The $2000\,\mathrm{cm^{-1}}$ mode corresponds to SiH bonds in dense bulk material, while the $2080\,\mathrm{cm^{-1}}$ modes

corresponds to SiH/SiH_2 bonds in less dense a-Si:H such as at the internal surfaces of microvoids [76, 79–81]. The lower the value of R, the more compact the morphology and hence the better the quality of the layer. Furthermore, after $H^{\bullet}$ treatment, a growth in the $2000\,cm^{-1}$ mode is desirable since this is associated with hydrogen that has gone on to passivate previously unsaturated Si dangling bonds in the bulk of the material. This results in a reduction in defect density and hence better excess charge carrier transport properties and thus to an improvement in optoelectronic behaviour.

2.3.2 Estimation of Hydrogen Content

The hydrogen content or atomic concentration c_H^* of the films is estimated using the Si-H stretching mode absorption band between 2000–$2080\,cm^{-1}$ as acquired via FTIR. The method requires an independent measurement of the thickness d of the film and the determination of the integrated infrared absorption I of the FTIR signal given by

$$I = \int_{2000}^{2080} \frac{\alpha(\omega)}{\omega} \mathrm{d}\omega, \tag{2.2}$$

where $\alpha(\omega)$ is the infrared absorption as a function of wavenumber ω [80, 82]. The spectral analysis involves the summation of the intensities of the deconvoluted components as

$$I = \sum_{i=2000}^{2080} I_i = \frac{\int \omega_i}{\omega_i \times d}, \tag{2.3}$$

where the index $i = 2000\,cm^{-1}$ or $2080\,cm^{-1}$, the integral in the numerator is the area of the i^{th} mode, ω_i is the position of the peak maximum of the i^{th} mode and d is the thickness of the film in cm. The c_H^* and I are related as

$$c_H^* = \frac{N_H}{N_H + N_{Si}} \cdot 100\%, \tag{2.4}$$

where $N_H = A \cdot I$, with $A = 1 \times 10^{20}\,cm^{-2}$ is an empirically determined proportionality constant and $N_{Si} = 5 \times 10^{22}\,cm^{-3}$ is the atomic density of amorphous silicon.

The above calculation tends to overestimate the value of c_H due to multiple internal reflections which effectively increase the optical path length in thin films. We hence employ the correction factor put forth by Langford et al. to compensate for this apparent increase in infrared absorption in the layers given by

$$c_{\mathrm{H}} = \frac{c^*_{\mathrm{H}}}{1.72 - K\omega d}, \tag{2.5}$$

where $K = 0.0011$, ω is the wavenumber in cm^{-1}, and d is the film thickness in µm. The correction factor is applicable for samples with $c_H < 30\,\mathrm{at\%}$ and for ωd products for which the denominator is > 1 [82, 83].

2.3.3 Optoelectronic Applications

Thin films of a-Si:H are used in two applications in this work, namely in n-i-p type solar cells and as intrinsic surface passivation layers for c-Si wafer substrates. The latter, while not a complete optoelectronic device, constitutes a preliminary step in the fabrication of industrially relevant heterojunction with intrinsic thin layer (HIT) solar cells.

As shown in *Figure* 2.3a, the n-i-p solar cell architecture consists of a thick intrinsic (i) a-Si:H sandwiched between two thin, doped layers (n and p-type). The i-layer is responsible for light absorption and the doped layers for setting up an electric field in the device that enables charge carrier (electron-hole pair) separation and subsequent transport to the respective electrodes [84]. The ZnO functions as the rear contact and the ITO (indium tin oxide) as the transparent and conductive front electrode. A Ag grid is subsequently deposited to complete the electrical contacting. The layer thicknesses of the n, i and p a-Si:H layers were typically of the order of 30 nm, 80–120 nm and 15 nm, respectively. It should be noted that the i-layer is usually somewhat thicker (100–300 nm) in state-of-the-art PECVD cells.

The HIT solar cell shown in *Figure* 2.3b is governed by a different working principle and has a different layer stack. As opposed to n-i-p type solar cells which are drift devices, where a built-in electric field drives the electrons and

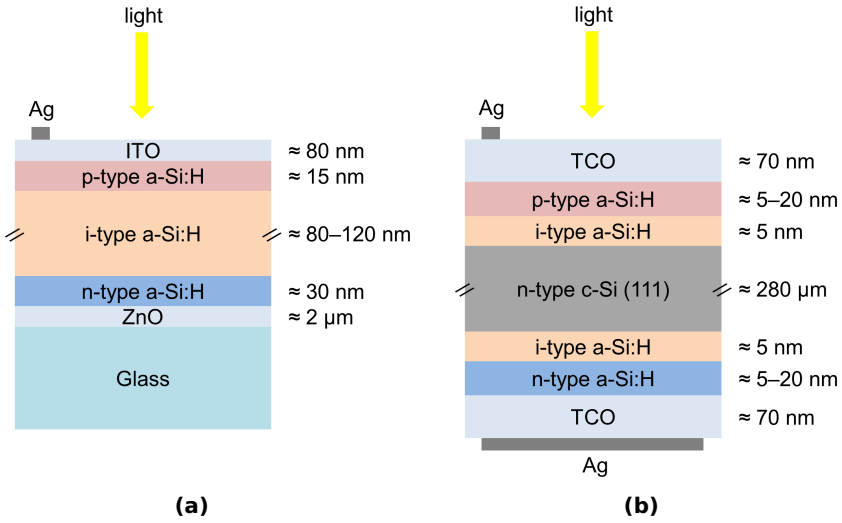

Figure 2.3: *(a) Schematic diagram of the n-i-p layer stack implemented in the thin film solar cells fabricated in this work. Note that the thick intrinsic (i-) layer (≈ 80–120 nm) in this device functions as the absorber material.* ***(b)*** *Schematic of a typical heterojunction with intrinsic thin layer (HIT) solar cell. Here, the thin i-layers (≈ 5 nm) are responsible for the passivation of dangling bond defects on the surface of the c-Si wafer. All layer thicknesses given are approximate.*

holes to their respective electrodes, HIT cells are diffusion-based devices. These cells rely on the extremely high effective charge carrier diffusion lengths in c-Si for ensuring that charge carriers are collected at the terminals. The intrinsic a-Si:H layers are responsible for passivating dangling bond defects on the surface of the c-Si wafer thereby enabling very low effective surface recombination velocities $S_{\text{eff}} < 10\,\text{cm}\,\text{s}^{-1}$. The doped p- and n-layers act as front and back surface passivation fields, respectively. The Ag and TCO (transparent and conductive oxide) in the front have the same function as in the n-i-p cell and the rear TCO/Ag ensures good electrical contact to the n-layer.

2.4 Ultrasound and Sonochemistry

The employment of ultrasound (US) for the synthesis of polymeric and nanoparticulate materials offers an alternative energy source to those used in conven-

tional chemistry, where usually either heat, electromagnetic waves (e.g. light, microwaves), or electricity are used. The actual chemical activation mechanism at work during sonication, however, does not result from the direct interaction of ultrasonic waves with matter via coupling to electronic, vibrational or rotational molecular states, but rather from a secondary phenomenon known as acoustic cavitation. This can be demonstrated as follows: if we assume a speed of sound c in a trisilane/cyclooctane solution in the range of 1000–1300 $\mathrm{m\,s^{-1}}$ and take a tip oscillating frequency f of 26 kHz, it can be readily calculated that the relation $\lambda = c/f$, gives a wavelength λ of 3.8–5 cm for the generated ultrasonic waves. These length scales are far in excess of molecular dimensions and hence any direct coupling to molecular modes is ruled out. When liquids are irradiated with US in the frequency range 20 kHz to 500 MHz, the high tensile stress during rarefaction cycles can cause local rupturing of the liquid at weak spots [85]. These weak spots may include dust particles, solid impurities or pre-existing pockets of gas (e.g. air/nitrogen) in the fluid. The formed cavities grow into microbubbles during one or several cycles until reaching a maximum size of $\sim$ 100–150 µm before experiencing implosive collapse. It is this series of events encompassing the inception, expansion and implosion of microbubbles that is termed acoustic cavitation and the field concerned with its application to the synthesis and modification of materials is known as sonochemistry [85, 86].

Sonochemistry stems back to 1927 where Wood and Loomis reported for the first time on the physical and biological effects of high intensity ultrasound [87]. Sonochemistry has now been extensively studied [85, 88–91] and its chemical applications include for instance, increasing chemical reaction rates (sonocatalysis) via the generation of radicals, polymer synthesis [92], polymer degradation [93], and metallic compounds synthesis. Some physical effects include enhanced mass and heat transport via stirring due to high-velocity microjet formation, collision-induced sintering of particles [94], surface cleaning and morphological alteration via asymmetric bubble collapse at the solid-liquid interface, and degassing of liquids.

At present, the sonochemical effect is understood to be triggered by the formation of a so-called thermal "hot spot" during cavitational collapse. Temperatures and pressures at these hot spots have been reported to reach values as high as

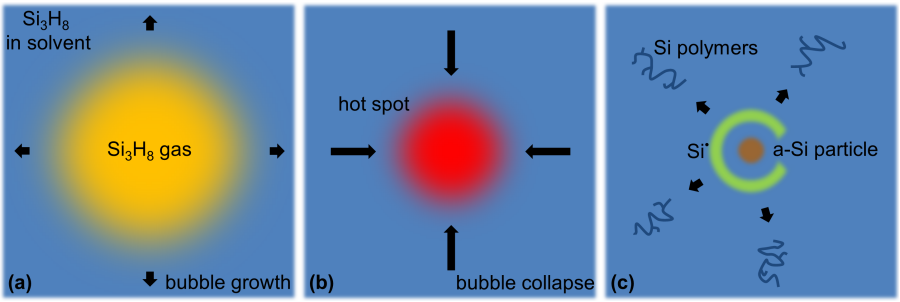

Figure 2.4: *Schematic depiction of the growth and collapse of a bubble, and the ensuing synthesis of solid-state silicon via the sonochemical effect.* ***(a)*** *During decompression cycles, an expanding bubble is preferentially filled with highly volatile trisilane (Si_3H_8) dissolved in the solvent (e.g. cyclooctane).* ***(b)*** *Upon bubble collapse, high transient temperatures and pressures result in the creation of a "hot spot".* ***(c)*** *The implosion results in the generation of new silicon-containing species, namely an amorphous silicon (a-Si) particle and Si radicals ($Si^{\bullet}$), the latter of which subsequently diffuse into the bulk of the liquid to form Si polymers.*

5000 K and 1000 atm, respectively [95]. The transient nature of the hot spots of $\sim 10^{-9}$–10^{-12} s gives rise to short energy pulses of $\sim$ 0.1–10 eV and cooling rates of $\sim 10^{9}\,\mathrm{K\,s^{-1}}$. A schematic representation of the acoustic cavitation phenomenon as applied to the trisilane/cyclooctane system is given in *Figure* 2.4. In general, there are several factors influencing sonochemical action, these include the characteristics of the liquids used such as solvent and solute vapour pressure, viscosity, purity (e.g. dissolved solids), and surface tension, as well as sonication parameters such as frequency and amplitude.

2.5 Silicon Nanoparticle Synthesis

The ink developed in this work using trisilane as precursor is in fact a Si nanoparticle - Si polymer composite ink and is to the best of our knowledge, the first reported silicon hydride nanocomposite ink of its kind. In general, Si-NPs can be fabricated via a plethora of vacuum and solution-processing methods. Typical vacuum-based fabrication techniques involve the use of radio frequency or

microwave plasma reactors [96–98], hot-wall reactors [99, 100], hot-wire [101], reactive sputtering [102] or laser ablation [103]. Solution-processing methods include synthesis routes based on the reaction of silicon compounds such as $SiCl_4$, Mg_2Si or NaSi, with selected salts [104–106]. There are also hybrid techniques, e.g. where ultrasound is used to promote the reduction of tetraethyl orthosilicate by metallic sodium in toluene solutions held at −70 °C [107] or where a porous silicon film is prepared by electrochemically etching the surface of a c-Si wafer with subsequent sonication of the surface resulting in the breaking off of individual Si-NPs [108]. Unfortunately, most of these synthesis routes yield crystalline Si-NPs, involve intricate electronics, expensive vacuum equipment or elaborate preparation procedures. The synthesis route that will be demonstrated in this work employs a single liquid (TS) as both the silicon and hydrogen precursor and since the entire preparation is carried out in a N_2-filled glove box, it is vacuum-free, low-temperature and can be executed in very compact spaces, e.g. in a 2 mL glass vial. As will be shown in *Chapter* 4, sonication presents a reliable method for "fusing" amorphous Si-NPs, a feature that differentiates it from most other preparation methods. In addition, the exterior surface of the particles is hydrogen-terminated, which not only makes them suitable for subsequent surface functionalisation, but in conjunction with the absence of a surface oxide makes the need for post-treatment with, e.g. hydrofluoric acid for oxide shell removal or surface hydrogenation, redundant [11, 109, 110].

In addition to its application to processes such as sonocatalysis and polymer synthesis (*Section* 2.4 above), sonochemistry has also been applied to the fabrication of a myriad of metallic and organic nanostructured materials, for instance metals (e.g. amorphous iron), metal oxides (e.g. TiO_2), chalcogenides (e.g. CdSe), and carbon nanotubes, to name but a few [111, 112]. As of this writing, however, there is no evidence for the employment of sonication or sonochemical means for either the direct synthesis of silicon hydride polymers nor of Si-NPs from a heterogeneous liquid-liquid system comprising a lower silane and an organic solvent.

2.6 Characterisation Techniques

Numerous techniques are used throughout this work to characterise the Si polymer - Si nanoparticle composite ink prepared from TS, and separately the Si-NPs, as well as the Si polymer prepared from CPS. In the following subsections the various characterisation methods are introduced and the reasoning behind their employment is also briefly explained. For further details refer to *Chapter* 3.

2.6.1 Characterisation of the Silicon Polymer - Silicon Nanoparticle Composite Ink

The properties of the inks fabricated from the two monomers used in this work, namely CPS and TS, were selectively characterised via UV-Vis transmission measurements, size exclusion chromatography (SEC), gas chromatography - mass spectrometry (GC-MS) and nuclear magnetic resonance (NMR).

UV-vis is used to study and spectroscopically quantify visual changes observable with the naked eye in treated solutions. Since both CPS and TS monomers are transparent in the visible range, these measurements allow us to associate optical absorption variations with chemical reactions in the processed inks.

Analysis via SEC is carried out for two main purposes. Firstly, it was employed to chromatographically confirm that the sonication of CPS solutions yields polymer products and if so, to monitor the distribution and evolution of the molecular weight as a function of time. Secondly, to ascertain whether the ring-opening polymerisation is "macrothermally" initiated as a result of the slightly increased temperature of the solution due to unintentional heating during sonication or, instead, if it can be ascribed to sonochemical effects. SEC allows for the analysis of treated and untreated solutions containing a mixture of untreated monomer and polymer products by temporally separating the species as they are pumped through a densely packed column. The varying degree of diffusion of the polysilanes (the analytes) into, out off and around the pores of the stationary phase (i.e. the packing material) results in different retention times according to their size and/or

structure. In this way, smaller molecules can infiltrate deeper and into more of the micropores and hence take longer to elute from the column, on the other hand larger molecules are partially or fully excluded from entering the porous microstructure and hence have a shorter retention time in the column [63, 113, 114].

GC-MS is used to detect and identify more volatile species that can be transported in the gas phase. The technique involves injecting a solution containing the analytes into a capillary column housed in an oven. As the temperature is raised, the specific chemical properties and varying degree of interaction of the dissolved molecules with the internal walls of the column lead to their temporal separation as they exit the column into an attached mass spectrometer. The mass spectrometer then ionizes the individual molecules which results in their fragmentation and subsequent identification according to their mass-to-charge ratio and fragmentation pattern. The characteristic retention times and mass spectra of the detected components allow for reliable identification of the molecules' chemical composition and molecular mass [115–117].

The compounds studied in this work are known to be composed predominantly of hydrogen and silicon, however, the bonding configuration of these elements in the polymer is not straight-forward to determine. For the case of the TS-based ink, liquid-state ^{29}Si NMR spectroscopy was used to address the specific question as to whether the derived polymer had a linear or branched molecular structure. NMR relies on the fact that atomic nuclei in a magnetic field interact differently with electromagnetic radiation (i.e. exhibit different absorption and emission behaviour) depending on their magnetic properties and neighbouring molecular environment [118, 119]. Slight variation in the resonance frequency at which this absorption and re-emission takes place enables the determination of the position and relative abundance of atoms in a molecule, for instance, whether the Si atom is present in at a branching point -SiH, along the length of the chain -SiH_2- or at the end of a chain as a -SiH_3 end group [64, 113]. Of particular interest is the relative abundance of these groups, since it has been reported that for spin coated films more SiH_3 end groups are conducive to enhancing the quality of the cross-linking and densification of the Si polymer into a-Si:H upon pyrolytic conversion [14].

2.6.2 Characterisation of Thin Films and Optoelectronic Devices

2.6.2.1 Amorphous Silicon Thin Film and Nanoparticle Morphology and Microstructure

The electron microscopy techniques used to study a-Si:H thin films and Si-NPs include scanning electron microscopy (SEM), transmission electron microscopy (TEM), and scanning TEM (STEM). SEM allows for the fast evaluation of film and Si-NPs morphology with images revealing details from the micron to $\sim 10\,\mathrm{nm}$ range. On the other hand, TEM and STEM allow for introspection with a resolution down to the atomic scale. The spectroscopic techniques used include highly spatially resolved electron energy loss spectroscopy (EELS) on the nano-scale, and Fourier transform infrared spectroscopy (FTIR) and Raman spectroscopy on the macro-scale. FTIR provides invaluable information on the Si-H, Si-O, and C-H bonding in the samples by studying the properties (intensity and location) of infrared active molecular absorption bands. This is used to characterise the microstructure by differentiating between dense bulk material and surface-rich microvoid regions, to study the process of oxidation upon exposure to air, as well as to estimate hydrogen content. Raman spectroscopy enables an investigation of the amorphous nature of the samples via an analysis of characteristic Si-Si phonon modes. The location, relative intensity and spectral width of these modes allows for an analysis of the near and mid range order of the silicon bonding in the a-Si:H matrix [120–123].

In terms of optoelectrical performance, a-Si:H layers are characterised via lateral electrical conductivity measurements using two co-planar metallic (Ag) electrodes. The photoresponse (σ_{PR}), defined as the ratio of the conductivity of the film under illumination (σ_{ph}) to its conductivity in the dark (σ_{d}), provides a simple measure of the layer's semiconducting quality. Undoped or intrinsic (i) layers should generate maximal photocurrent upon illumination so that (σ_{ph}) should be as high as possible. In state-of-the-art solar grade PECVD films, σ_{ph} reaches values of the order of $\sim 10^{-5}\,\mathrm{S\,cm^{-1}}$ under illumination at approximately one sun (AM1.5, $100\,\mathrm{mW\,cm^{-2}}$). In contrast, in the dark the i-layer should have as low a majority

charge carrier density as possible and hence exhibit a σ_{d} as small as possible. Low values of σ_{d} are an indication of low defect density and/or a Fermi level lying deep within the band gap. Typically, σ_{d} has a value in the range 10^{-11}–$10^{-10}\,\mathrm{S\,cm^{-1}}$ in good quality material [124]. In general, material with $\sigma_{PR} > 10^3$ is deemed suitable for optoelectronic device application. Films doped p or n-type for use in devices where conductance through the thickness of the layer is intended (i.e. transverse instead of lateral conductance) such as in solar cells, typically have conductivities ($\sigma_{\mathrm{d}} \approx \sigma_{\mathrm{ph}}$) in the range $\sim 10^{-2}$ and $\sim 10^{-4}\,\mathrm{S\,cm^{-1}}$, respectively [72].

2.6.2.2 Photovoltaic Cells

The performance of the solar cells is evaluated via current density versus voltage (JV) curves using solar simulator. Here, the open circuit voltage V_{oc} and the short circuit current I_{sc} are the measured voltage at zero current and current at zero voltage, respectively. The fill factor FF is defined as

$$FF = \frac{P_{\mathrm{max}}}{V_{\mathrm{oc}} I_{\mathrm{sc}}}, \tag{2.6}$$

where P_{max} is the power density at the maximum power point of the cell. The efficiency η of the cell is then simply the ratio of maximum electrical output P_{max} to optical input power density P_{opt} [125]. In combination with the previous expression this gives

$$\eta = \frac{P_{\mathrm{max}}}{P_{\mathrm{opt}}} = FF \frac{V_{\mathrm{oc}} I_{\mathrm{sc}}}{P_{\mathrm{opt}}}. \tag{2.7}$$

The series resistance R_{s} and shunt resistance R_{sh} are calculated from the JV curve from the inverse slope at V_{oc} and I_{sc} as

$$R_{\mathrm{s}} = \left.\frac{\Delta V}{\Delta I}\right|_{V=V_{\mathrm{oc}}} \tag{2.8}$$

and

$$R_{\mathrm{sh}} = \left.\frac{\Delta V}{\Delta I}\right|_{I=I_{\mathrm{sc}}}, \tag{2.9}$$

respectively.

2.6.3 Surface Passivation Layers

The quality of the surface passivation of c-Si wafer substrates is assessed via effective minority charge carrier lifetime measurements.

The effective lifetime τ_{eff} of the minority charge carriers (i.e. holes in n-type c-Si) is estimated from a fit to the exponential decay as a function of time of excess holes $\Delta p(t)$ generated in the bulk of the sample by a short optical excitation pulse, and is given by

$$\tau_{\text{eff}} = \frac{\Delta p(t)}{G - \frac{\mathrm{d}}{\mathrm{dt}}\Delta p(t)}, \tag{2.10}$$

where G is the generation rate. The measured τ_{eff} is a superposition of the bulk τ_{b} and surface τ_{s} lifetimes as

$$\frac{1}{\tau_{\text{eff}}} = \frac{1}{\tau_{\text{b}}} + \frac{1}{\tau_{\text{s}}} \approx \frac{1}{\tau_{\text{s}}}, \tag{2.11}$$

where the approximation stems from the fact that $\tau_{\text{b}} >> \tau_{\text{s}}$ in high purity/high quality float-zone c-Si [126].

We hence have that $\tau_{\text{eff}} \approx \tau_{\text{s}}$, which in combination with the assumption of a large value for the diffusion coefficient D and symmetric interfaces yields an approximate expression for the effective surface recombination velocity S_{eff} as

$$S_{\text{eff}} = \frac{d}{2}\left[\tau_{\text{eff}} - \frac{1}{D}\left(\frac{d}{\pi}\right)^2\right]^{-1} \approx \frac{d}{2}\tau_{\text{eff}}, \tag{2.12}$$

where d is the wafer thickness [127].

Chapter 3

Experimental

This chapter is concerned with a summary of the raw materials, equipment, and the various experimental and analytic techniques that were employed in the development and characterisation of the inks, the silicon nanoparticles, and the thin films thereof.

3.1 Materials

The preparation of the CPS and TS-based inks, as well as the Si-NPs was carried out under dilution in an organic solvent. The solvent of choice was dried cyclooctane (CO, C_8H_{16}) from Sigma Aldrich (99.0 % purity). The CO was additionally dried with sodium and degassed via evacuate-refill cycles in a N_2-filled Schlenk line. The cyclopentasilane (CPS, Si_5H_{10}) was acquired from the group of Prof. Terfort at the University of Frankfurt and synthesised by Dr. Britta Kämpken via the hydrogenation of decachlorocyclopentasilane with lithium aluminium hydride [128]. The trisilane (TS, Si_3H_8) was purchased from Voltaix LLC (Silcore®, 99.99 % purity). For the p-type formulation of the ink technical grade decaborane ($B_{10}H_{14}$) from Sigma Aldrich was used. Some of the more relevant material properties of the solvent and the liquid silicon precursors are summarised in *Table* 3.1.

Table 3.1: *Summary of several material properties of the liquid substances used in the preparation of the ink [48, 57, 61, 129–131].*

Property	Cyclooctane	Cyclopentasilane	Trisilane
Formula	C_8H_{16}	Si_5H_{10}	Si_3H_8
Molar mass ($g\,mol^{-1}$)	112.21	150.51	92.32
Density ($g\,cm^{-3}$)	0.834	0.963	0.743
Colour	colourless	colourless	colourless
Boiling point (°C)	151	194	53
Melting point (°C)	10–13	−10.5	−117
Vapour pressure (Torr)	4.12	1.12	95.3
Refractive index	1.459	1.691	1.498
Dynamic viscosity ($m\,Pa\,s$)	0.254	0.546	0.318
Surface tension ($mN\,m^{-1}$)	31.46	32.5	18.7
Band gap (eV)	6.7	6.5	6.2
Purity (%)	> 99.0	> 95.0	> 99.99

The substrate materials used for standard layers were Eagle XG glass from *Corning* and double-side polished c-Si substrates of $15 \times 15\,mm^2$ in size. For the solar cells, $20 \times 20\,mm^2$ untextured Al-doped ZnO (AZO) coated glass was used. For the passivation layers, ca. $50 \times 50\,mm^2$ complete *RCA* treated float-zone n-type Si(111) substrates with specific resistivity $\rho \approx 3\,\Omega\,cm$ were used. The substrates submitted to piranha etch to remove residual organic impurities and a subsequent 1 % HF dip to remove the native oxide, thereafter introduced into inert N_2 atmosphere within 20 min.

3.2 Ink Preparation

Due to the pyrophoricity of CPS and TS, the entire handling and processing of the liquid silanes, treated and untreated solutions thereof as well as subsequent thin film deposition was carried out in a N_2-filled glove box from *MBraun* with residual traces of H_2O and O_2 of < 1 ppm. The liquids were transferred from their respective storage vessels using *Eppendorf* pipettes and disposable hypodermic needles and syringes. Filtering of processed solutions was done with 0.1 and 0.45 µm PTFE

syringe filters. Solutions were mixed and treated in 2 cm^2 borosilicate glass vials. Typical solutions have a volume of 1–1.6 mL and concentrations of 8–15 wt% and 35–55 wt% for CPS and TS monomer, respectively.

In order to mitigate evaporation losses during sonication, especially when using highly volatile TS as precursor material, solutions are actively cooled to temperatures between −10 and 20 °C using a Peltier cooling system. The cooler consists of a $40 \times 40 \times 40$ mm^3 copper block with a cylindrical borehole for the glass vial and two 72 W Peltier elements mounted on two of its lateral faces. The heat generated by each Peltier element is extracted and dissipated via two aluminium heat sinks attached to cooling fans. The remaining sides of the copper block are covered with polystyrene for increased thermal insulation. The cooling performance of the Peltier elements, and hence the temperature of the solution, is controlled by varying the power supply to the cooler. The system is mounted near the base of a retort stand to allow for the submersion of the ultrasonic horn into the solution from above. The temperature of the solution during sonication is measured using a type K thermocouple from *Thermocoax* immersed in the liquid itself.

The ultrasonic treatment of the solutions is carried out using a 26 kHz *Hielscher Ultrasonics* UP200St ultrasonic horn made of titanium and with a 2 mm diameter tip. The maximum amplitude at the tip is 240 µm and the duty cycle per second can be varied from 0 to 100 % in steps of 10 % and is typically set to between 40–60 % to avoid excessive unintentional heating of the solution. In the case of solutions where sonication was carried out without the aid of active cooling, lower duty cycles of 30–40 % are preferred in order to avoid heating the solution above $\sim$ 70 °C during treatment.

For the photolytic treatment of solutions with ultraviolet irradiation is carried out using a high power LED array from *Roithner Lasertechnik GmbH* is used. The array consists of 60 AlGaN diode chips with a peak wavelength at 365 nm and a total optical output power density of 100 mW cm^{-2}.

3.3 Thin Film Deposition

The thin films of silicon hydride polymer were cast on the substrates via two methods, namely spin coating and atmospheric pressure chemical vapour deposition (APCVD). State-of-the-art reference and doped a-Si:H layers were deposited via plasma enhanced chemical vapour deposition (PECVD). For the evaluation of film thickness, layers deposited on glass substrates are used to make small etch craters of 1–3 mm in diameter using KOH. Profilometry measurements are then made across the sharp edges where material was removed.

3.3.1 Spin Coating

Spin coated films are cast using a Spin150i coater from *SPS-Europe B.V.* The spin parameters were in the range 1500–200 rpm for 15–30 s. Subsequent cross-linking of the polymer to transform it to amorphous silicon was done by pyrolytic conversion on a hot plate at temperatures between 400–450 °C for 1–3 min. Layer thicknesses vary from around 50–80 nm for a single spin and up to $\sim$ 200 nm for substrates coated multiple times.

3.3.2 Atmospheric Pressure Chemical Vapour Deposition of Thin-Films

Films fabricated via APCVD were deposited as illustrated in *Figure* 3.1 using a variation of the technique originally demonstrated by Masuda at al. using an inverted petri dish [65, 132]. Firstly, the substrates are placed on the hot plate and pre-heated to temperatures in the range 350–450 °C. Then the inside of a petri dish is coated with 30–50 µL of liquid silicon ink and placed facing down over the heated substrates. This differs from the Masuda method in that instead of pure and untreated CPS monomer, the ready-to-use ink is employed which consists of CO solvent, higher order branched and linear silanes of the generic form Si_nH_{2n+2} with $n > 3$, silicon hydride polymer (-$(SiH_x)_n$-), amorphous Si-NPs and residual

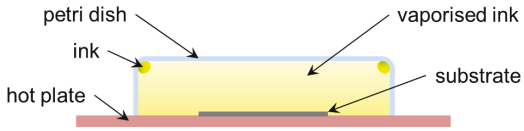

Figure 3.1: *Schematic depiction of the APCVD deposition setup. A substrate is placed and pre-heated on the hot plate. Thereafter a petri dish is coated on the inside with some ready-to-use ink and placed faced down over the substrate. As the dish and ink are slowly heated up by the hot plate an atmosphere of vaporised ink is produced within the confined space. After* 2–3 min *a thin film of a-Si:H is discernible on the substrate.*

unreacted TS. Shortly after coming into contact with the hot plate, the petri dish is indirectly heated and its base reaches 150–200 °C. This causes the ink to evaporate and produce an atmosphere of vaporised silicon ink (including the colloidal silicon species) within the confines of the space enclosed by the dish. After 2–3 min a thin film of a-Si:H is discernible on the substrate. The standard petri dish has a height of 20 mm and a diameter of 60 mm. This procedure is repeated several times until the desired film thickness is reached.

In a standard APCVD deposition, a petri dish is coated with 40 µL of a 40 wt% formulation of the TS ink and takes 4 min. With the substrate heated to $\sim$ 375 °C films of ca. 25 nm in thickness typically result. This gives a growth rate under standard conditions of $\sim$ 6 nm min^{-1} ($\sim$ 0.1 nm s^{-1}). Using more ink and higher substrate temperatures results in thicker films, albeit at the expense of material quality where rapidly grown films exhibit blistering and matt surfaces. The desired film thickness was hence achieved under relatively slow growth rate conditions using several coated petri dishes placed one after the other over the substrate. Finally, note that the temperature of the petri dish, and hence the rate of evaporation of the ink, is indirectly set by the temperature of the underlying hot plate and is thus not independently regulated under the current conditions.

The experimental setup used to deposit the passivation layers was identical to that shown in *Figure* 3.1 except that the substrate was isolated from the hot plate using two small c-Si supports in order to avoid contamination of or damage to the surfaces. The deposition was done at $\sim$ 350 °C using 75 µL of a 40 wt% formulation of the TS ink in two steps, 10 min per side. The film thickness of each layer is estimated at 10–20 nm. The passivation layer were not submitted to any additional hot-wire hydrogen treatment prior to characterisation.

Table 3.2: *Summary of the standard deposition parameters for the intrinsic (i) and doped (p and n) PECVD layers used in this work.*

Parameter	i-layer	p-layer	n-layer
Feedstock gas/gasses	SiH_4/H_2	$SiH_4/PH_3/C_3H_9B/CH_4$	SiH_4/PH_3
Flow (sccm)	23/45	10/121/18/10	24/10
Power density ($mW\,cm^{-2}$)	40	40	40
HF frequency (MHz)	13.56	13.56	13.56
Pressure (Torr)	1	1.5	0.8
Substrate heater temperature (°C)	250	250	285
Deposition time (s)	600	120	240
Deposition rate ($nm\,s^{-1}$)	0.17	0.14	0.13

3.3.3 Plasma Enhanced Chemical Vapour Deposition of Thin-Films

The intrinsic (i) and the p and n-type doped layers used as reference or in the optoelectronic devices were deposited using a high-vacuum PECVD cluster system. The deposition parameters for the layers are summarised in *Table* 3.2.

3.4 Hot-Wire Atomic Hydrogen Treatment

Hydrogen radical ($H^{\bullet}$) treatment after deposition to passivate the solution-processed films was carried out in a hot-wire CVD (HWCVD) high-vacuum chamber [133, 134]. The samples are transferred from the glove box to the hot-wire chamber in a specially designed hermetic transfer vessel, the samples are thus not subjected to an air break. The hot-wire system is equipped with tantalum filaments (wires) operated at 1300–1375 °C, these being responsible for dissociating H_2 into atomic H. The pressure in the chamber is 0.05 mbar with a H_2 flow of 50 sccm. The wires are fixed at a distance of 70 mm to the substrates and the substrate heater temperature T_{heater} is set to 400–450 °C. The substrates are preheated for 60 min in vacuum prior to passivation so that they reach the desired temperature and to allow for the desorption of any residual volatile species or moisture. Finally, treatment time varies between 30–120 min. For further details on this technique and the effects of $H^{\bullet}$ exposure on a-Si:H thin films see the following literature [67–69].

3.5 Optical Characterisation Techniques

3.5.1 UV-Vis Optical Transmission Measurements

The optical transmission measurements were carried out on solutions in hermetically sealed quartz tubes using two experimental setups, one for the measurement of CPS solutions and another for TS solutions. The former measurements were carried out using a Lambda 950 spectrophotometer from *PerkinElmer* equipped with an integrating sphere in the UV-Vis range from 220–740 nm and the latter using a home-built system consisting of a xenon high pressure lamp and a *Spex* 25 cm double monochromator.

3.5.2 Optical Microscopy

The optical microscope used was a *Nikon* Eclipse L200 equipped with a *Zeiss* AxioCam Mrc 5 camera and *Nikon* LU Plan objective lenses.

3.5.3 Electron Microscopy

3.5.3.1 Scanning Electron Microscopy

The scanning electron microscopy (SEM) images presented in this work are secondary electron contrast images and were acquired using a *Zeiss* LEO 1550 VP microscope under high-vacuum conditions using an electron accelerating voltage (EHT) of 20 keV.

3.5.3.2 Transmission Electron Microscopy

The transmission electron microscopy (TEM) images, the electron diffraction patterns and the electron energy loss spectroscopy (EELS) measurements were done on a *Tecnai* F20 transmission electron microscope equipped with a *Gatan* Tridiem 863P post column image filter. The samples were prepared using a carbon grid which was submerged into the solution and subsequently mounted into the TEM holder in the glove box to ensure a minimum exposure to air of about 5 min during transfer into the microscope

3.5.3.3 Scanning Transmission Electron Microscopy

The high-angle annular dark field scanning transmission electron microscopy (STEM) images were recorded using a sub-angstrom beam obtained in an aberration-corrected *Titan* 80-300 scanning transmission electron microscope. Particle counting was carried out with *ImageJ*.

3.5.3.4 X-Ray Photoelectron Spectroscopy

The x-ray photoelectron spectroscopy (XPS) measurements are carried out on a *Scienta Omicron* MXPS system with an XM1000 Al-K_α x-ray source at 300 W. The spectra are collected at a base pressure of $\sim 7 \times 10^{-11}$ mbar in constant analyser energy mode with a pass energy (PE) of 100 eV and a 1 eV step size for the survey spectrum and a PE of 20 eV for the high-resolution narrow scan spectra with a 0.1 eV step size.

3.6 Fourier Transform Infrared Spectroscopy

Fourier transform infrared spectroscopy (FTIR) measurements were carried out in order to investigate the morphology and hydrogen content of a-Si:H thin films prior to and after $H^\bullet$ treatment, and to study the microstructure, Si-H bonding configuration and oxidation behaviour of the a-Si-NPs. In the case of entirely inert measurements without N_2 atmosphere break, a special hermetic vessel with a set of germanium windows was used to characterise the samples using a *Bruker* Vertex 80v spectrometer. For samples that incurred an air break during transfer, characterisation was carried out under N_2 purging using a *ThermoFischer Scientific* Nicolet 5700 spectrometer. All measurements were conducted in transmission mode on double-side polished c-Si wafer substrates. For a brief overview of the most relevant infrared active modes discussed in this work refer to *Table* 4.1. More extensive identification and analysis can be found in [75, 135].

3.7 Raman Spectroscopy

The Raman spectroscopy measurements are carried out using a *Sapphire* 532 nm cw laser from *Coherent* and a *Shamrock* 303i spectrometer equipped with an iDus 420 Si CCD camera from *Andor*. The spot had a diameter of 1 µm and an intensity of 0.71 mW. The spectral resolution was $\sim 1\,\mathrm{cm}^{-1}$. The Si-NP samples consisted of drop-coated Si-NPs on a silver coated glass substrate and the measurement took place ex-situ at room-temperature under inert conditions in a sealed box. The a-Si:H samples were measured under atmospheric conditions.

3.8 Photothermal Deflection Spectroscopy

Photothermal deflection spectroscopy (PDS) was used to quantify the fundamental and sub band gap optical absorption properties of the films in terms of the absorption coefficient α as a function of energy, as well as to probe the near range structural order of the layers as inferred from the band tail slope. PDS is an extremely sensitive technique and the measurement principle is as follows. A sample is immersed in CCl_4 and frontally irradiated with light of varying energy from ~ 0.4–$3\,\mathrm{eV}$ (corresponding to a wavelength in the range ~ 3000–$350\,\mathrm{nm}$). At the same time, a He-Ne laser beam passes parallel to the surface of the film at a distance of ca. 50 µm. The temperature of the film, and hence the heat dissipated into the surrounding CCl_4 is proportional to the amount of light that is absorbed by the film at any given wavelength. The refractive index of CCl_4 is temperature dependent so that small changes in it due to changes is absorption lead to corresponding deflections of the laser beam traversing in close proximity to the absorbing film. This deflection is subsequently used to arrive at a measure of the absorbance as a function of impinging photon energy $h\nu$, which is then used to derive the absorption coefficient α of the material for a known film thickness. The technique's insensitivity to pinholes and cracks in the film should be noted. The probed spot has an area of $\sim 1 \times 5\,\mathrm{mm}^2$ and an integrated irradiation power of $\sim 1\,\mu\mathrm{W}$. The characterisation was carried out on a-Si:H films of thickness ranging from 50–150 nm deposited on glass substrates using a home-made setup. For more details on this technique refer to [136–141].

3.9 Gas Chromatography-Mass Spectrometry

Gas chromatography-mass spectrometry (GC-MS) measurements are used to demonstrate the effects of ultrasound and UV light on the production of linear and branched silanes of the form Si_nH_{2n+2}, with $n > 3$. GC-MS allows us to temporally separate the different silanes along their path through the GC column due to their varying degree of interaction with the internal surface of the column. The analysis of the silanes was performed on a GC-MS system consisting of a *Trace GC* Ultra gas chromatograph with a programmed temperature vaporizing (PTV) injector and an ITQ 900 mass spectrometer (*ThermoFisher Scientific*, Waltham, MA, USA). Analytes were separated on a FS-Supreme-5 MS Plus column (60 m × 0.25 mm i.d., 0.25 µm film thickness, *Chromatographie Service*, Germany). Helium was used as carrier gas at a constant gas flow of 1.0 mL min^{-1}. The oven temperature program employed for analysis of silanes was as follows: 35 °C for 1 min, 3 °C min^{-1} to 150 °C, 10 °C min^{-1} to 340 °C. Injections of 1 µL were made in the PTV injector at a split ratio of 1:20 which was then heated up from 35 °C to 250 °C with 5 °C s^{-1}. The mass spectrometer was used in the electron impact (EI, 70 eV) mode and scanned over the range 25–900 m/z with an acquisition rate of 1 microscan (1 scan/s). The transfer line and ion source were kept at 140 °C. Data processing was performed using the *XCalibur* 2.0.7 software package (*ThermoFisher Scientific*). For more details on this analytic technique refer to [115–117].

3.10 Nuclear Magnetic Resonance

The ^{29}Si NMR measurements were carried out on a *Bruker* 600 Avance NMR spectrometer operating at 119.23 MHz. The spectrum was collected by using 65×10^3 data points over an acquisition time of 2 s, with a recycle delay of 300 s and recorded using inverse gated decoupling.

3.11 Size Exclusion Chromatography

The measurements are carried out using a *Polymer Laboratories* PL 220 SEC instrument equipped with a differential refractive index (DRI) detector and a *PolyPore* column. The instrument was operated at a temperature of 30 °C at a flow rate of $1\,\mathrm{mL\,min^{-1}}$. The measurements entailed i) comparing solutions submitted to sonication for increasing treatment times and ii) camparing sonicated solutions to similar ones having been submitted only to purely thermal treatment at temperatures typically reached during sonication. The molecular weight or more precisely, the mass average molar mass M_w , is estimated using polystyrene (PS) standards as molecular weight references and the formula

$$M_\mathrm{w} = \frac{\sum M_\mathrm{i}^2 N_\mathrm{i}}{\sum M_\mathrm{i} N_\mathrm{i}}, \tag{3.1}$$

where M_i and N_i are the mass of the i^{th}-molecule and the number of molecules with that mass, respectively. The PS standards are used to calibrate the retention time, t_r, that analytes require to elute through the SEC column with known molecular weights so that a calibration curve of M_w against t_r can be made. In addition to the PS standards, the peak for CO was also used as a reference at the low molecular weight end of the measurement range with $M_\mathrm{w} = 112.2\,\mathrm{g\,mol^{-1}}$ at $t_\mathrm{r} = 10.1\,\mathrm{min}$. The calibration curve for the SEC measurements is shown in *Figure* 3.2. The estimation of the M_w of the silicon hydride polymer solutions is then achieved by comparing the signal intensity measured by the DRI detector in the time period over which the polymer distribution spans.

A total of two SEC measurement runs were carried out. The first series of measurements was carried out using cyclohexene (CH) as SEC equipment solvent in order to estimate the M_w of the silicon polymer. The reason for this was that under the experimental conditions the PS standards were found to be soluble in CH, but not in cyclooctane (CO). Note that CO is the solvent used for the synthesis of the CPS-derived polymer via sonication. The second series was carried out using CO as SEC equipment solvent and was undertaken in order to monitor changes in CPS monomer concentration, the growth of higher silanes and to investigate the nature of the polymerisation process, i.e. to compare the effects of ultrasonic and

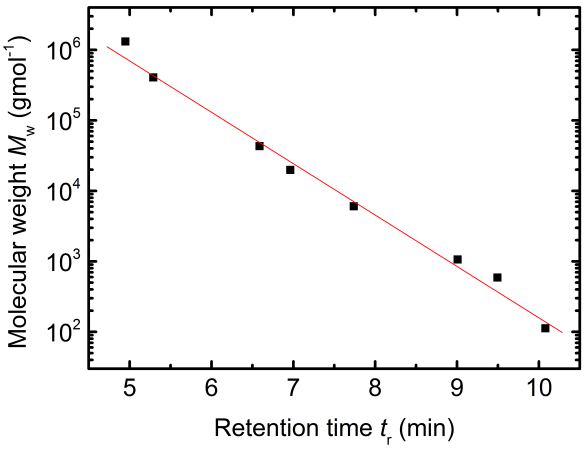

Figure 3.2: *Calibration curve of molecular weight diluted in cyclohexene versus retention time calculated using polystyrene standards. The data point at* 10.1 min *corresponds to pure cyclooctane with a* M_w *of ca.* 112 g mol^{-1}. *The red line is simply a guide to the eye.*

purely thermal treatment of CPS, respectively. The CH series had the drawback that both unreacted CPS monomer and CO were found to elute concurrently, thus the information on the changes in CPS concentration with increasing sonication time were inaccessible during this run (see *Section* 4.2 for more details). Here an 8.8 wt% CPS solution was used and the sonication parameters were: a duty cycle per second (DC) of 40 %, an amplitude (A) of 60 % (= 144 µm), a total treatment time of t_{treat} = 270 min (t_{eff} = 108 min) and a steady-state process temperature (T_{ss}) of 65–70 °C. Test samples for SEC analysis were taken from the untreated solution and after 90, 180, 220 and 270 min of sonication, respectively. For the CO series a 14.2 wt% CPS solution was used and the sonication conditions were: DC = 40 %, A = 50 % (= 120 µm), t_{treat} = 625 min (t_{eff} = 250 min) and T_{ss} = 70–75 °C. Here test samples were taken from the untreated solution and after 240, 390 and 625 min from the sonicated solution and after 625 min from the thermally treated solution, respectively. The SEC samples were diluted to about 0.3 wt% to avoid column overloading. All samples were filtered with a 0.2 µm PTFE syringe filter prior to both SEC characterisation and spin coating.

3.12 Electrical Conductivity Measurements

The characterisation of the a-Si:H layers by electrical conductivity measurements is carried out in order to quantify their optoelectronic performance and assess their utility in optoelectronic devices such as thin-film field effect transistors and photovoltaic cells.

The electrical conductivity measurements are performed at room temperature in vacuum using a Keithley 6517A electrometer to measure current with a voltage sweep between ± 100 V. The samples are tempered at 440 K for 30 min before measurement to remove any moisture film adsorbed on the surface of the films. The measurement configuration comprises two coplanar Ag electrodes deposited onto the silicon coated glass with a width of 5 mm and a gap between them of 0.5 mm. For the photoconductivity measurements, a xenon halogen lamp with approximate AM 1.5 illumination conditions is used.

Simple geometric considerations show that the coplanar dual-electrode architecture used enables a measurement of the lateral conductivity, σ, given by

$$\sigma = \frac{I}{U}\frac{l}{w \cdot d}, \tag{3.2}$$

where I is the measured current, U the voltage across the electrodes, l is the gap between the electrodes, w is the width of the electrodes, and d is the thickness of the film. Films measured in the dark yield the dark conductivity, σ_{d}, and measurement under illumination yields the photoconductivity, σ_{ph}, given by

$$\sigma_{\mathrm{ph}} = \sigma_{\mathrm{tot}} - \sigma_{\mathrm{d}}, \tag{3.3}$$

where σ_{tot} is the total conductivity measured under illumination. The distinction between σ_{ph} and σ_{tot} only becomes relevant when $\sigma_{\mathrm{ph}} \approx \sigma_{\mathrm{d}}$. The photo-sensitivity or photoresponse σ_{PR} of the films is then defined as the ratio

$$\sigma_{\mathrm{PR}} = \frac{\sigma_{\mathrm{ph}}}{\sigma_{\mathrm{d}}}. \tag{3.4}$$

3.13 Optoelectronic Device Characterisation

3.13.1 Photovoltaic Cell Contacting and JV Curve Acquisition

The cell architecture used was a n-i-p configuration on flat AZO coated glass. The n and p-type layers were deposited via PECVD. The reason for the use of this stacking order was that the n-type layer (on top of which the absorber layer is deposited) is found to be more robust and less affected by the high temperatures of $\sim 450\,^{\circ}\mathrm{C}$ required for the pyrolytic conversion of spin coated i-layers or the $\sim 400\,^{\circ}\mathrm{C}$ needed for the deposition of the i-layer via APCVD. The p-layer is subsequently covered with a shadow mask consisting of several square opening of $25\,\mathrm{mm}^2$ which define the area of the individual cells. The stack is then coated with an ITO (indium tin oxide) layer of $\sim 80\,\mathrm{nm}$ in thickness. The cells are deposited with a Ag grid for charge carrier extraction. The area of the ITO minus the area shadowed by the Ag electrode ($5.2\,\mathrm{mm}^2$) gives an effective area of ($19.8\,\mathrm{mm}^2$) for the solar cells.

The current density (J) versus voltage (V) curves are acquired using a *Keithley* 238 SMU (source measure unit) and are measured under AM 1.5G illumination conditions ($100\,\mathrm{mW\,cm^{-2}}$, $25\,^{\circ}\mathrm{C}$) using a Class A *WACOM* WXS-140S-Super solar simulator.

3.13.2 Characterisation of Surface Passivation Layers

The quality of the passivation of the c-Si wafer substrates was evaluated via effective minority charge carrier lifetime measurements carried out on a *Sinton Consulting* WCT-120 photoconductance instrument in TPC mode (transient photoconductance) [142].

Chapter 4

Results

This chapter deals with the main findings of this work. It begins with a somewhat phenomenological description of a general synthesis route for preparing a printable silicon polymer - silicon nanoparticle composite ink using trisilane as precursor via a combination of ultrasound and ultraviolet light. Also shown are a p-type formulation of this ink and an ink prepared using cyclopentasilane without the action of light. The inks are studied with a variety of techniques ranging from the molecular level using gas chromatography and nuclear magnetic resonance to the microscopic scale using size exclusion chromatography as well as scanning and transmission electron microscopy. The various inks are subsequently used to deposit hydrogenated amorphous silicon thin films via spin coating and atmospheric pressure chemical vapour deposition. The morphology, optical absorption, and band gap properties of the films are characterised using infrared and photothermal deflection spectroscopy. The films are also characterised electrically via dark and photoconductivity measurements. Finally, the utility of the thin films for optoelectronic devices is demonstrated by fabricating n-i-p thin-film solar cells and surface passivation layers.

4.1 Synthesis of Polysilane Inks from Trisilane

4.1.1 Ultraviolet Irradiation of Untreated Trisilane Solutions

As discussed previously, lower linear and branched silanes of the form Si_nH_{2n+2}, with $3 < n < 5$, are rather insensitive to irradiation by UV light. This makes

the synthesis of a higher silicon hydride from trisilane (TS) by photochemical means alone a challenging task due to the long irradiation times needed and the low polymer yields that result. It is known, however, that higher order silanes as well as "crude" silane mixtures composed of different silanes exhibit higher photosensitivity. This leads to enhanced rates of photochemical decomposition reactions of the respective silanes and hence a greater yield of both additional higher order silanes (in the present case higher than TS) and higher silicon hydride polymer [41, 64].

A number of tests were carried out using untreated solutions of TS to investigate its photosensitivity. For instance, an initially transparent 1 mL TS/CO solution of 37 wt% can be irradiated with 365 nm UV light with an intensity of 80 mW cm^{-2} for $\sim$ 50 hr before a slight colour change towards clear lemon-yellow is discernible. This colouration if associated with a higher silicon sub-hydride of the form -$(SiH_x)_n$-, with $1 < x < 2$ [26, 46] However, all attempts at fabricating a thin film via spin coating using solutions submitted to solely UV treatment were unsuccessful. In contrast, identical solutions subjected to prior treatment with ultrasound (amplitude $A = 192\,\mu m$, duty cycle $DC = 80\,\%$, sonication time $t_S \sim 250$ min) exhibit a lemon-yellow tinge after just 5–6 hr of UV irradiation and are typically suitable for spin coating or deposition via APCVD after another $\sim$ 20 hr of UV exposure.

4.1.2 Ultrasonic Irradiation of Trisilane Solutions

The inability to prepare a spin-coatable ink using UV treated TS solutions warranted the search for a method capable of producing a coatable ink or, at the very least, increasing the photosensitivity of TS to allow for the accelerated synthesis of a high molecular mass, low volatility silicon hydride polymer suitable for deposition via another technique such as APCVD.

To this end, solutions of TS in cyclooctane (CO) of between 30–50 wt% are prepared in glass vials and sonicated at 26 kHz with A ranging from 140–240 µm and DC of 60–80 %. In order to mitigate the evaporative losses accrued when TS solutions are sonicated at typical process temperatures of between 40–65 °C which

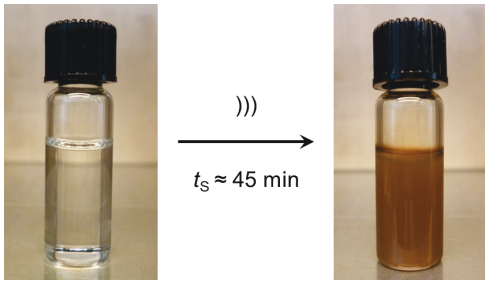

Figure 4.1: *Photographs depicting the colour and opacity changes of a typical* 30–50 wt% *TS solution after about* 45 min *of sonication at process temperatures between* −10 °C *and* 65 °C *using tip amplitudes of* 140–240 µm. *In general, the final colour and opacity, and the speed at which they are reached depends on a combination of sonication time, tip amplitude, and TS concentration.*

are reached without the use of active cooling, the sonication is usually carried out in the temperature range −5–10 °C using the Peltier cooling system described in *Section* 3.2.

As schematically illustrated in *Figure* 4.1, the sonication leads to visible changes of an otherwise initially transparent TS solution. Within the first 15 min of ultrasonic treatment time (t_{US}), which correspond to an actual sonication time, t_S, of $\sim$ 7 min, a slight colour change is already evident as a clear beige tinge. After about 30 min ($t_S \sim 15$ min) the solution has turned a clear vanilla colour. Under continued sonication the solution progresses through further colour changes from light orange, dark orange, maroon, and finally dark brown. If sonication if halted at any stage and the solution is allowed to settle, one discovers that it tends to increase in transparency and an accumulation of particles is observed at the base of the vial.

The colour variation of the solutions upon sonication is found to be caused by the synthesis of silicon nanoparticles (Si-NPs), the properties and details of which are discussed at length in *Section* 4.3. In general, for standard 30–50 wt% TS solutions (initially transparent) sonicated with an A of 140–240 µm one finds that the concentration of particles increases with increasing t_{US}. This, in turn, results in the progressively darker colour and decreasing transparency of the solution. The solutions are observed to acquire a light-beige colouration within the first

1–2 min, thereafter gradually turning light brown and finally dark, opaque brown after $\sim$ 45 min (see *Figure* 4.1). Variation of the *DC* simply results in changes to the time required to reach a particular colouration or opacity, i.e. is dependent on the particle and/or agglomerate production rate. Once the solution has reached a dark brown colour, sustained sonication results in a further darkening of the solution, on occasion even reaching an opaque brown-grey colour. After treatments for $t_S >\sim 45$ min, once sonication has been halted an accumulation of Si-NP agglomerates at the base of the glass vial is usually observed. It should be mentioned that the sonication of pure CO, the organic solvent used to dilute the TS, does not result in any discernible production of particulate material.

For relatively short t_S of less than $\sim$ 20 min, the particles or particle agglomerates appear to the unaided eye as a fine powder and the solutions are predominantly transparent, albeit possessing different shades of brown. For longer t_S exceeding $\sim$ 50 min, the agglomerates are noticeably larger and solutions turn darker and more opaque. Depicted in *Figure* 4.2, are SEM images on c-Si substrates of spin coated particles from relatively long syntheses of $t_S > 80$ min where the solution was dark brown. Shown in the low-magnification image **(a)** is a section of a partially interconnected film of micron-sized particles exceeding 20 µm. Upon further magnification, image **(b)** shows the high surface area and porous morphology of the particles. Zooming in further, image **(c)** reveals the presence of even smaller nano-sized particles on the parts of substrate not covered by the larger porous particles.

In contrast to particles synthesised after long treatments, short sonication runs of $t_S < 15$ min result in higher quantities of isolated nano-sized particles and significantly fewer micron-sized particles that do not surpass about 3 µm. As shown in the SEM images of *Figure* 4.3, again with increasing magnification from left to right, the wide field image in *Figure* 4.3a shows that presence of fewer and smaller $\sim$ 100 nm sized particles as compared to those visible in *Figure* 4.2a for longer t_S. Upon further magnification *Figure* 4.3b and *Figure* 4.3c demonstrate that the particles are noticeably smaller, rounder and more isolated from each other. Once more, much smaller particle in the range $\sim$ 10 nm are also discernible. Also visible is a featureless thin film covering the space between the particles, more clearly apparent in image **(c)** as the slightly darker regions surrounding the particles.

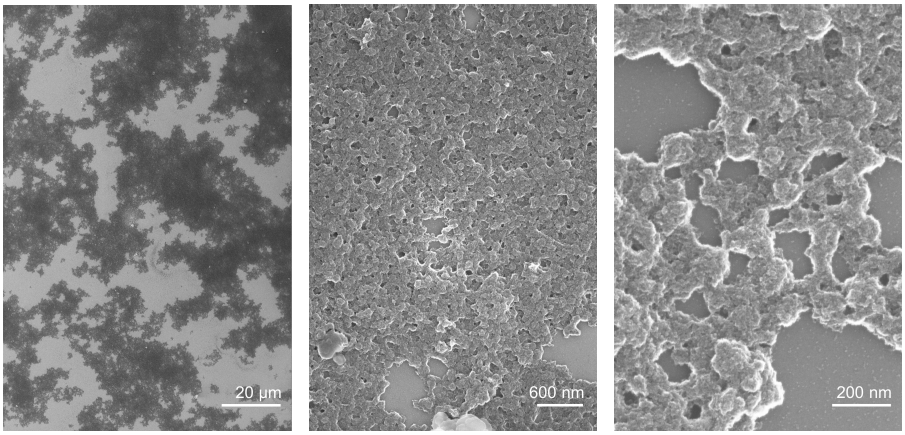

Figure 4.2: *SEM images depicting the morphology of spin coated particles on a c-Si substrate. The particles result from relatively long syntheses of* $t_S > 80\,\text{min}$ *and where the solution is not filtered. Upon increasing magnification from* ***(a)*** *to* ***(c)****, the micron-sized particles are seen to be highly porous and the existence of even smaller nano-sized particles on the substrate is also apparent in sections not covered by the larger agglomerates.*

We are hence able to attribute the colour changes that take place with increasing sonication time to the creation of solid particles. A correlation is found between the progression of colouration to darker colours and increasing colloid size (isolated particles or agglomerates) and/or particle concentration, where e.g. the lighter colours such as clear vanilla or light orange correspond to smaller colloids ($< 200\,\text{nm}$) and the darker ones such as opaque brown to the additional presence of larger colloids with sizes $> 10\,\mu\text{m}$. In general, solutions become darker and more opaque with increasing amounts of dispersed particles; this is observed even in solutions composed of concentrated amounts of smaller particle agglomerates that have been collected from several short sonication runs.

As shown in *Figure* 4.4a, the surface morphology of larger particles appears to be littered with fused particles of various sizes. For instance, observable in the central region of the image is a collection of $\sim 100\,\text{nm}$ sized particles in a porous formation and on the bottom right hand corner a larger $\sim 500\,\text{nm}$ sized particle with smaller $< 80\,\text{nm}$ sized particles on its surface. It is suggested that under certain conditions, larger particle agglomerates/aggregates in the micron range might be formed as

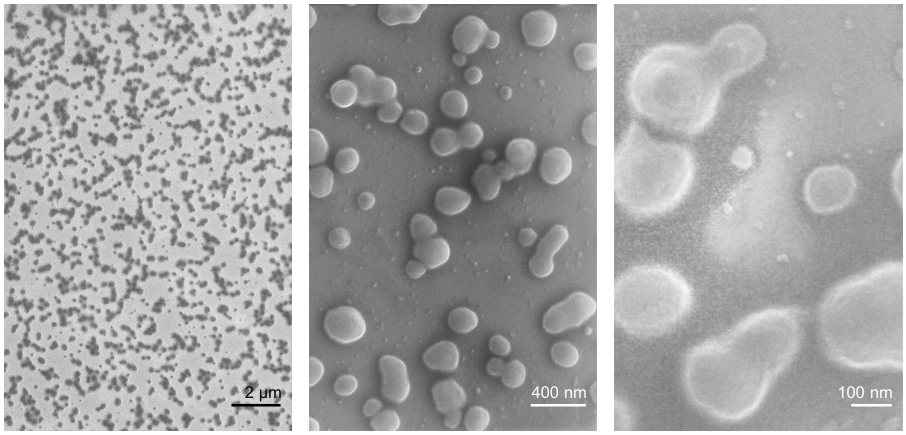

Figure 4.3: *SEM images depicting the morphology of spin coated agglomerates prepared in short sonication times of* $\sim 15\,\text{min}$ *where the colour of the solution was clear vanilla.* ***(a)*** *Well dispersed islands of colloids not exceeding about* $1\,\mu\text{m}$ *after deposition.* ***(b)*** *Zooming in reveals that the largest agglomerates are of the order of* $400\,\text{nm}$. ***(c)*** *Smaller Si-NPs and a thin featureless film of slightly darker complexion covering the spaces between agglomerates (also discernible in* ***(b)****).*

a result of local sintering during inter-particle collisions between initially smaller nano-sized particles [94].

The question arises as to the composition and morphology of the particles. Since no discernible reactions take place in solutions comprising solvent alone one would naturally expect that the particles produced using TS solutions should, at least in part, be composed of silicon.

For completeness, it should be mentioned that there is no evidence suggesting that large quantities of titanium are eroded from the ultrasonic horn during sonication, especially in the short treatment times needed for pre-treatment with ultrasound ($\sim 1\,\text{hr}$). Nevertheless, in order to rule out the possible effects of sensitization with Ti particles in solution, the following experiment was carried out. Pure cyclooctane solvent is sonicated for a total of $2\,\text{hr}$ before diluting trisilane in it. Thereafter, the TS/CO solution was irradiated with UV light and showed absolutely no colour change even after $55\,\text{hr}$, the same behaviour an untreated

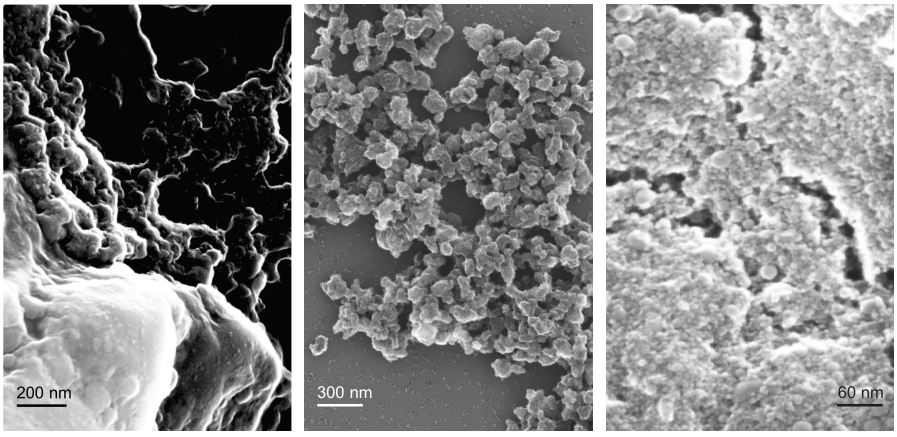

Figure 4.4: *(a) High magnification SEM image of the surface morphology of micron-sized Si-NP agglomerates. Such particles typically possess a porous and disordered structure and appear to be composed of smaller ts that appear to have been fused together under sustained ultrasonic irradiation.* ***(b)*** *Coral-like Si-NP agglomerate prepared by drop coating and after annealing at* 450 °C *for* 20 min. ***(c)*** *Close-up SEM image highlighting the retained high surface area and corpuscular morphology of annealed Si-NP agglomerates.*

TS/CO solution shows upon UV irradiation. It is hence concluded that if Ti particles are eroded during sonication, that these do not function as catalysers or photosensitisers during the UV irradiation of trisilane.

As will be considered below in more detail in the context of UV irradiation of TS solutions, the role of the Si-NPs is still a matter of investigation and the enhanced photosensitivity to UV light of sonicated solutions may involve the particles increasing the reaction cross section due to light scattering or concerted reactions at their surfaces in direct contact with the silane mixture.

4.1.3 Irradiation of Sonicated Trisilane Solutions with UV Light

We now investigate the effects of irradiating already sonicated TS solutions with UV light. As demonstrated previously, approximately $\sim 50\,\text{hr}$ of photolysis are required to detect visible changes to untreated TS solutions. Subsequent attempts at spin coating thin films using these solutions were unsuccessful. As was shown in *Section* 4.1.1, however, UV irradiation eventually does result in the formation of higher silanes. In principle, this makes deposition via APCVD using TS solutions subjected to extended UV treatment alone also possible.

Solutions that have undergone ultrasonic treatment for $\sim 90\,\text{min}$ (corresponding to $t_\text{S} \sim 45\,\text{min}$) so that they appear opaque brown are typically used for subsequent photolytic treatment using UV light (*Figure* 4.5). Here 30–40 hr of UV treatment is required to produce a spin-coatable ink. However, longer sonication runs with $t_\text{S} \sim 300\,\text{min}$ result in clear, light lemon yellow coloured solutions after filtering, without the action of UV light. This suggests that sonication alone can lead to discernible quantities of the highly branched silicon hydride polymer associated with the yellow colouration. In contrast to untreated TS solutions or sonicated solutions with $t_\text{S} \sim 45\,\text{min}$, these solutions reach an intense lemon yellow colour after just $\sim 6\,\text{hr}$, where continued irradiation for between 20–30 hr results in a spin-coatable ink.

It can also be shown that the presence of particles larger than 100 nm is not strictly necessary for the preparation of the ink. For instance, a TS/CO solution is submitted to a sonication for $t_\text{S} = 50\,\text{min}$ after which it is opaque brown. The solution is subsequently filtered with a 0.1 µm PTFE filter to remove all particles exceeding 100 nm in size and is then irradiated with 365 nm UV light. After approximately 24 hr a tinge of yellow is discernible and after 35–40 hr the solution takes on the familiar bright lemon-yellow colour.

It hence appears that the presence of at least one of the following three constituents is required for the preparation of the printable ink with shortened subsequent UV irradiation. The first species that might be required are particles of various

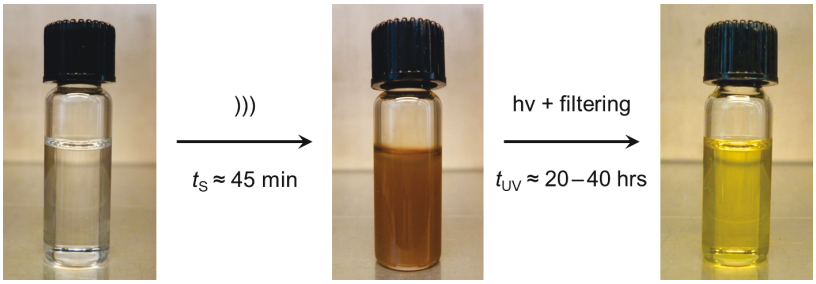

Figure 4.5: *Steps required to arrive at a printable ink using a TS solution. After a sonication time t_S of about* 45 min*, an opaque brown solution is irradiated with UV light for between* 20–40 hr *with a magnetic stirrer and is subsequently filtered with a* 0.1 µm *PTFE filter. The resulting solution exhibits a clear, lemon-yellow colour and can be used to deposit thin films of silicon hydride polymer. In general, the intensity of the lemon-yellow colour and the irradiation time after which it is observed (after filtering) depends on a combination of t_S, tip amplitude A, and TS concentration c_{TS}.*

sizes. As mentioned above, sonicated opaque brown solutions that appear clear beige after filtering also yield similar inks in comparably short UV treatment times. This suggests that particles smaller than 100 nm could play a role, but does not rule out potential contributions from larger particles, e.g. photochemical reactions at their surface. Secondly, the enhanced photo-initiated polymerisation may be attributed to lower silanes higher than TS of the form Si_nH_{2n+2} (both linear and branched). Thirdly, the presence of a higher silicon hydride or hydridosilane of the form -$(SiH_x)_n$- might be responsible for promoting the growth of a particular class of silicon sub-hydrides responsible for the lemon-yellow colouration observed after treatment with UV light.

We observe mostly light out-gassing or bubbling, but at times also intense bubbling of the solution upon reopening the vial after UV irradiation. The gaseous species that are released were not collected for analysis in the present work, but they are believed to be one or a combination of either H_2, SiH_4, Si_2H_6. With reference to *Figure* 4.10, a Si_2H_6 (disilane) singlet was recorded in the ^{29}Si NMR spectrum of a sonophotolytically treated solution, indicating that some disilane was still dissolved in the liquid during characterisation.

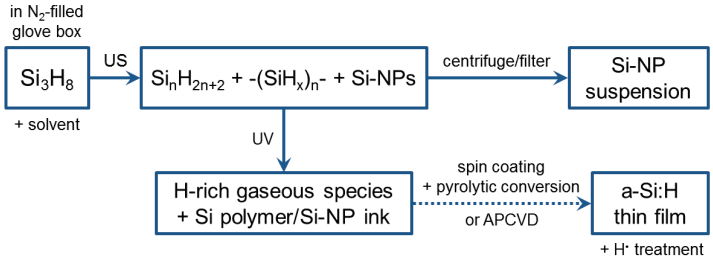

Figure 4.6: *Scheme summarising the processing steps for the fabrication of the TS based ink in N_2 atmosphere. The initial treatment of a TS solution with ultrasound (US) leads to the production of a homologous series of silanes (Si_nH_{2n+2} with $3 < n < 9$), small amounts of a higher silicon hydride (-$(SiH_x)_n$-) and silicon nanoparticle(s) (Si-NP(s)). The solution can be centrifuged or filtered and then used to prepare a Si-NP suspension. Alternatively, the solution can be subsequently irradiated with UV light. This results in the further growth of -$(SiH_x)_n$- and the production of gaseous by-products such as disilane. As an example, the fabrication of a-Si:H thin films via spin coating or APCVD with subsequent $H^\bullet$ treatment is provided.*

4.1.4 UV-Vis Transmission Measurements

The colouration of treated TS solutions was alluded to in the previous chapter and is a central consequence of the chemical changes undergoing in the solution upon irradiation with both ultrasound and UV light. The following transmission measurement results aim to elucidate some of the optical effects observed during the preparation of the polysilane ink.

As mentioned previously, undiluted and untreated TS, as well as CO solutions thereof are almost completely transparent for visible and UV light. Shown in *Figure* 4.7 are UV/Vis transmission (T) spectra as a function of wavelength λ for untreated TS and two treated TS solutions. Also shown in the plot is the position of the 365 nm wavelength LED laser array used for the UV treatment. The cyan curve corresponds to pristine trisilane and was derived from absorption measurements by Fehér [32]. This explains why untreated TS is insensitive to the UV light used in the experiments and helps clarify why the polymerisation via UV treatment alone proceeds at such a slow rate. In stark contrast, the brown curve at the bottom at the bottom of the plot corresponds to a sonicated solution

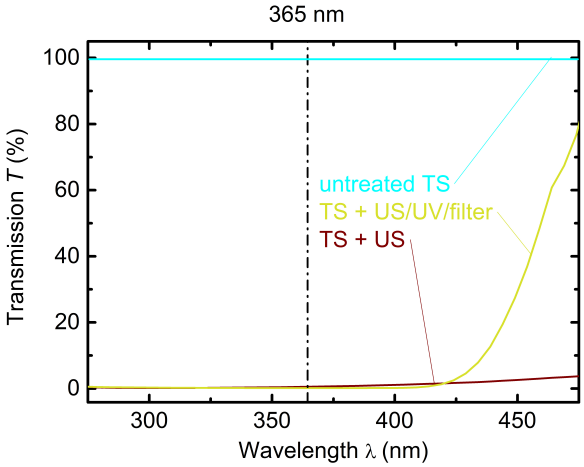

Figure 4.7: *Transmission (T) measurements as a function of wavelength λ carried out on treated and untreated solutions in hermetic quartz tubes. The cyan curve shows the T of untreated trisilane as derived from absorption measurements by Fehér [32]. The line shows that trisilane is essentially completely transparent in the spectral range from* 275–475 nm. *The brown curve corresponds to a solution sonicated for* 200 min *and the yellow curve is for the same solution after* 680 min *of irradiation with UV light and subsequent filtering. The vertical dashed line corresponds to the* 365 nm *UV laser diode array used in the fabrication of the ink.*

which appeared dark opaque brown to the naked eye and evidently absorbs most incoming light in the shown spectral region. This solution underwent sonication for $t_S = 200$ min. This solution exhibits a transmission $T < 5\,\%$ throughout the entire range and at 365 nm, T drops to less than $\sim 0.5\,\%$. The fact that sonicated solutions exhibit such high absorbance, with over 99 % of incoming light being absorbed, helps explain why they demonstrate enhanced photosensitivity upon irradiation with 365 nm UV light.

The yellow curve corresponds to the measurement of a clear lemon-yellow solution that results upon subsequent irradiation of the sonicated solution with UV light for 680 min and filtering with a 0.1 µm PTFE filter. This solution likewise demonstrates enhanced absorption over a wide spectral range. In particular, for wavelengths of 420 nm and below the solution transmits $< 2\,\%$ of incoming light

and at 365 nm has a transmission T of $\sim 0.1\,\%$. The curve also shows an absorption edge beginning at around 475 nm down to 420 nm, where the transmission remains relatively flat at a value of around 0.1 %. These results also explains why the finished ink has a lemon-yellow colour, the reason being that all wavelengths ≥ 450 nm corresponding to the blue region of visible light are strongly absorbed and hence the transmitted or reflected light appears yellow.

Lastly, the transmission measurements reveal the surprising result that yellow-lemon solutions possess comparable, if not superior, absorption for wavelengths below 420 nm, precisely in the range of the UV light used to photolytically polymerise previously sonicated solutions. This finding suggests that it should be possible to mix in a small amount of highly absorbent ready-to-use ink into an untreated TS solution to function as "seed" to enhance the rate of photo-induced polymerisation. This has indeed been attempted and successfully used to prepare new solutions via UV irradiation in shorter times than those required with untreated TS solutions, but without the need for additional treatment with ultrasound. For example, instead of a 1.2 mL, 31 wt% TS solution requiring ~ 50 hr to turn lemon-yellow, a solution that was prepared with 25 vol% of a similar, but already lemon-yellow solution requires just 30 hr to reach a comparable colouration.

4.1.5 Gas Chromatography-Mass Spectrometry

In order to highlight the distinction between photolysis and sonication, and the way they modify TS at the molecular level, gas chromatography - mass spectrometry (GC-MS) was applied to characterise treated and untreated TS solutions. The method enabled the detection of TS and higher order silanes, both linear and branched of the general form Si_nH_{2n+2} with $3 < n < 9$.

Plotted in *Figure* 4.8 are a number of gas chromatograms depicting the relative abundance of the various generated lower and higher order silanes as a function of retention time for various treated and untreated TS solutions. To facilitate the visualisation of silicon-containing molecules only, the plot shows ion chromatograms of molecular species in the retention time range from 2–40 min with mass-to-charge ratio (m/z) in the limited mass range between 114–120 amu.

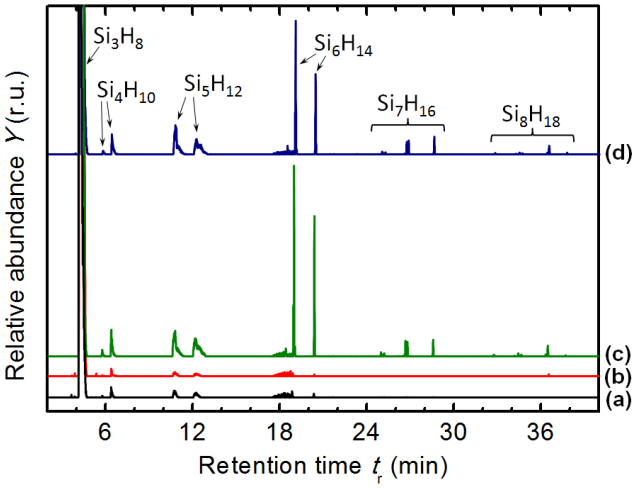

Figure 4.8: *Gas chromatograms depicting the effects of UV irradiation, ultrasonic treatment, and a combination thereof on TS solutions. Chromatogram* ***(a)*** *corresponds to pristine TS,* ***(b)*** *shows that* 120 min *of UV irradiation yields little to no higher silanes,* ***(c)*** *depicts the dramatic effects of* 120 min *of US on the production of higher silanes up to octasilane (Si_8H_{18}), and* ***(d)*** *shows the slight, yet detectable reduction in the concentration of most silanes after irradiating sample* ***(c)*** *with UV light for* 120 min.

This has suppresses most hydrocarbon peaks, in particular the broad signal from 17.5–19 min corresponding to the solvent (CO). Three identical untreated solutions consisting of TS diluted in CO to 47 wt% were prepared, one of which was used for the acquisition of the reference chromatogram **(a)** (black) corresponding to pristine TS as measured using GC-MS. The first and most intense peak on the left at around 4.4 min corresponds to TS and has been cropped at the top of each chromatogram. It is immediately evident that even a pristine TS solution contains small amounts of higher silanes up to hexasilane (Si_6H_{14}), however, the combined total relative concentration of these being extremely low at an estimated 0.01 rel%. The iso-silanes or i-silanes for short, i.e. silanes possessing at least one branching point, are expected to elute faster through the CG column than their linear counterparts, the n-silanes. This is due to the greater degree of interaction of a linear molecule with the inner surface of the column or equivalently, due to the lower effective interaction surface of branched molecules with the column walls as a result of steric hindrance.

The results of irradiating a TS solution with UV light for 120 min is shown in chromatogram **(b)** (red). Here, little to no production of higher silanes is observed. In stark contrast, chromatogram **(c)** shows the effect of submitting an identical TS solution to 120 min of sonication at −5–10 °C, where the production of higher silanes from tetrasilane (Si_4H_{10}) through to octasilane (Si_8H_{18}) is clearly evident. The silanes are observed to elute in approximately equispaced groups, which is indicative of a homologous series [30, 143]. This simplifies their identification, where in general the first peak of each group corresponds a more compact branched i-silane with less affinity for the column material, e.g. i-Si_4H_{10}, i-Si_5H_{12}, etc. On the other hand, the last member to elute is the linear member, i.e. n-i_4H_{10}, n-Si_5H_{12}, etc., exhibiting the strongest retention. Sonication is thus found to yield far superior yields compared to irradiation by UV light. Chromatogram **(d)** (blue) corresponds to the same solution depicted in **(c)**, but in addition to the US treatment, it was subsequently submitted to 120 min of UV irradiation. Close inspection of the peaks reveals a general decrease in intensity after irradiation. This is most clearly apparent for the hexasilane (Si_6H_{14}) peaks.

This observation suggests a plausible explanation for the observed photolytic synthesis of high molecular mass polymers in much shorter times when a sonicated TS solution is used instead of an untreated one. It appears that the presence of additional silanes might be responsible for the rapid synthesis of still higher silanes in the homologous series as well as higher hydridosilanes of the form -$(SiH_x)_n$- not measurable using this technique, but inferred from the lemon-yellow colouration of the ink. As reported by Fischer, the higher the order of the silane, the higher its photosensitivity becomes [41]. Moreover, he observed that crude silane solutions containing a mixture of different silanes are more sensitive to UV light than pure solutions of the respective silanes. Hence, one of the effects of ultrasound in the solution is the generate silanes other than TS and thereby ultimately enhancing the conversion efficiency into low volatility polymer products. As will be discussed at length in a subsequent, the other effect that ultrasound brings about is the generation of Si-NPs, which may also have a role to play in enhancing the photosensitivity of sonicated solutions.

As illustrated for selected silanes in *Figure* 4.9, the respective silanes can be identified by their characteristic mass spectra. The fine structure evident in each

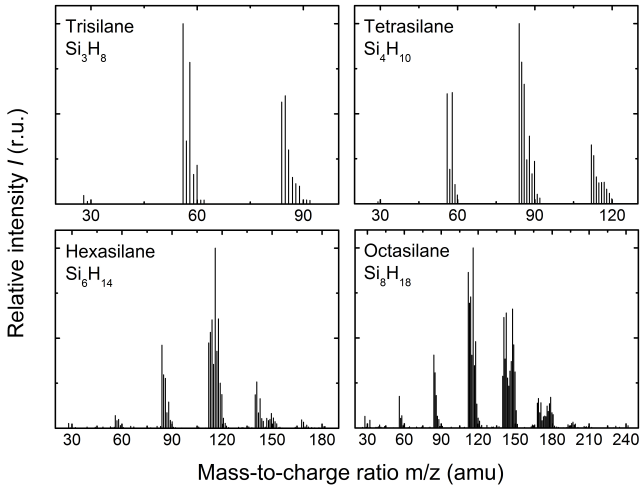

Figure 4.9: *Several exemplary mass spectra corresponding to selected silanes from the chromatograms in Figure 4.8. The spacing between silicon clusters is approximately* 32 amu*, corresponding to the atomic mass of an intact monosilane molecule.*

cluster is related to the occurrence of natural silicon isotopes and well as molecular fragmentation and hydrogen evolution in the mass spectrometer itself. The relative intensity differences between the clusters and in the clusters themselves is simply related to detection frequency. For instance, intact trisilane molecules with a mass of ca. 92 amu are observed to endure ionisation during detection in the spectrometer, while hexasilane and octasilane with a mass of ca. 182 amu and 242 amu, respectively, almost completely fragment into lower silane clusters during the detection process. This phenomenon also highlights the instability of silanes, where this type of fragmentation is not observed, for instance, in the more stable and structurally analogous alkanes.

4.1.6 Nuclear Magnetic Resonance

In order to examine the molecular structure of the finished silicon hydride polymer ink nuclear magnetic resonance (NMR) is used. NMR is useful in this regard in

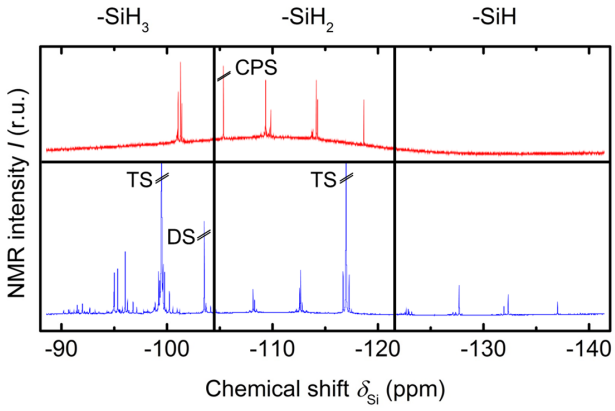

Figure 4.10: *^{29}Si NMR spectra of the finished silicon ink with TS as precursor after sonication and UV irradiation (blue) and for comparison purposes that of a CPS-based polymer solution prepared via UV irradiation. The abscissa has been subdivided into three ranges corresponding to the -SiH_3, -SiH_2 and -SiH groups. The peaks for unreacted TS (cropped at the horizontal line in the middle), disilane (DS) and unreacted cyclopentasilane (CPS) were not included in the calculations.*

that it allows for an inspection of the presence or absence of characteristic Si-H and Si-HSi bonding configurations. These include the -SiH_3, -SiH_2, -SiH and Si_2-Si-Si_2 groups, the latter of which refers to a fourfold-coordinated Si atom.

Figure 4.10 shows ^{29}Si NMR spectra of a silicon ink prepared from a 40 wt% TS solution by sonolysis for t_S = 90 min and UV irradiation for 28 hr and an ink prepared from cyclopenasilane (CPS, Si_5H_{10}) by UV irradiation of a 9 wt% solution for 135 min. The abscissa has been subdivided into three distinct regions associated with the SiH_3, SiH_2, and SiH groups mentioned previously. Note that no fourfold-coordinated Si was detected. A calculation of the integrated intensities of the peaks in these three regions reveals that the TS ink has an SiH_3:SiH_2:SiH ratio of approximately 4:4:1, while the proportionality for the CPS ink is 3:2:0. This demonstrates that the polymer in the TS ink possesses simple one-sided branching points of the form (SiH)-Si_3- and not double-sided branching point (since no Si_4 groups were detected). On the other hand, the CPS-based ink exhibits no branching and hence the dissolved polymer can be described as a polydihydrosilane with the generic form -$(SiH_2)_n$- consisting of predominantly linear chains.

4.1.7 Pyrolytic Treatment of Trisilane Solutions

Without active cooling during sonication, TS solutions are unintentionally heated up by the ultrasonic horn in direct contact with the bulk of the liquid. For typical sonication parameters with a maximum amplitude at the tip of 25–45 µm and a duty cycle of 20–40 %, and without the aid of active cooling, solutions reach process temperatures of 45–75 °C. The typical process duration is between 80–180 min.

A number of experiments are carried out in order to test whether TS will react at these relatively low temperatures. In particular, it was investigate whether particle formation or colour changes of any sort are discernible upon prolonged thermal treatment at the typical process temperatures encountered during sonication.

For instance, a 1.2 mL TS solution in CO diluted to 25 wt% is heated up to between 60–65 °C. After about 2 hr fresh TS is added to offset evaporative losses and restore the solution to its original volume. The loss of volume is attributed to preferentially evaporated TS due to its much lower boiling point of bp = 53 °C compared to bp = 151 °C for CO. The solution is heated for a total of 700 min, after which no colouration or particulate matter is observed. The solution is subsequently used to attempt to deposit a thin film of silicon hydride polymer on a glass substrate via spin coating. Poor wetting is noted and no layer is discernible on the substrate.

Heating of similar solutions at lower temperatures of between 40–50 °C for several hours results in somewhat slower evaporation of the solution, albeit yielding the same negative end result of no colouration or particle formation of any kind.

The aforementioned attempts at pyrolytic polymerisation or decomposition of TS at such low temperatures are somewhat unsurprising in light of the fact that previous studies have shown that TS only begins to decompose at temperatures exceeding 260 °C [34, 35, 42]. These results clearly indicate that the observed phenomena are not thermically initiated due to the temperature of the solution itself, but rather that they must necessarily stem from acoustically-induced effects. The reader may refer to similar discussions in connection with sonicated CPS solutions (*Section* 4.2.1) and Si-NP synthesis from TS (*Section* 4.3).

4.1.8 Preparation of p-Type Inks using Decaborane and Trisilane

Following the general guidelines for the preparation of doped polysilane inks from cyclopentasilane (Si_5H_{10}) and neopentasilane ($Si(SiH_3)_4$) found in the literature [13, 14], in this section a simple recipe for the synthesis of a p-doped formulation of a polysilane ink using TS and decaborane (DB, $B_{10}H_{14}$) is outlined.

Prior to usage, DB (bp = 213 °C) is purified via sublimation using a pair of glass petri dishes. Small quantities of DB are placed on the base dish and covered by an inverted upper dish. The dishes are then slowly heated up to about 250 °C upon which a white vapour fills the confined volume. After some minutes the upper dish is removed and a thin layer of condensed DB is found on its base. The purified DB is subsequently scraped off and collected for use. This procedure can be repeated several times depending on the amount required.

Typically, 40 wt% TS/CO solutions of $\sim$ 1.2 mL are prepared and mixed with 42–85 mg of DB giving solutions with DB concentrations of 1–2 wt%. The mixture is then submitted to sonication for $t_S \sim 50$ min at process temperatures ranging from 5–20 °C. Next, the mixture is irradiated with 365 nm UV light for about 20 hr. Finally, the solution is filtered with a 0.1 µm PTFE syringe filter after which it appears clear light lemon yellow. The use of DB in concentrations exceeding about 3 wt% is found to result in solutions that do not produce usable inks after UV irradiation. As of this writing, the reason for this observation has not been clarified.

In this study, the p-type ink is exclusively used for the deposition of thin films via APCVD in N_2 atmosphere and no attempt at developing a spin-coatable ink was undertaken. The results of characterisation via electrical conductivity measurements of the highly conductive layers that can be fabricated using the p-doped ink can be found in *Section* 4.5.3.

4.1.9 Summary of Polysilane Ink Synthesis from Trisilane Precursor

The main objective of developing a general recipe for the synthesis of a silicon polymer ink or as it turns out, a silicon polymer - silicon nanoparticle composite ink using a combination of sonolytic and photolytic treatment in relatively short times has been demonstrated. In general it is found that solutions submitted to longer ultrasonic treatment times require shorter post-treatment with UV light.

The method involves an initial sonication step that exploits the chemical effects associated with acoustic cavitation. Sonication leads to the production of silicon colloids which vary in size from several nanometres to several microns. Apart from macroscopically observable changes to trisilane solutions in the form of colour changes and accumulation of particulate matter at the base of the reaction vials, SEM and TEM were used to ascertain both the existence of isolated nanoparticles, as well as their chemical composition.

We showed that untreated trisilane solutions are transparent and rather insensitive to irradiation with 365 nm ultraviolet light, where it was not possible to prepare a printable ink via photolysis in the same amount of time as that needed for similar solutions submitted to prior sonication. The findings point towards the need for the presence of UV "photosensitisers" that enhance the absorbance of the solutions and hence allow for a more rapid preparation of the polysilane ink from trisilane. The species responsible for the enhanced photosensitivity could be the higher order silanes that are generated upon sonication. This proposition is consistent with observations made by Fischer [41] where crude silane solutions containing a mixture of different silanes were found to be more sensitive to UV light than pure solutions of the respective silanes. The role of the silicon nanoparticles is still a matter of investigation, where they too might contribute to enhancing the photosensitivity by increasing the reaction cross section due to light scattering or via concerted reactions at their outer surfaces in direct contact with the silane mixture.

Analysis via gas chromatography - mass spectrometry demonstrates that compared to ultraviolet treatment, the initial sonication step is an effective way of

generating a homologous series of silanes from tetrasilane up to octasilane. In fact, ultraviolet light alone yielded no higher order silanes under the conditions in which the experiments were performed.

Although observation by the unaided eye of colouration changes in solutions subjected to sonication point to the production particulate matter, it was through scanning and transmission electron microscopy that the existence of micro and nanoparticles could be definitively ascertained. The particles are found to be amorphous and range in size from $\sim 5\,\mathrm{nm}$ to agglomerates of $10\,\mu\mathrm{m}$ or larger. Electron energy loss spectrometry and Fourier transform infrared spectroscopy reveal that the particles are composed of unoxidised elemental silicon and bonded hydrogen.

Irradiation of sonicated trisilane solutions with ultraviolet light produces an ink possessing a clear, lemon-yellow colour. With reference to known literature [46] concerning the observed colouration and in conjunction with nuclear magnetic resonance measurements, the growth of a branched higher silicon sub-hydride polymer of the form -$(SiH_x)_n$-, with $1 < x < 2$ is indirectly inferred. The ready-to-use trisilane based ink was hence found to consist of three main types of silicon-containing species, namely a homologous series of silanes, a silicon hydride polymer and silicon nanoparticles.

4.2 Synthesis of Polysilane Inks from Cyclopentasilane

As discussed in *Chapter* 2, cyclopentasilane (CPS, Si_5H_{10}) was the first precursor used to demonstrate the preparation of a-Si:H thin films from a liquid silane. The method employed by Shimoda et al. involved the irradiation of CPS with UV light to initiate the growth of a high molecular weight polymer via light-induced ring-opening polymerisation (ROP). In the following an alternative method of preparing a spin-coatable ink from CPS based on ultrasonic means is demonstrated, and not requiring the action of UV light at any stage of the processing.

Solutions of CPS diluted in CO can be prepared of various concentrations. However, these typically have rather low CPS content compared to TS in TS/CO solutions due to monomer cost considerations (see *Introduction*). Inks used to produce a-Si:H thin film via spin coating are usually prepared in 0.5–1.0 mL batches of 8–15 wt% and require an ultrasonic treatment time t_{US} of between 270–600 min depending on the duty cycle employed. This corresponds to an actual sonication time t_S of 100–300 min. The maximum amplitude at the sonotrode tip is usually 120–145 µm. The process temperature during sonication when no active cooling of the solution is used is typically limited to $< 70\,°C$ to avoid additional contributions from thermally-initiated decomposition reactions of CPS. With active cooling, sonication is usually carried out at 20–40 °C.

As-mixed CPS/CO solutions are initially transparent, but go through colour changes as sonication progresses (see *Figure* 4.11). After $t_S \sim 75$ min a clear, slight vanilla-yellow colouration is discernible. The colouration remains essentially the same until $t_S \sim 100$ min where the solution begins to show signs of turbidity. For increasingly long $t_S > 250$ min, the solution is usually opaque milky white indicating the precipitation of high molecular weight polysilanes out of solution. After sonication the solution is filtered to remove insoluble precipitates. The solution is now transparent and usually remains so for about 30 min, after which it becomes turbid once again (without any further irradiation). This indicates rather poor solubility of the polysilanes in CO and can, in principle, be mitigated by using a higher concentration of CPS in the solution since the polysilanes are known to be soluble in the unreacted CPS monomer itself.

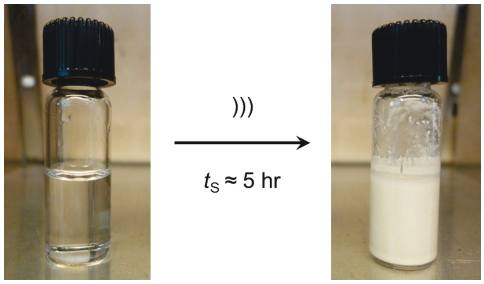

Figure 4.11: *Photographs depicting the colour and transparency changes of a typical* 30–50 wt% *CPS solution after about* 300 min *of sonication at process temperatures* 70–75 °C *using tip amplitudes of* 120 µm. *In general, and as is the case for TS solutions, the colour and opacity changes, and the speed at which they are reached depends on a combination of factors such as sonication time, tip amplitude, and CPS concentration. After filtering, CPS solutions usually remain transparent for* ∼ 30 min *before becoming turbid once again.*

4.2.1 On The Non-"Macrothermal" Nature of the Sonolytic Treatment

It is a well-established fact that silane molecules can be pyrolytically decomposed into lower and higher silanes via disproportionation reactions [42]. For TS, for instance, the threshold temperature has been reported at 260 °C [34]. However, silanes such as cyclopentasilane (Si_5H_{10}, CPS) are also known to undergo slow polymerisation over several months even at room-temperature. In order to investigate whether the polymerisation process initiated via sonication is thermal or sonocatalytic in nature, a number of experiments with both TS and CPS were carried out.

In general, the temperature of a solution rises during ultrasonic treatment. This unintentional heating is caused by friction of the horn with the liquid and the injection of sonic power. Without the aid of active cooling a steady-state temperature of anything between 30–100 °C reached after about 20 min which is found to depend on the amplitude (A), duty cycle (DC), the immersion depth of the tip in the solution, and the volume of liquid being sonicated. Typically, active cooling during sonication enables the temperature of the solution to be held between −15–40 °C. The temperature of the solution is referred to as the "macroscopic" temperature of

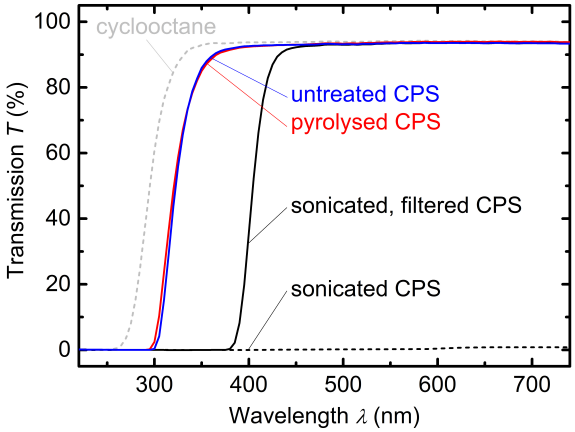

Figure 4.12: *Transmission (T) spectra of various CPS solutions in the wavelength range from* 220–740 nm. *Shown in blue is the curve for untreated CPS, the red curve corresponds to a CPS solution thermally treated at* 75 °C, *the dashed black curve corresponds to a CPS solution sonicated at the same process temperature of* 75 °C, *and the solid black line corresponds to the sonicated solution after filtering. Since cyclooctane is the solvent used to dilute the CPS monomer, the T of pure cyclooctane is included as reference (dashed grey curve).*

the solution when being discussed in the context of the mechanism responsible for the polymerisation of CPS and to differentiate it from the inferred and localised "microscopic" temperature of the hot spot generated at imploding microbubbles.

4.2.1.1 UV-Vis Transmission Measurements

In order to spectrally study the aforementioned colour and transparency changes that are observed after sonicating CPS solutions, as well as to show that the initiation of the polymerisation is sonocatalytic and not macrothermal in nature, additional ultraviolet-visible optical transmission measurements were conducted on treated and untreated solutions.

Shown in *Figure* 4.12 are the transmission spectra from 220–740 nm of an untreated CPS solution (blue), a solution pyrolysed at 70–75 °C for 625 min (red), a

solution sonicated at this same process temperature for the same amount of time (dashed black), and of the same sonicated solution after filtering (solid black). The fact that the blue and red curves again overlap demonstrates that the solution remains essentially unchanged after pyrolysis. This suggests that no polymerisation via thermally activated bond cleavage has taken place. The solution remains transparent in the whole visible range, consistent with an absorption edge at about 320 nm. On the other hand, the sonicated solution prior to filtering had become milky white and its transmission spectrum indicates that it is almost completely opaque. After filtering out the precipitated polymer, the solid black line shows that the solution appears transparent once more. However, the absorption edge has now shifted to about 400 nm indicating that higher silicon hydrides have been formed [57].

4.2.1.2 Comparison of Pyrolysis and Sonolysis of Cyclopentasilane Solutions via Size Exclusion Chromatography

In order to scrutinise the nature of the polymerisation process further, CPS is chosen since it constitutes a more sensitive molecule which is known to polymerise at temperatures as low as 80 °C and even gradually polymerise at room-temperature over some months. In particular, the question is addressed as to whether or not the polymerisation process is due to acoustic cavitation or simply due to thermal activation from unintentional heating of the solution by the ultrasonic horn during sonication.

To this end, a $\sim$ 1.0 mL solution of CPS in CO of 14 wt% is sonicated with an A of 60 % and a DC of 30 %. During the present experiment, the solution reached a steady-state process temperature of $\sim$ 65 °C after about 15 min of ultrasonic treatment. *Figure* 4.13 shows typical temperature increases of solutions unintentionally heated during sonication as measured using a thermocouple in direct contact with the liquid. In general, the steady-state temperature depends on a combination of factors, including the A, DC, and submersion depth of the sonotrode in the solution. A similar solution in a glass vial is also prepared and is brought to the same process temperature on a hot plate under constant stirring with a magnetic stirrer. Both solutions are treated for a total of 625 min.

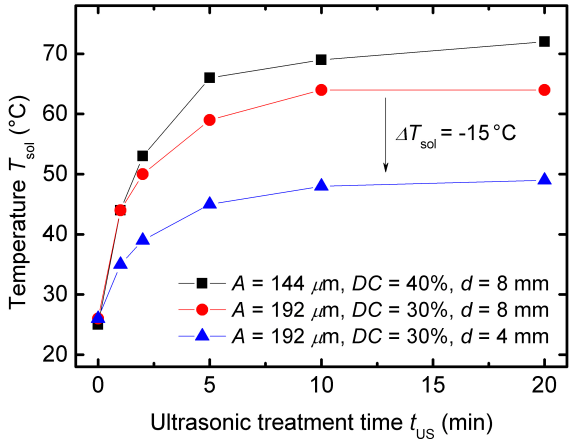

Figure 4.13: *Typical process temperatures reached by the solution during sonication without the aid of active cooling. The variation in steady-state temperature is a consequence of the interplay between a number of factors, these include the A, DC, and submersion depth d of the sonotrode in the solution. The drop in temperature of* $-15\,°C$ *results from simply changing the d of the tip.*

Size exclusion chromatography (SEC) is then used to follow changes in molecular mass, if any, of the solutions before and after heat and/or ultrasonic treatment. The results are presented in *Figure* 4.14. The elugrams in *Figure* 4.14a depict the silicon hydride signal intensity measured by the refractive index (RI) detector as a function of elution time t_{elu}. Since no molecular mass standards were used in the present experiment, the abscissa is inversely proportional to the molecular mass. As explained in more detail in *Section* 3.11 this means that, in general, the shorter the elution time, the larger the molecular mass. Also, the signal intensity (I_{RI}) is proportional to the amount of a particular polymer that is present at any given elution time.

In *Figure* 4.14a, the blue curve shows the untreated CPS/CO solution and the main peak at around 10.45 min corresponds to unreacted CPS monomer. Peak 1 and peak 2 at earlier t_{elu} of 9.75 and 9.35 min, respectively, and the stretched out shoulder starting at about 9 min most probably correspond to by-products of the synthesis or polymerised CPS during the synthesis or during storage at ambient

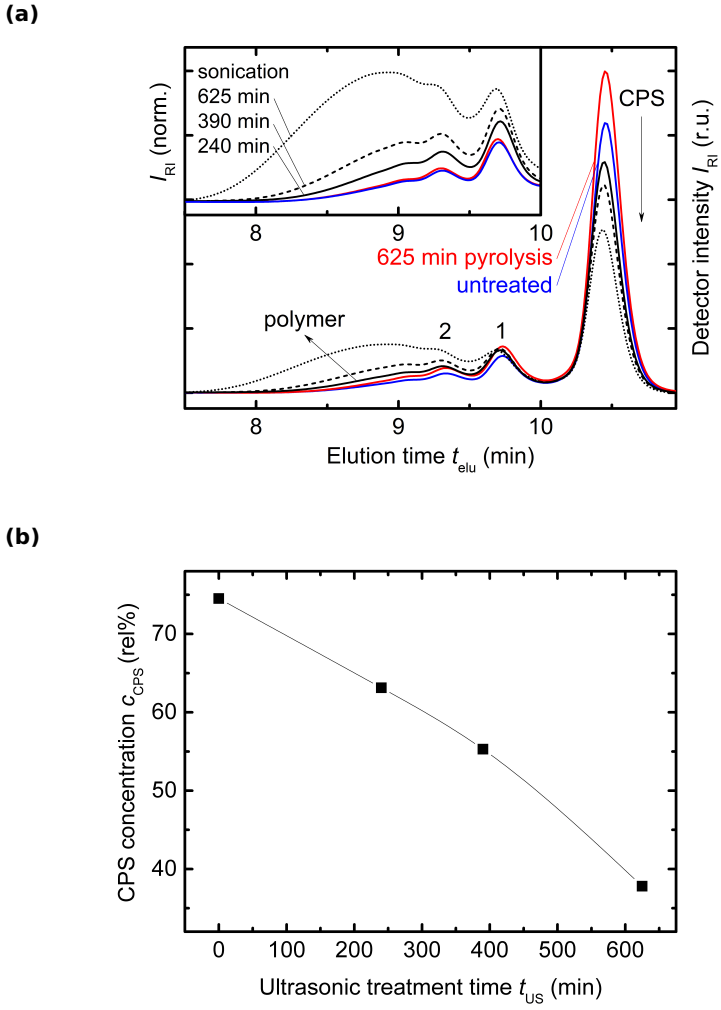

Figure 4.14: *(a) SEC elugrams using cyclooctane as equipment solvent depicting the evolution of larger molecular species in a CPS solution (untreated in blue) with increasing sonication time (black lines) compared to a purely thermally treated (red line) one at the same process temperature of* $\sim 65\,^{\circ}\mathrm{C}$. *The normalised inset demonstrates that the thermally treated and untreated solutions are practically identical. In contrast, with increasing* t_{US} *the sonolytic polymerisation is apparent from the appearance of species at earlier* t_{elu}. ***(b)*** *Plot of the relative concentration of CPS monomer* c_{CPS} *as a function of* t_{US}. *Here,* c_{CPS} *is calculated using the intensities of the CPS monomer peak at* $10.4\,\mathrm{min}$ *and polymer signal between* 7.5–$10\,\mathrm{min}$ *in the elugrams above.*

temperature in the glove box in the stainless steel vessel or glass vials. Peak 1 and 2 could possibly correspond to the CPS dimer (10 Si atoms) and trimer (15 Si atoms), respectively. This proposition, however, has not been verified. The red curve corresponds to the purely thermally treated solution. The intensity of the CPS peak at ca. 10.45 min is visibly slightly higher than the rest of the underlying signal and may be explained by minor preferential evaporative losses of CO solvent (since its boiling point of bp = 151 °C is lower than that of CPS with bp = 194.3 °C) during thermal treatment on the hot plate. This has as a consequence that the sample taken for SEC analysis had a slightly higher concentration of CPS.

In order to ascertain whether any polymer growth took place the untreated (blue) and thermally treated (red) curves are normalised to the main CPS peak, the results of which are shown in the inset of *Figure* 4.14a. Since both signals have essentially the same form it can be concluded that no polymerisation has taken place upon pyrolytic treatment. On the other hand, the black curves show the results of sonication after 240–625 min at the same process temperature of $\sim$ 65 °C. The elugrams thus show a reduction in peak intensity of unreacted CPS at $t_{\mathrm{elu}} = 10.45$ min and the simultaneous emergence of newly formed species at $t_{\mathrm{elu}} < 9.5$ min, which unambiguously demonstrates the growth of a higher hydridosilane via the sonolytically induced ROP of CPS.

CPS has a RI of 1.69 and for some lower silanes e.g. $Si_3H_8 = 1.49$, $Si_4H_{10} = 1.55$, $Si_5H_{12} = 1.57$, $Si_6H_{14} = 1.59$, and $Si_7H_{16} = 1.60$ [50]. Since the RI continues to increase the larger the silicon hydride polymer is, for this rough estimate it is assumed that the signal response of the differential RI detector to the various silanes is of the same order in the limited retention time range from ca. 7–10 min of the elugram. In this way one can compare the area under the CPS (I_{CPS}) and polymer (I_{poly}) signals to get an estimate of how much CPS has been converted to polymer. For this, the relative CPS concentration is defined as $c_{\mathrm{poly}} = I_{\mathrm{CPS}}/(I_{\mathrm{CPS}} + I_{\mathrm{poly}})$ (in %) and the results are shown in *Figure* 4.14b as a plot of c_{CPS} versus t_{US}. As expected from the trends depicted in the elugrams, a general decrease in c_{CPS} as t_{US} increases is observed. Also, the solution is found to still contain $\sim$ 40 rel% of unreacted CPS monomer after about 600 min of ultrasonic treatment. This rather large amount of residual CPS is useful and necessary since CPS itself is a very good solvent for the thereof derived polysilanes.

We should mention that the employment of an active cooling system enables the CPS polymerisation reactions to potentially be carried out at temperatures as low as −13 °C (refer to reference [63] for thin films prepared from inks treated at 20–25 °C). Interestingly, after filtering with a 0.2 µm syringe filter, precursors produced at room-temperature or below take on colours ranging from clear lemon-yellow to light-brown. This additional colouration is believed to point to the production of a non-negligible amount of highly branched silicon sub-hydrides of the generic form -$(SiH_x)_n$-, with $x \leq 2$, or silicon particles as was described earlier for the case where TS is used as monomer [45, 64]. Note that this is distinctly different to the characteristic colourless (for longer treatment times, milky white prior to filtering) appearance reported in the literature for the polydihydrosilane of the form -$(SiH_x)_n$- prepared via the conventional method using UV light [63].

4.2.2 Polymer Growth via Sonication using Cyclopentasilane as Precursor

In order to gain insight into the growth, molecular mass and the distribution of the silicon hydride polymer with increasing ultrasonic treatment time, another CPS/CO solution was analysed by SEC at various stages of sonication. The CPS/CO solution used for this experiment had a volume of ∼ 0.5 mL and a concentration of 9 wt%. The sonication parameters were: $A = 120$ µm, $DC = 40$ % and process temperature $T \sim 65$ °C. As mentioned in *Section* 3.11, the present experiment was carried out using cyclohexene (CH) as SEC equipment solvent since the PS molecular weight references used were found to be soluble in this solvent under these experimental conditions. Here the peak for unreacted CPS monomer is found to occur concurrently with that of CO and thus information on the varying concentration of unreacted CPS was not accessible.

Figure 4.15 shows the results of the experiment. The blue curve corresponds to the untreated CPS/CO solution, and peaks 1 and 2 are identical to those found in *Figure* 4.14a, these being associated with the presence of silane compounds other than CPS. The main peak at about 10.2 min (cropped at the top of the plot) corresponds to both unreacted CPS monomer and CO solvent (green curve).

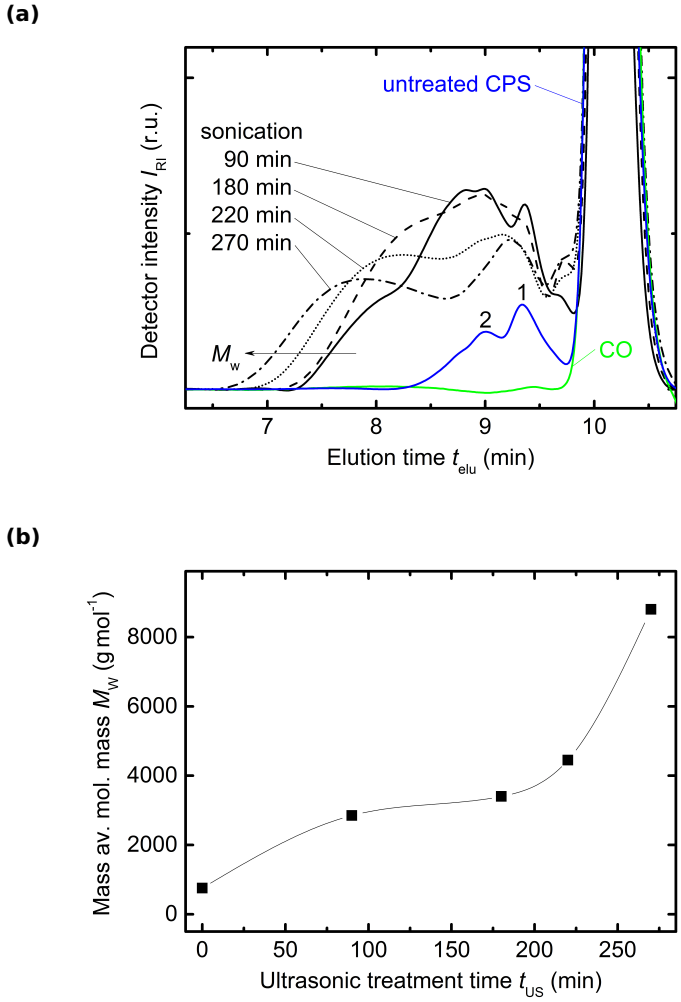

Figure 4.15: *(a) SEC elugrams using cyclohexene as equipment solvent of an untreated CPS/CO solution as well as of solutions having undergone various sonication times. Also shown is the elugram of pure CO, highlighting the fact that it elutes concurrently with the peak for unreacted CPS monomer at* 10.2 min. ***(b)*** *Plot depicting the growth of the mass average molar mass M_w as estimated using polystyrene standards as a function of increasing ultrasonic treatment time t_{US}.*

It is evident that centre of gravity of the polymer distributions shift to earlier t_{elu} with increasing sonication time. The calculated mass average molar mass, M_{w}, associated with the various elugrams is plotted in *Figure* 4.15b as a function of increasing ultrasonic treatment time t_{US}. The colour of the solution was observed to vary from transparent at the beginning, to a very light clear vanilla, through to cloudy white for the 270 min sample. Thus, the M_{w} of the samples with $M_{\mathrm{w}} \geq 220\,\mathrm{min}$ is expected to be somewhat larger than those actually measured. This is because the turbidity indicates precipitation out of solution of the large M_{w} species which are not measurable using SEC.

It should be noted that the occurrence of peaks 1 and 2 does not render the untreated CPS/CO solution suitable for the preparation of thin films via spin coating. All attempts at casting a thin film using untreated solutions resulted in poor wetting and no discernible layer on glass and/or c-Si wafer substrates before and after pyrolytic conversion on the hot plate.

4.2.3 Summary of Polysilane Ink Synthesis using Cyclopentasilane Precursor

Using ultrasound and the sonochemical effects associated with acoustic cavitation, an alternative method of polymerising cyclopentasilane was demonstrated which does not involve the use of ultraviolet light. It is shown by way of size exclusion chromatography and optical transmission measurements that the polymerisation is not initiated by the macroscopically determined temperature of the solution. Rather, the growth of higher hydridosilanes is attributed to the production of reactive species at hot spots generated by collapsing microbubbles. In particular, it is shown that purely pyrolytic treatment of solutions at temperatures of 75 °C or below does not produce the polymer growth observed in similar solutions sonicated at these low temperatures. Further, the results of the sonolysis are presumed to constitute the first time that any such polymerisation of a liquid silane monomer with ultrasound has been reported.

We also find that the amount of unreacted CPS can be varied over a wide range and for an adequately processed precursor usually makes up $< 30\,\%$ of the total silane content after ultrasonic treatment. In addition, the molecular mass of the silicon hydride polymer in the ink is estimated to be in excess of $8 \times 10^3\,\mathrm{g\,mol^{-1}}$.

4.3 Synthesis of Silicon Nanoparticles from Trisilane

As opposed to the previous section focusing on the preparation of a printable ink, this section deals exclusively with details on the sonolytic synthesis of the silicon nanoparticles. Various spectroscopic techniques and electron microscopy images are applied to demonstrate that variation of the concentration of trisilane in the solution or of the amplitude of the ultrasonic waves lead to the fusion of discrete, unoxidised, hydrogenated, and amorphous Si-NPs of tunable size in the range of 1.5–50 nm. Also shown is that under certain conditions, sustained ultrasonic irradiation yields highly porous, sponge or coral-like silicon nanoparticle agglomerates.

4.3.1 Formation Mechanism

As described in the previous section as well as in *Section* 2.4, the extreme transient conditions generated at imploding microbubbles lead to the synthesis of silicon radicals ($Si^{\bullet}$) that subsequently diffuse into the bulk of the liquid and via various insertion reactions involving silylenes/silenes in conjunction with hydrogen shift reactions go on to form higher order silanes and, in turn, silicon hydride polymers. In addition to this, it was hypothesised that a single collapse event also results in the "fusion" of an single Si-NP (refer to *Section* 2.4 and *Figure* 2.5). One of the main experimental conditions made use of during sonication and subsequent bubble formation is that TS is highly volatile ($P_{vap} \approx 95$ Torr at 0 °C compared to ≈ 4 Torr for CO solvent) so that relative to CO, preferentially more TS diffuses into the microbubbles during rarefaction cycles. This results in an accumulation of gaseous TS within the cavity during bubble growth.

The formation of isolated particles is ascribed to the interplay between the extreme conditions that reign during cavitational collapse and to the high density of reactive species generated at such temporally discrete and spatially localised

points in the liquid. A potential explanation for the amorphous morphology of the Si-NPs is the presence of residual bonded hydrogen in the particles left behind as a result of incomplete out-diffusion during bubble collapse, which inhibits Si-Si bond formation. Moreover, the fast cooling rates during cavitational collapse as well as the short-lived nature of the hot spot itself give the silicon matrix too brief an interaction time to reconstruct and relax into a crystalline state.

The direct "fusion" mechanism for particle synthesis is found to be more plausible than ones involving the generation of $Si^{\bullet}$ in conjunction with subsequent nucleation. This is supported by the results of the previous section, which were made under otherwise similar conditions. Briefly, experiments showed that irradiation of TS with UV light results in chromatographically detectable quantities of higher order silanes only after long treatment times of several hours. Like TS, however, these higher order silanes are themselves transparent and so cannot explain the observed colouration of the solutions. Extended UV irradiation for $> 50\,\mathrm{hr}$ eventually results in observable quantities of polymeric silicon sub-hydrides. These branched polymers give the solution the lemon-yellow colouration described in connection with the TS ink [45, 64], but the mixture remains clear with no indication of the presence of dense particulate matter. Hence, if radicals or oligomers were the precursor seeds from which the Si-NPs grow during sonication, one would expect similar particle formation from such photo-generated species and this is certainly not observed.

That the synthesis of the Si-NPs is pyrolytically initiated due to the macroscopic temperature of the solution during treatment (roughly -15–$40\,^{\circ}\mathrm{C}$) can also be ruled out. Solutions submitted to purely thermal treatment at even higher temperatures of up to $65\,^{\circ}\mathrm{C}$ for several hours remain completely transparent and simply incur evaporation losses. This is not surprising since these process temperatures are over $200\,^{\circ}\mathrm{C}$ lower than those required for the thermal decomposition of TS [34, 35]. It is thus conjectured that particle fusion is a primary process taking place during a single bubble collapse event and that reactive species or oligomers undergoing subsequent nucleation cannot account for the particle formation.

4.3.2 Analysis of the Silicon Nanoparticles via Electron Microscopy Techniques

Transmission electron microscopy (TEM) is used to investigate the size of the Si-NPs prepared via sonication at scales inaccessible using SEM, as well as to ascertain whether the particles are amorphous or crystalline. In conjunction with the TEM analysis, electron energy loss spectroscopy (EELS) is used to determine the chemical composition of various nanoparticles with diameters in the range 1.5–50 nm.

Depending on the desired kind of particles, two main preparation parameters can be easily varied, namely (i) the amplitude of vibration of the ultrasonic horn (A) and (ii) the concentration of trisilane in the solution (c_{TS}). As long as the amplitude is sufficiently high to reach the cavitation threshold, in general it is found that low tip A or low c_{TS} favour the production of isolated and monodisperse Si-NPs. *Figure* 4.16a shows Si-NPs synthesised with low A (= 48 µm) and high c_{TS} (= 47 wt%). The higher magnification inset on the top right of the dashed region highlights the discrete nature of the particles. Analysis of the 387 particles visible in the main image (using *ImageJ*) yields the histogram shown in *Figure* 4.16b. The particles possess a mean diameter $D_{\mathrm{m}} = 2.96 \pm 0.82$ nm, constituting a size distribution comparable to published results for similarly sized particles [96, 144], albeit without any filtering or sampling since the collection of the particles was done by simply submerging the C grid into the suspension.

On the other hand, high A (= 192 µm) and high c_{TS} favour the production of large amounts of larger and more polydisperse particles (*Figure* 4.16c). This is attributed to larger microbubbles due to the higher A and/or more TS in-diffusion during bubble growth due to sufficiently high c_{TS} in the surrounding liquid [85, 90]. Clearly visible in the image and in the higher resolution inset is the production of predominantly larger and more polydisperse particles in the range of $\sim$ 10–50 nm which coalesce to form irregularly shaped $\sim$ 100 nm sized clusters. The particles are thus significantly different from those presented in *Figure* 4.16a, which were prepared under otherwise identical conditions except with reduced maximum amplitude at the tip A of 48 µm.

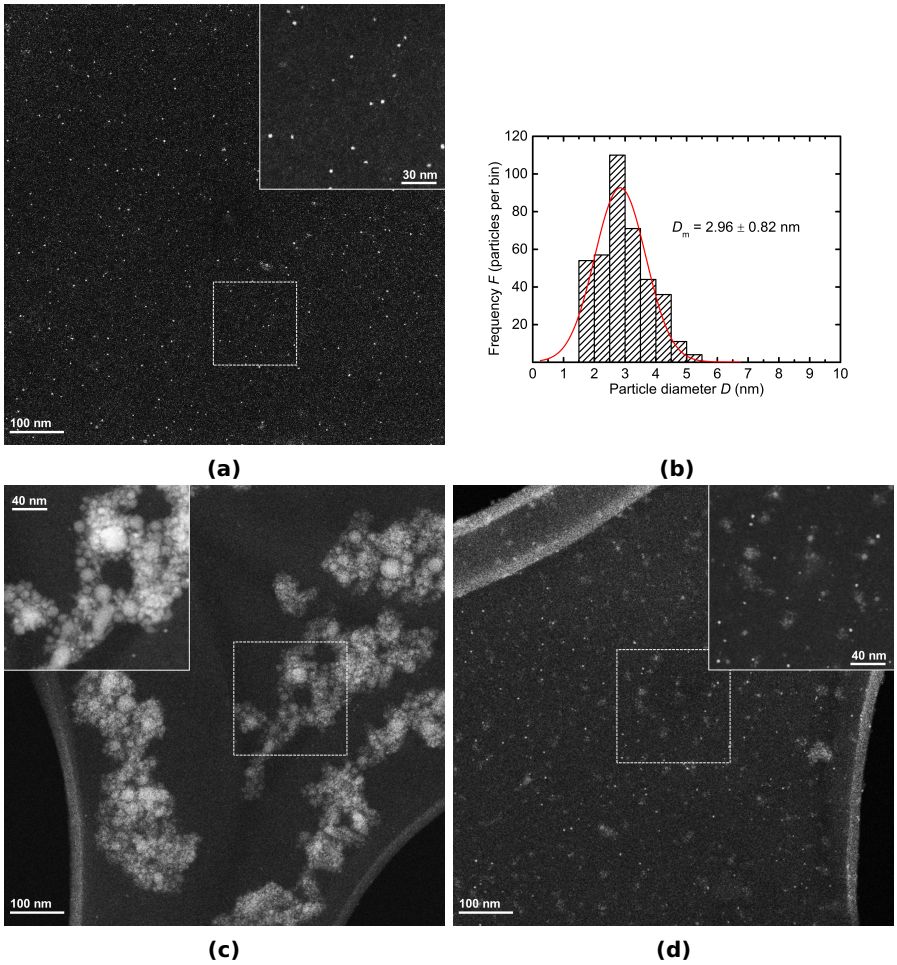

Figure 4.16: *Dark field STEM images depicting the effects of sonication conditions on the predominant type of Si-NPs that are synthesised.* ***(a)*** *Si-NPs produced using low ultrasonic intensity (low tip amplitude $A = 48\,\mu m$) and high trisilane concentration ($c_{TS} = 47\,wt\%$).* ***(b)*** *Histogram of the 387 particles in (a), the red curve is a Gaussian fit to the data.* ***(c)*** *Si-NPs produced using high tip amplitude ($A = 192\,\mu m$) and $c_{TS} = 47\,wt\%$.* ***(d)*** *Si-NPs produced using high tip amplitude ($A = 192\,\mu m$) and a low c_{TS} of $1\,wt\%$. The insets show higher resolution images of the regions enclosed by dashed boxes.*

Alternatively, keeping A high, but lowering c_{TS} to 1 wt%, (*Figure* 4.16d demonstrates the synthesis of smaller and more monodisperse Si-NPs similar to those depicted in *Figure* 4.16a. The clear suppression of the synthesis of larger particles and the simultaneous production of significantly smaller and more monodisperse particles of size in the range 2.5–4.6 nm is in stark contrast to the particles produced using excess TS but with equally high A. The type of particles produced is attributed to reduced diffusion of TS into the expanding microbubbles resulting in less silicon precursor material available for particle fusion upon cavitational collapse. The "cloudy" patches of slightly lower intensity visible in the main imagehiand in the higher resolution inset are small clusters of comparably small particles of somewhat lower density.

To demonstrate that particle fusion commences essentially immediately after activation of the ultrasonic horn, Si-NPs were synthesised in a solution that was subjected to sonication (high A (= 192 µm) and high c_{TS}) for a mere 2 min at a process temperature of 25–40 °C. Here, the solution took on a clear, light vanilla colouration after sonication. Note that the sonication conditions (A and c_{TS}) are identical to those used for the particles depicted in *Figure* 4.16c.

The bright-field TEM image in *Figure* 4.17b reveals that the solution already contains significant amounts of Si-NPs ranging in size from around 5–50 nm (*Figure* 4.17b). Most particles, however, are found to be < 40 nm in size. *Figure* 4.17a shows a TEM image of a larger Si-NP of ~ 50 nm. The particle exhibits a fluffy, cauliflower-like morphology that suggests it may be composed of even smaller constituents of < 10 nm, either chemically bonded or loosely bound forming an agglomerate. The inset on the top left shows an electron diffraction pattern exhibiting a set of diffuse rings which demonstrate the amorphous nature of the particles. The inset on the top right shows a core-level electron energy loss spectroscopy (EELS) spectrum revealing a strong Si-$L_{2,3}$ edge at ~ 100 eV. The form and onset energy of the edge indicates that the particles are composed of unoxidised silicon and not, for instance, of a silicon oxide. Also discernible is a small hump at ~ 280 eV corresponding to the carbon K-edge and which is attributed to the adjacent C grid. Note that no trace of the oxygen K-edge at ~ 530 eV is discernible to within the limits of sensitivity. Chemical analysis via EELS thus shows that the Si-NPs contain neither oxygen in the bulk nor an encapsulating outer oxide shell.

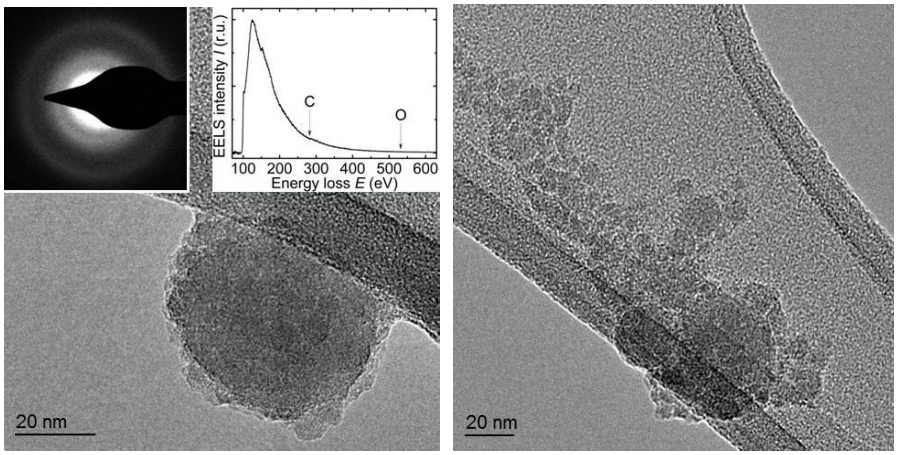

Figure 4.17: *TEM images of Si-NPs synthesised in-solution within* 2 min *of sonication.* ***(a)*** *The particle in the image appears fluffy as if composed of even smaller particles and its cauliflower-like morphology is devoid of any sharp contours or boundaries. The electron diffraction pattern in the inset on the top left shows a set of diffuse rings indicating that the particles are amorphous. The inset on the top right shows the core-level EELS $SiL_{2,3}$-edge at* $\sim$ 100 eV *indicating that the particles are composed of unoxidised silicon. The slight elevation at* $\sim$ 280 eV *is the carbon K-edge and no trace of the oxygen K-edge is evident at* $\sim$ 530 eV. ***(b)*** *The image shows a cluster of separate particles, the smallest of which have diameters in the range of* $\sim$ 5 nm.

4.3.3 Analysis of the Silicon Nanoparticles via Infrared Spectroscopy

In the following, Fourier transform infrared spectroscopy (FTIR) is used to characterise the elemental composition and morphology of drop-coated Si-NPs films, as well as to demonstrate that the particles are hydrogenated and to elucidate the nature of the silicon-hydrogen bonding. Also dealt with is the behaviour of the particles upon exposure to ambient air. Note that the particles used for the analysis were synthesised using high tip amplitude and high TS concentration (refer to *Section* 4.3.2 above for details).

Shown in *Figure* 4.18 is a series of FTIR spectra of Si-NPs measured as-deposited (40 °C) and after subsequent annealing at temperatures from 200–500 °C. The first

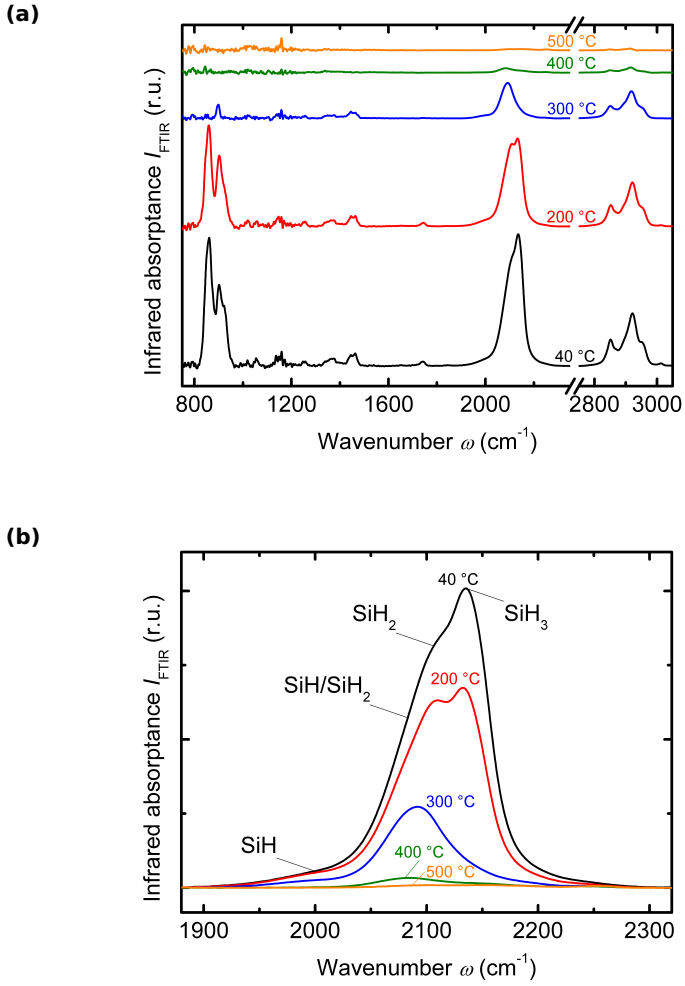

Figure 4.18: *(a) FTIR spectra of Si-NPs deposited via drop coating at* 40 °C *and after subsequent annealing at temperatures up to* 500 °C*. The various Si-H and C-H modes are discussed in the main text.* ***(b)*** *Magnified plot of the SiH_x stretching modes centred at* $\sim$ 2100 cm^{-1} *showing their decreasing intensity as more and more hydrogen and silicon hydrides evolve from the particles with increasing temperature. The surface hydrides at* $\sim$ 2100–2140 cm^{-1} *evolve first and then the bulk hydrides at* $\sim$ 2000–2080 cm^{-1} *follow.*

three spectra (40, 200, and 300 °C) in *Figure* 4.18a are dominated by two main silicon hydride bands, one at 840–910 cm^{-1} comprising a characteristic doublet related to various SiH_2 and SiH_3 deformation, bending, wagging and scissor modes and another at 2000–2140 cm^{-1} associated with SiH_x (x = 1, 2 or 3) stretching modes of hydride groups in the bulk, at the outer surface, and at the internal surfaces of microvoids within the particles themselves. The latter spectral region is reproduced in *Figure* 4.18b to make the modes more apparent.

Increasing the annealing temperature enables the identification of four main bands corresponding to distinct silicon-hydrogen bonding configurations in regions of the material associated with specific stoichiometry and microstructure. Evident from the as-deposited (black, 40 °C) and the 200 °C (red) spectra, are two dominant peaks at $\sim$ 2110 and $\sim$ 2135 cm^{-1} corresponding to dihydride (SiH_2) and trihydride (SiH_3) groups at the exterior surface of the Si-NPs, respectively [97, 145]. After annealing at 300 °C (blue line) a third band emerges at $\sim$ 2090 cm^{-1} as a result of most SiH_2 and SiH_3 hydride groups having evolved from the exterior surface of the particles. This peak is associated with monohydride (SiH) and dihydride groups at the internal surfaces of microvoids in the bulk of the particles and at the exterior surface. The evolution of the surface hydrides at this temperature is also corroborated by observing that only a small SiH_2 (bending or scissor mode) peak at $\sim$ 898 cm^{-1} remains in *Figure* 4.18a. Finally, a broad shoulder is evident at $\sim$ 2000 cm^{-1} which corresponds exclusively to SiH groups where the hydrogen atom resides at silicon monovacancy/divacancy sites in dense bulk material [76]. This mode is more apparent in *Figures* 4.19a and 4.19c and corresponds to hydrogen in the inner core of the Si-NPs. At 400 °C (green line) the peak at $\sim$ 2090 cm^{-1} shifts slightly towards $\sim$ 2080 cm^{-1} consistent with a shift of the bulk hydrides component as a result of a more compact microstructure [146]. At 500 °C (orange line), most of the hydrogen in the bulk of the particles has also out-diffused.

Finally, the bands between 1100–1760 cm^{-1} and 2800–3050 cm^{-1} are associated with various CH_x-modes from residual solvent and attenuate as a result of evaporation as the temperature is raised after successive annealing steps [96, 97]. This means that the detected carbon is present as an evaporable adsorbate only, which in turn shows that the solvent acts as an inert reaction medium that does not take

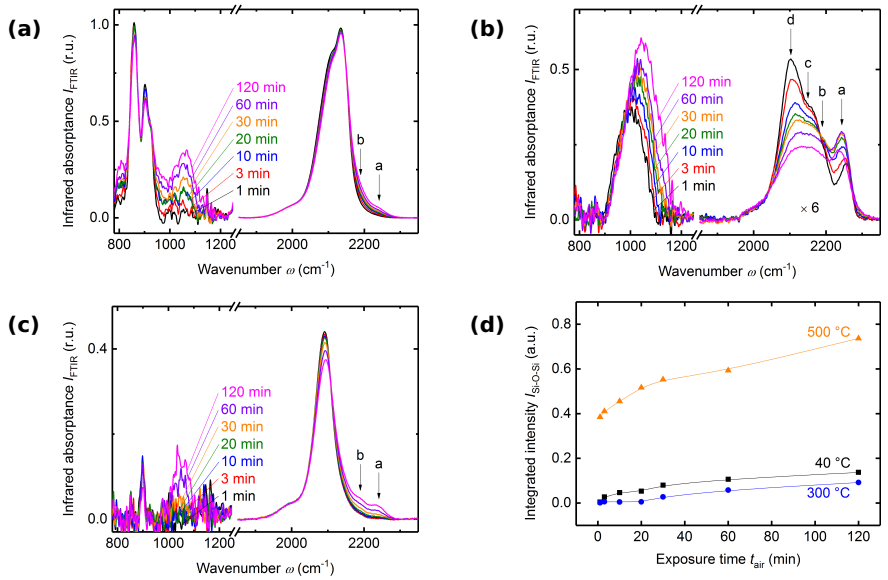

Figure 4.19: *FTIR study depicting the effect of air exposure on Si-NPs annealed for* 10 min *at different temperatures.* ***(a)*** *40 °C: As the air exposure time t_{air} increases the particles oxidise as evident from the increasing intensity of the Si-O-Si stretching mode at* $\sim$ 1000–1150 cm^{-1} *and the SiH_x modes with back-bonded oxygen labelled* ***a*** *and* ***b****.* ***(b)*** *500 °C: As evident from the Si-O-Si mode as well as the SiH_x modes with back-bonded oxygen labelled* ***a*** *-* ***d****, the particles easily oxidise if most of the hydrogen is removed. Note that the spectra after the break have been magnified* $\times 6$ *to facilitate visibility.* ***(c)*** *300 °C: The almost complete absence of SiH_2/SiH_3 surface hydrides and hence the predominantly SiH terminated surface of the particles mitigates oxidation for the first* 20 min*. Note that the ordinate scale of all plots is identical.* ***(d)*** *Integrated intensity of the Si-O-Si stretching mode versus t_{air} at the different temperatures. The strongest oxidation is measured for Si-NPs with low hydrogen content and particles with high concentrations of SiH_2 and SiH_3 surface hydride groups. Si-NPs with predominantly SiH/SiH_2 terminated surfaces exhibit the slowest and least oxidation.*

part chemically during Si-NP fusion. The bulk chemical composition of the Si-NPs hence comprises Si and a tunable amount of H.

The following deals with the oxidation behaviour of the particles as a function of annealing temperature (in N_2 atmosphere, H_2O, $O_2 \sim 1$ ppm) and duration of exposure to ambient air (24 °C, 57 % humidity). Here, the measurements were

carried out in vacuum after each air exposure step (1, 3, 10, 20, 30, 60, and 120 min).

Shown in the series of plots in *Figure* 4.19, is how the hydrogenated nature of the bulk and the H_x-termination of the surface of the particles help mitigate rapid oxidation upon exposure to air. Particles deposited at 40 °C (*Figure* 4.19a), capped primarily with loosely bound SiH_2/SiH_3 surface hydride groups, are found to oxidise at low to moderate rates. After 3 min in air the characteristic Si-O-Si stretching mode appears at $\sim 1050\,cm^{-1}$, as well as modes associated with SiH_x groups back-bonded to oxygen [97, 147, 148]. In the plot, stretching mode **a** at $\sim 2245\,cm^{-1}$ is assigned to H-(SiO_3) and mode **b** at $\sim 2190\,cm^{-1}$ is assigned to H-(Si_2O_2). The SiH mode at $\sim 2000\,cm^{-1}$ remains stable and the SiH_2/SiH_3 bands at 840–910 cm^{-1} and 2110–2140 cm^{-1} decrease slightly as the oxidation progresses. The noticeable oxidation of these particles is due to the fact that the SiH_2/SiH_3 groups covering their outer surface readily react with oxygen or atmospheric water vapour.

Radically different is the behaviour of particles with very little hydrogen content. *Figure* 4.19b clearly demonstrates that once most of the H has been driven off via annealing at 500 °C for 10 min, the particles become exceedingly susceptible to oxidation. Note that the ordinate scale of this plot corresponds to that of *Figure* 4.19a and that the spectra after the break have been magnified ×6 to facilitate visibility. Here, a broad Si-O-Si stretching mode at $\sim$ 950–1150 cm^{-1} is already clearly visible after just 1 min in air. Also, the stretching modes centred at $\sim 2100\,cm^{-1}$ are exclusively associated with SiH_x groups back-bonded with oxygen. Modes **a** and **b** are as in *Figure* 4.19a, and mode **c** at $\sim 2150\,cm^{-1}$ is assigned to H_2-(SiO_2) and mode **d** at $\sim 2100\,cm^{-1}$ is assigned to H-(Si_3O). In general, as the oxidation advances the growth of the Si-O-Si mode is accompanied by a gradual redistribution of the stretching modes from the singly oxygen back-bonded **d** to progressively higher oxidation states **c** → **b** → **a**. Here, a broad Si-O-Si stretching band at $\sim$ 1000–1150 cm^{-1} and oxygen back-bonded SiH_x stretching modes at $\sim$ 2100–2250 cm^{-1} are readily observed directly after annealing in the glove box [149].

Evidently, both excess hydrogen in the form of reactive SiH_2 and SiH_3 groups as well as hydrogen deficiency at the outer surface of the Si-NPs lead to significant

oxidation upon exposure to air. To demonstrate a substantially slower oxidation rate, a third thin film of Si-NPs is annealed at 300 °C for 10 min and then exposed to air as before. *Figure* 4.19c shows that most of the surface polyhydrides have evolved from the particles as evident from the absence of SiH_2 ($\sim 2110\,cm^{-1}$) and SiH_3 ($\sim 2135\,cm^{-1}$) stretching modes, and the clear predominance of the SiH bulk ($\sim 2000\,cm^{-1}$) and SiH_2/SiH_3 ($\sim 2090\,cm^{-1}$) bulk and surface hydride modes. Note that a small amount of residual surface SiH_2 is still present as indicated by the peak at $\sim 900\,cm^{-1}$ (bending or scissor mode, compare with the corresponding spectrum in *Figure* 4.18a). The oxidation progresses slower than in *Figures* 4.19a and 4.19c, where only after 20 min does any growth in the Si-O-Si, and modes **a** and **b** become significant. Notice also that while the peaks at $\sim 900\,cm^{-1}$ and $\sim 2090\,cm^{-1}$ decrease in intensity, the presence of a constant fraction of the SiH mode at $\sim 2000\,cm^{-1}$ (as is also the case in *Figures* 4.19a and 4.19c) indicates that the dense core of the Si-NPs remains hydrogenated and oxygen-free. Particles with mainly monohydride (SiH) or dihydride (SiH_2) terminated surfaces are hence found to be highly resistant against oxidation and remain essentially oxide-free for air exposures up to about 20 min.

In *Figure* 4.19d the integrated intensity of the Si-O-Si stretching mode is plotted as a function of air exposure time t_{air} for the Si-NP thin films of the oxidation series. The curves demonstrate that the hydrogenated nature of the particles (40 and 300 °C) leads to a mitigation of oxidation compared to particles where the hydrogen has been almost completely removed via annealing at high temperature (500 °C).

4.3.4 Raman Spectroscopy

In conjunction with the electron diffraction pattern shown in *Figure* 4.17a, Raman spectroscopy was used to confirm the amorphous morphology of the Si-NPs and show the effect of annealing on the microstructure. Shown in *Figure* 4.17a are Raman scattering spectra of as-deposited Si-NPs (black, 40 °C) and as they are progressively annealed in the glove box at 200 °C (red), 300 °C (blue), 400 °C (green) and 500 °C (orange) for 3 min at each temperature. Four characteristic

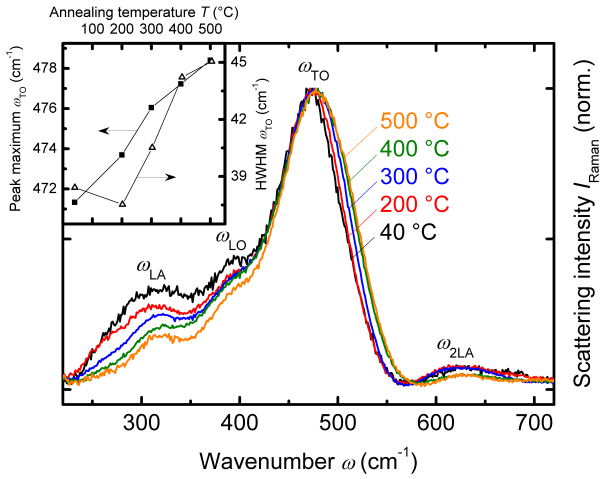

Figure 4.20: *Raman scattering spectra of a thin film of Si-NPs as a function of annealing temperature. The main plot shows the longitudinal acoustical (ω_{LA}), longitudinal optical (ω_{LO}) and transverse optical (ω_{TO}) and the second order longitudinal acoustical (ω_{2LA}) phonons. The inset shows the evolution of the position of the ω_{TO} peak maximum (solid squares) and its half-width at half-maximum (HWHM, hollow triangles) as a function of annealing temperature.*

phonon bands associated with hydrogenated a-Si are identified. These are the longitudinal acoustical (ω_{LA}), longitudinal optical (ω_{LO}) and transverse optical (ω_{TO}) and the second order longitudinal acoustical (ω_{2LA}) phonon mode at around 310, 390, 470 and 620 cm^{-1}, respectively [75, 120].

As the annealing temperature is raised a relative decrease in the intensity of the ω_{LA} and ω_{2LA} modes relative to the ω_{TO} phonon is seen, consistent with a reduction in hydrogen content [75, 122]. Peak analysis (not shown) reveals that the ω_{LO} phonon intensity varies slightly from curve to curve with no consistent trend and hence changes in the medium range order of the Si-NPs could not be ascertained. Shown in the inset are the shift of the peak maximum from 471.3 to 478.4 cm^{-1} and the asymmetric broadening of the ω_{TO} mode (HWHM measured using the peak maximum and right flank) from 38.4 to 45.1 cm^{-1}. The shift can be related to a modified atomic bonding environment and/or mechanical stress, and the broadening is in accordance with decreasing short range structural order, e.g.

due to a distribution of strain and bond angles of the Si-Si bonds as a result of matrix reconstruction after hydrogen evolution. Raman spectroscopy hence reveals that the Si-NPs do not crystallise and remain in the amorphous state even at the moderately high temperatures reached during the final annealing steps.

4.3.5 X-Ray Photoelectron Spectroscopy

Surface sensitive x-ray photoelectron spectroscopy (XPS) was carried out on thin films of Si-NPs in order to corroborate the conclusions drawn from the elemental analysis via high spatial resolution EELS on a single $\sim 50\,\text{nm}$ Si-NP presented in *Figure* 4.17a.

Shown in *Figure* 4.21a is a high resolution narrow scan of the Si 2p core-level peak centred at a binding energy (E_B) of $\sim 99.5\,\text{eV}$. The data points are depicted as solid black dots and the least-squares fit resulting from the deconvoluted components is drawn in solid black. The main deconvoluted peak (red) corresponds to elemental Si and is a doublet consisting of two components fitted with equal FWHM (0.752 eV), an intensity ratio of 1:2 and separated by a spin-orbit splitting of 0.61 eV. They are labelled $\text{Si}^0\ 2\,\text{p}_{1/2}$ and $\text{Si}^0\ 2\,\text{p}_{3/2}$ and are located at 99.84 and 99.23 eV, respectively.

Following the method described by Ley et al. [150] and with the foreknowledge that the bulk and surface of the Si-NPs are hydrogenated, three additional doublets are fitted which correspond to the chemically shifted Si 2p peak when the Si atom is bonded to either 1 (Si^{1+}, blue doublet), 2 (Si^{2+}, green doublet) or 3 (Si^{3+}, orange doublet) H atoms. The SiH_x doublets are spaced 0.4 eV apart [151] and are fixed to the same FWHM, intensity ratio and spin-orbit splitting as the Si^0 doublet. The slight mismatch at $\sim 101.5\,\text{eV}$ is attributed to the presence of atmospheric water vapour on the surface of the Si-NP film accrued during sample transfer. Water vapour has been documented to give rise to a chemically shifted component due to adsorbed OH groups [152, 153]. Note the absence of a SiO_2 peak at $\sim 103.6\,\text{eV}$ and that no sub-oxides are discernible up to $\sim 2\,\text{eV}$ below that [98, 154–157].

Shown in *Figure* 4.21b is a survey scan revealing the surface composition of the Si-NP film. Evident is the presence of silicon (Si 2s and Si 2p at a E_B of $\sim$ 150 eV

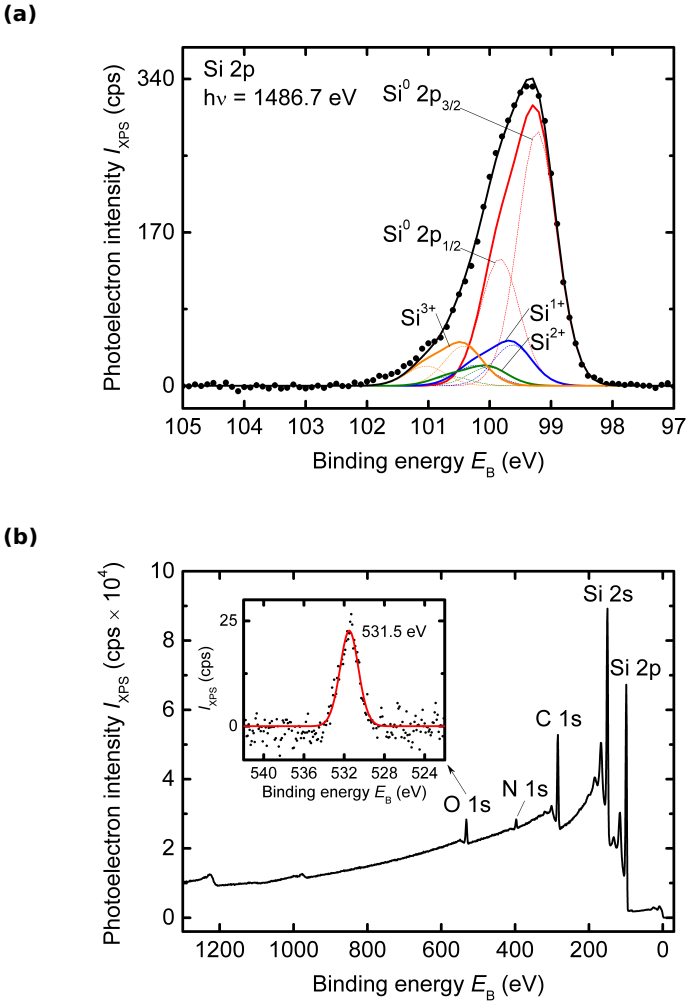

Figure 4.21: *(a) High resolution XPS core-level spectrum of the Si 2p peak fitted with four doublets corresponding to Si atoms bonded to 0, 1, 2 or 3 H atoms (Si^0, Si^{1+}, Si^{2+} and Si^{3+}, respectively). Note the absence of a SiO_2 peak expected at $\sim$ 103.6 eV for oxidised particles.* ***(b)*** *XPS survey spectrum of drop-coated Si-NPs. The presence of three main elements, namely Si, C, and O is detected. An increasingly small amount of N of < 0.5 at% is also discernible at $\sim$ 397 eV. The inset shows a high resolution narrow scan of the O 1s peak at 531.5 eV.*

and $\sim$ 99 eV, respectively), carbon (C 1s, at $\sim$ 284.5 eV) and oxygen (O 1s, at $\sim$ 531 eV). Included in the plot as an inset is a high resolution narrow scan of the O 1s peak which provides a more precise determination of its binding energy of 531.5 eV. This relatively low E_B suggests that the O is likely present in non-bridging form such as in H_2O molecules or OH groups and not incorporated as a SiO_x, where the latter has typical E_B values that range between 532 eV and 533 eV [158–160]. The calculated atomic concentrations are 76.3, 21.8 and 1.93 at% for Si, C and O, respectively. The high value for C is not surprising since the particles were not annealed to remove residual CO solvent. The very low value for the O concentration is comparable to that found on freshly etched (with hydrofluoric acid) amorphous and crystalline Si surfaces with sub-monolayer O coverage [159, 160]. For comparison, a typical survey scan of Si/SiO_x core-shell particles with a $\sim$ 1 nm thick oxide can be found in the work by Li et al. [109].

4.3.6 Summary of Silicon Nanoparticle Synthesis

In contrast to the use of both ultrasound and ultraviolet light in the fabrication the silicon polymer - silicon nanoparticle composite ink, here details on the purely sonochemical synthesis of discrete, unoxidised hydrogenated amorphous silicon nanoparticles in the size range 1.5–50 nm was presented. It was argued that the synthesis could be best understood as a type of "fusion" process due hot spots generated at imploding microbubbles. The method was shown to be possible at ambient pressure and at temperatures in the range 10–40 °C, and entailed sonication using different tip amplitudes of vibration and solutions of variable trisilane concentration.

The macroscopic colloids or agglomerates responsible for the brown colouration of sonicated solutions presented in *Section* 4.1.2 were studied further. Using TEM and STEM it was shown that high tip amplitudes lead to the production polydisperse silicon nanoparticles in the size range $\sim$ 10–50 nm and that these subsequently agglomerate to form the high surface area sponge or coral-like agglomerates discussed previously. In stark contrast, low tip amplitudes or low trisilane concentrations were shown to yield smaller particles in the range $\sim$ 1.5–5 nm.

In particular, without the aid of any filtering or special sampling technique, low tip amplitudes enabled the synthesis of particles of good monodispersity with an average size of $2.96 \pm 0.82\,\mathrm{nm}$.

Several spectroscopic techniques were used to investigate the chemical and physical properties of the nanoparticle thin films. Electron diffraction and Raman scattering were used to show that the particles are amorphous and remain so up to annealing temperatures as high as $500\,^{\circ}\mathrm{C}$. Detailed analysis via electron energy loss spectroscopy, x-ray photoelectron spectroscopy, and Fourier transform infrared spectroscopy were used to study the chemical composition and microstructure of the particles. The results revealed that the particles are composed almost exclusively of hydrogen and silicon. Only traces of oxygen were detected and found to most probably be present on the surface of the particles in non-bridging form. Also, carbon was found to occur only as an evaporable adsorbate and not chemically bonded to silicon. This, in turn, demonstrated that the solvent does not participate chemically during particle fusion. Annealing and oxidation experiments showed that the hydrogen content of the particles in tunable. In addition, the hydrogen/polyhydride termination of the particles' surface was found to greatly mitigate their oxidation upon exposure to ambient air.

4.4 Thin Films Deposition, Growth, and Conversion

4.4.1 Spin-Coated Silicon Hydride Polymer Films

Polysilane inks prepared as described in *Sections* 4.1 and 4.2 can be used to cast thin films of silicon hydride polymer onto various substrates such as glass and polished c-Si substrates. Spin coating can be applied since the inks contain low-volatility hydridosilanes and exhibit very good wetting of the substrate surface. As will be shown later, the wetting aspect only plays a role here where films are directly cast in a coating process and not when film growth takes place via the APCVD technique.

The thickness of films fabricated from both CPS and TS based inks can be varied by varying the spin coating parameters such moras the spin time and spin speed. One can also deposit thicker films by spin coating several times. Here, before the next film is spin coated, the previously deposited film needs to be dried and tempered at ca. 200 °C to avoid re-dissolving the underlying polymer into the wet, freshly dispensed ink. However, the film thickness also depends strongly on the composition of the ink itself. While CPS-based inks usually require two spin coats to yield layer thicknesses exceeding 100 nm, TS-based ink normally surpass this mark with just a single spin. This is attributed to the much faster drying characteristics of these inks during spin coating due to the faster rate of evaporation of TS compared to CPS. Moreover, TS is usually used in greater weight percentages than CPS (30–50 wt% compared to 8–15 wt%) so that TS-based inks also have a larger proportion of unreacted monomer which significantly decreases the effective boiling point of the solvent.

Although great care is taken to ensure that the substrates are dust-free, spin coated films usually possess a number of macroscopic defects such as comets, striations, pinholes and upon pyrolytic conversion, vortex-shaped micro-cracks (see *Figure* 4.22).

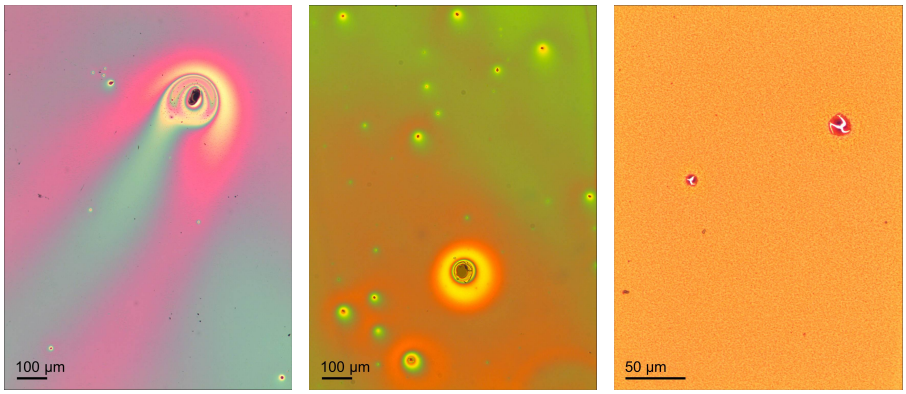

Figure 4.22: *Typical micrographs of defects found in spin coated films.* ***(a)*** *An example of a so-called comet, where an initial inhomogeneity in the film such as a dust particle gives rise to an extended "tail" in the radial direction toward which the fluid is accelerated during coating.* ***(b)*** *Typical pinhole defects, most of which perforate the entire film.* ***(c)*** *Image of a vortex-shaped pinhole or micro-crack that emerges after pyrolytic conversion, presumably at an existing weak spot or pinhole as a result of tensile stress in the film.*

A rough estimate of the effective deposition rate for spin coating with a CPS derived ink can be calculated as follows. A single spin coating of 30 s yields an a-Si:H film of about 50 nm after pyrolytic conversion for 2 min. This translates to an effective deposition rate of $50/150\,\mathrm{s} \approx 33.3\,\mathrm{nm\,s^{-1}} = 20\,\mathrm{nm\,min^{-1}}$. The effective spin coating deposition rate using TS derived inks is roughly double this, i.e. $\sim 40\,\mathrm{nm\,min^{-1}}$.

4.4.2 Formation of Hydrogenated Amorphous Silicon via Pyrolytic Conversion

The as-deposited silicon hydride polymer thin films do not possess the desired properties required for their application as semiconducting layers in optoelectronic devices. The cross-linking of the polymer film or its conversion into a-Si:H is achieved by pyrolysis on a hot plate at temperatures between 250–300 °C. This fact is supported by FTIR measurements where the doublets at 840–860 $\mathrm{cm^{-1}}$ and

Table 4.1: *Summary and assignment of infrared active modes observed in the FTIR spectra of Si-NP agglomerate and a-Si:H thin films.*

Wavenumber (cm^{-1})	Associated group(s)	Vibrational mode
630	SiH, [SiH_2, SiH_3], $(SiH_2)_n$	bending, [rocking], shear
640	[SiH], SiH_2, $(SiH_2)_n$, SiH_3	[wagging], rocking
650	(Si-O-Si)-H	bending
680	SiH	rocking, wagging
840–845	$(SiH_2)_n$	wagging
860–862	SiH_3	sym. deformation
890–910	$(SiH_2)_n$	bending, scissors
950–1110	Si-O-Si	stretching, asym. stretching
2000–2090	SiH	stretching
2080–2110	SiH_2	stretching
2130–2140	SiH_3	stretching
$\sim$ 2100	(Si_3O)-H	stretching, O back-bonded
$\sim$ 2150	(SiO_2)-H_2	stretching, O back-bonded
$\sim$ 2190	(Si_2O_2)-H	stretching, O back-bonded
$\sim$ 2245	(SiO_3)-H	stretching, O back-bonded

890–910 cm^{-1} associated with various polymeric modes are absent at temperatures exceeding 300 °C (refer to *Table* 4.1).

The final morphology or microstructure of the layers varies greatly and depends on several aspects associated with film deposition. The factor exerting the most pronounced influence on the microstructure is the method employed for the deposition, where APCVD films exhibit significantly better microstructure compared to spin coated ones. For the case of spin coated films, additional factors such as conversion temperature, conversion time, and film thickness play major roles. In terms of morphology, the best films fabricated via spin coating are also found to be dependent on the monomer used for the preparation of the polysilane ink, a finding which suggests that the structure and in turn the cross-linking of the polymers fabricated from CPS and TS are dissimilar.

As discussed in *Section* 2.3.1, the microstructure of a-Si:H was characterised by way of the microstructure factor, R, defined as the relative integrated FTIR

intensity ratio of the SiH/SiH_2 stretching mode at $\sim$ 2080–2100 cm^{-1} to the SiH mode at $\sim$ 2000 cm^{-1}. For spin coated samples R ranges from 90 % for microvoid-rich material with a predominantly contribution in the 2080–2100 cm^{-1} region to values as low as 54 % for the best films with exhibiting significant contribution from the 2000 cm^{-1} mode.

We can gain insight into the morphological changes occurring in spin coated films during the conversion process on the hot plate by observing shifts in hydrogen bonding configuration. Apart from the stretching mode at $\sim$ 2000 cm^{-1}, changes in the 850–900 cm^{-1} region can be followed. These bands are associated with various Si-H vibrational modes in $(SiH_2)_n$ and SiH_3 groups, including wagging, bending, scissors and deformation modes (refer to *Table* 4.1). The existence or eventual disappearance of these modes helps facilitate the determination of the temperature at which cross-linking reactions during pyrolytic conversion have resulted in a tetragonal coordinated random network devoid of polymeric $(SiH_2)_n$ chains and SiH_3 terminal groups.

The plots presented in *Figure* 4.23 depict the evolution of several FTIR modes as a function of increasing conversion temperature on the hot plate for films deposited using inks made from CPS (4.23a) and TS (4.23b), respectively. Turning firstly to the above-mentioned modes at around 850 cm^{-1} and 900 cm^{-1}, their gradual decrease between 250–300 °C indicates the densification of the polymer film into a compact three-dimensional amorphous matrix. This appears to occur in a similar manner for both types of ink. These structural changes are also visible in corresponding changes in the Si−H stretching modes between 2000–2140 cm^{-1}, where in general the peaks at higher wavenumbers at 2120–2140 cm^{-1} associated with SiH_3 groups and at 2100–2120 cm^{-1} associated with SiH_2 groups decrease in intensity as more and more hydrogen evolves from the films. This is correlated with a corresponding emergence of new modes between 2050–2080 cm^{-1} associated with dihydride (SiH_2) vibrations in a slightly more compact, albeit microvoid-rich network. It is interesting to note that close inspection of the relative intensities of the peaks at 2110 cm^{-1} (SiH_2 groups) and 2133 cm^{-1} (SiH_3 groups) of the two layers reveals minor differences. It is hence inferred that the unconverted polymer prepared from TS is more branched and has more SiH_3 terminal groups relative

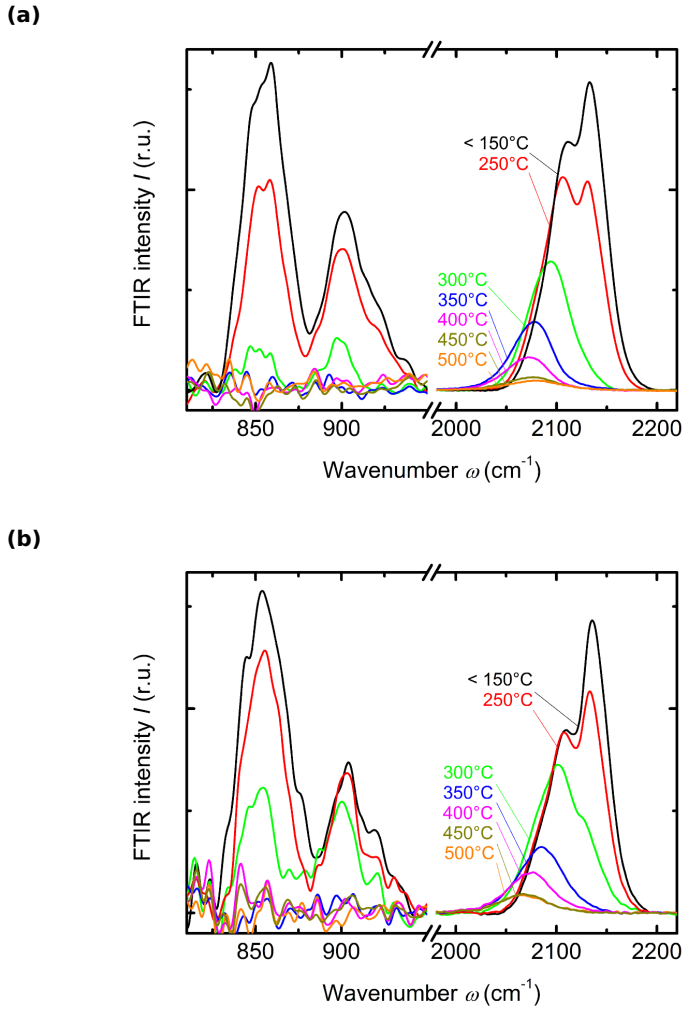

Figure 4.23: *FTIR spectra of hydridosilane thin films prepared from CPS* ***(a)*** *and TS* ***(b)*** *upon pyrolytic conversion at increasingly higher temperatures commencing from drying at* <150 °C *up to* 500 °C.

to SiH_2 groups (along the main chain of the polymer) compared to the polymer prepared from CPS.

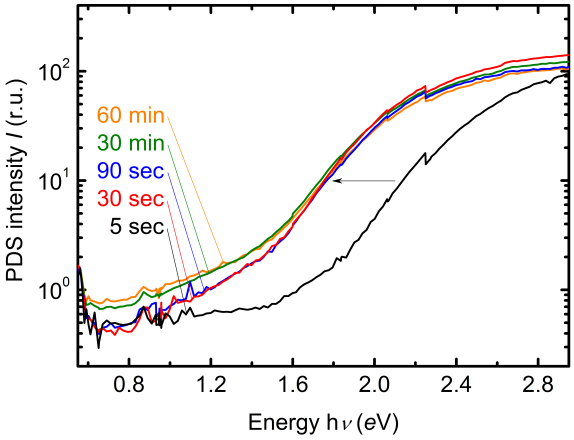

Figure 4.24: *Raw PDS spectra of changes in relative absorbance of a thermally treated silicon hydride polymer film upon increasing conversion time (t_{conv}) on a hot plate at* 450 °C. *As explained in the main text, t_{conv} = 5 sec is insufficient to allow for complete transformation of the polymer to a-Si:H. As seen from the decrease of the optical band gap from* 2.2 *to* 1.8 eV, *the main structural changes occur within the first* 30 s *and increasing t_{conv} to* 90 min *only results in a slight increase in the sub band gap absorption (<* 1.4 1.4 eV*) associated with silicon dangling bonds.*

The question arose as to the minimum time required for pyrolytic conversion to result in the complete transformation of the spun polymer into amorphous silicon. To this end, a film was spin coated onto a glass substrate using an ink prepared from TS and cumulatively increased the conversion time (t_{conv}) from 5 s to 60 min on the hot plate preheated to 450 °C. After each thermal step the sample was measured without air break via photothermal deflection spectroscopy (PDS).

As depicted in the raw PDS spectra of *Figure* 4.24, the first 5 s on the hot plate do not provide sufficient time for complete conversion as inferred from the rather large band gap of around 2.2 eV. The reason for this is either due to insufficient time for the layer to reach the necessary temperature at which cross-linking is triggered (i.e. $\sim$ 250 °C or higher) or due to insufficient time to complete the actual conversion process. For t_{conv} = 30–90 nm the sample's band gap has diminished by 0.4 eV to 1.8 eV due to further hydrogen outdiffusion. Additional prolongation of t_{conv} to

30 and 90 min results in no further decrease of the optical band gap compared to first 30 s. This observation indicates that at a conversion temperature of 450 °C the silicon matrix takes on a dense, cross-linked amorphous morphology within the initial 30 s and that thereafter no further major restructuring takes place.

However, inspection of the sub band gap region between 0.5–1.4 eV reveals that there is a slight increase in defect density for $t_{\mathrm{conv}} \geq 30$ min which is proposed to be caused by further Si−H bond cleavage resulting in the generation of Si dangling bonds. In summary, the experimental results suggest that ~ 2 min of pyrolysis at 450 °C should allow for ample time to allow for complete conversion of the silicon hydride polymer to a-Si:H.

4.4.3 Films Grown via Atmospheric Pressure Chemical Vapour Deposition using Trisilane

4.4.3.1 Using Sonophotolytically Treated Trisilane Solutions

Films grown by Atmospheric Pressure Chemical Vapour Deposition (APCVD) have significantly different properties and greatly exceed the optoelectronic performance of spin coated layers. This is true in spite of the rudimentary nature of the experimental setup consisting of an inverted petri dish and a hot plate.

The question immediately arises as to the utility of an ink composed of higher order silanes, polymeric silicon hydrides and Si-NPs, and what if any, effect their presence has on, for instance, lowering the temperature required for APCVD. The temperature required to decompose a silane molecule decreases as its chain length increases. For instance, monosilane decomposes thermally at around 400 °C, while disilane can be "cracked" at $\sim$ 370 °C [35] and trisilane at about 340 °C, and so the trend is toward lower temperatures the larger the silane molecule is. So at a given temperature, having silanes with more than 3 Si atoms should facilitate more bond breaking reactions at the heated substrate and hence contribute to faster film growth. Also, since thermal bond cleavage of a chain preferentially takes place at the middle of the chain, the decomposition products from silanes

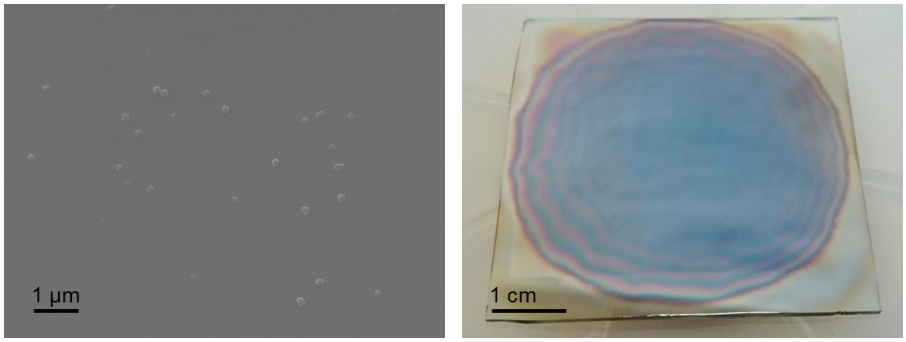

Figure 4.25: *(a) SEM image depicting silicon particles of* $\sim 200\,\text{nm}$ *in size deposited during film deposition via APCVD using an unfiltered formulation of the polysilane ink. Their presence indicates that particles suspended in the ink are also transported in the vapour phase toward the substrate during deposition. Note the smooth and featureless thin film between the particles demonstrating the homogeneity of APCVD films compared to spin coated samples.* ***(b)*** *Photograph of a typical* $\sim 100\,\text{nm}$ *thick APCVD layer on a* $5 \times 5\ \text{cm}^2$ *glass substrate using a standard (filtered) formulation of the TS ink.*

larger than trisilane are less likely to be small volatile species that could desorb from the substrate before reacting further on the hot surface [36]. This has been well documented where growth rates are compared using monosilane, disilane, trisilane and neopentasilane and where it is found that the larger silanes produce higher CVD deposition rates [37]. As corroborated by *Figure* 4.25a, the fact that much thicker layers are attainable with the composite ink is also attributed to the additional presence of dense Si-NPs which also make their way to the substrate to ultimately be integrated into the growing film.

Much faster film growth and thicker resulting layers are found for depositions via APCVD with the sonophotolytically prepared inks compared to those carried out using untreated TS/CO solutions (see next subsection). There is some evidence in the form of SEM images that supports the supposition that Si-NPs are transported in the vapour phase (i.e. in micro droplets) toward the substrate and hence contribute to faster film growth. Shown in *Figure* 4.25a is a SEM image of an a-Si:H thin film deposited using a ready-to-use, but unfiltered TS/CO solution.

Under the assumption that relatively large colloids of the order of $\sim 200\,\text{nm}$ can be transported in the vapour phase toward the substrate, it is postulated that smal-

ler particles, including nanoparticles of $< 10\,\text{nm}$ that are not directly observable via SEM, also make their way to the substrate thereby contributing to film growth. Apart from the obvious contribution of the dissolved polymer in sonophotolytically treated TS/CO solutions, the observation of Si-NPs on the surface of APCVD films suggests that they are assimilated into the films and hence also contribute to film growth. This helps account for the fact that ultrasonically treated TS inks produce much thicker films compared to untreated TS/CO solutions. With reference to the measurements presented in *Figure* 4.33 below, film thickness is found to increase with increasing substrate temperature. This result suggests that film growth via APCVD is thermally driven, where increasing temperature results in more decomposition reactions at the substrate as well as in an enhanced surface of reactive species in the vicinity of the surface of the growing film. As can be seen from the space between the particles in *Figure* 4.25a, APCVD films are typically very smooth and homogeneous, possessing no pinholes or micro-cracks. The photograph shown in *Figure* 4.25b demonstrates the macroscopic appearance of a typical APCVD layer. Note the increasing thickness homogeneity towards the centre of the sample where the heat distribution generated by the underlying hot plate is most homogeneous.

4.4.3.2 Using Untreated Trisilane Solutions

The question arises as to the feasibility of using an untreated TS/CO solution to deposit thin films via APCVD. To address this query, TS/CO solutions similar to those used for the sonophotolytic preparation described in the previous section are prepared (30–50 wt%) and used to grow films using a range of different substrate temperatures.

We find that it is indeed possible to grow films using untreated TS/CO solutions, however these are significantly thinner and of inferior electronic quality compared to those grown using treated solutions. In addition, onset temperature at which deposition is enabled is at about 425 °C, which is around 75 °C higher than that required when using the sonophotolytically prepared composite ink. The thinner layers are attributed to the high volatility of TS which results in gas leakage through the base of the petri dish. The higher temperatures required enable film

growth are attributed to the relatively high thermal decomposition temperature of TS at around 340 °C resulting in fewer "docking" reactions at the surface of the substrate or growing film. This is different to scenario with sonophotolytically treated inks where low volatility polymeric species are transported toward the substrate and subsequently partially decompose thereby generating more reactive sites with which other impinging molecules can react.

4.4.4 Summary of Film Deposition, Growth and Conversion

Two methods are used to deposit a-Si:H thin films, namely spin coating and APCVD. With inks prepared from CPS, spin coating of 100 nm thick layers was assigned an effective deposition rates of $\sim 20\,\mathrm{nm\,min^{-1}}$. With inks prepared from TS, faster effective deposition rates of $\sim 40\,\mathrm{nm\,min^{-1}}$ can be achieved. As will be shown in the next section, however, there is a substantial difference in the optoelectronic quality of the spin coated films fabricated from inks prepared from cyclopentasilane and those prepared from trisilane. On the other hand, although film growth via APCVD using inks prepared from TS is considerably slower at $\sim 5\,\mathrm{nm\,min^{-1}}$ compared to the effective deposition rates reached with spin coating, the thickness homogeneity and optoelectronic quality of APCVD films is far superior.

The deposition via APCVD using the sonophotolytically prepared ink from trisilane is fundamentally different in several respects compared to the method reported in the literature [65]. Firstly, the ink is used in the form of a solution in an organic solvent, namely CO. For one, this has the advantage that the effective boiling point of the mixture is increased compared to TS. This mitigates evaporative losses of unreacted TS in the ink, since TS also contributes to film growth. Moreover, the contents of the ink includes a homologous series of silanes up to (at least) octasilane, a branched higher silicon hydride as well as silicon nanoparticles, all three species of which exhibit excellent dilution and/or dispersion properties. This facilitates the coating of substrates at an increased rate since in addition to the contribution from decomposition reactions of the various silanes at the growing film, the vaporisation of the ink also enables the transport of pre-existing silicon hydride polymers and silicon nanoparticles toward the hot substrate, the latter two of which also contribute to film growth.

4.5 Thin Film Post-Treatment and Characterisation

This section is concerned with the post treatment and characterisation of thin films deposited via spin coating and APCVD using polysilane inks prepared as described in the preceding sections. The post treatment entails the exposure of a-Si:H to hydrogen radicals generated via hot-wire and the characterisation is undertaken using a several different techniques, including Fourier transform infrared spectroscopy (FTIR), electrical conductivity measurements, and photothermal deflection spectroscopy (PDS).

4.5.1 Hydrogen Radical Treatment via Hot-Wire

Hydrogen radical ($H^{\bullet}$) treatment of the films was carried out in order to improve their optoelectronic properties by rehydrogenating the films thereby passivating unsaturated Si bonds, otherwise known as dandling bonds, with atomic hydrogen. The effects of $H^{\bullet}$ treatment on a-Si:H thin films depends on a wide range of experimental parameters. These parameters include the filament temperature (T_{w}), the heater temperature (T_{heater}), the treatment time (t_{H}), the filament-substrate spacing ($d_{\mathrm{w\text{-}s}}$), the pressure (p), and the molecular hydrogen (H_2) flow rate (f). Once rough conditions were found that lead to the passivation of the layers and in order to restrict the vast parameter space, most of these parameters were held fixed to set values throughout the passivation runs. These include T_{w}, $d_{\mathrm{w\text{-}s}}$, p, and f.

The basic constraints on T_{w} are that it needs to be sufficiently high so as to enable the catalytic decomposition of H_2 and that an adequate $H^{\bullet}$ concentration ($c_{\mathrm{r}}ad$) should be produced to enable the passivation of the thin films in reasonable times of the order of minutes to hours. In addition, it was found that $T_{\mathrm{w}} \geq 1550\,^{\circ}\mathrm{C}$ lead to detrimental etching of the layers which hence provided an upper temperature limit for the experimental setup. Using known literature values as guides [13, 69], the flow and pressure are set to $f = 50\,\mathrm{sccm}$ and $p = 0.05\,\mathrm{mbar}$, respectively.

Table 4.2: *Summary of the parameters employed for the hydrogen radical treatment of the a-Si:H thin films fabricated from the liquid polysilane inks.*

Parameter		Fixed value	Variation range
Filament temperature	T_{w}	-	1300–1550 °C
Heater temperature	T_{heater}	-	400–450 °C
Treatment time	t_{H}	-	30–120 min
Filament-substrate spacing	$d_{\mathrm{w\text{-}s}}$	70 mm	-
Process pressure	p	0.05 mbar	-
H_2 flow rate	f	50 sccm	-

Although lower pressures in the range ~ 0.002 mbar are reported, it was not possible to reduce the process pressure any further due to the lower measuring limit of 0.01 mbar of the pressure gauge used.

Although $d_{\mathrm{w\text{-}s}}$ was fixed at 70 mm due to constructional limitations, its value was set as such so as to allow for sufficient distance to the filaments to mitigate unintentional heating and close enough to be within the mean free path length, l_{H} , of the generated radicals. Here, l_{H} is estimated via the following expression

$$l_{\mathrm{H}} = \frac{kT_{\mathrm{w}}}{\sqrt{2}\pi p d_{\mathrm{H}}^2}, \tag{4.1}$$

where Boltzmann's constant $k = 1.38 \times 10^{-2}\,\mathrm{m^2\,kg\,s^{-1}\,K^{-2}}$, T_{w} in the range 1500–1850 K, $p = 0.05$ mbar $= 5$ Pa, and the diameter of atomic hydrogen $d_{\mathrm{H}} = 74$ pm. With these values it is found that l_{H} lies in the range 170–210 mm, thus justifying the choice of $d_{\mathrm{w\text{-}s}}$.

The temperature of the substrates themselves was not directly determinable, however it plays a central role in the diffusion of $H^{\bullet}$ into the bulk of the thin films. For $T_{\mathrm{heater}} < 250$ °C strong etching of the films was observed, indicating that the $H^{\bullet}$ were predominantly surface-bound and did not possess sufficient mobility to diffuse into the bulk. The heater itself had a thermal tolerance limit of 450 °C and it is estimated that the substrates reach about 2/3 of this temperature. Hence, $T_{\mathrm{heater}} = 400$–450 °C in most experiments, which roughly corresponds to an actual substrate temperature, T_{sub}, of 265–300 °C. This temperature range is also appropriate since it is important that T_{sub} remains below the conversion temperature,

T_{conv}, at which the layers themselves were fabricated. With this parameter range t_{H} is varied from 0–120 min in steps of 30 min. *Table* 4.2 summarises the various parameters and their values.

The working range was found to be robust when considering the slight variation in the first two parameters, namely T_{w} and T_{heater}. As will be shown in the next section, the hydrogen content, microstructure and optoelectronic properties of treated films could be varied by changing t_{H}. In general, the most drastic improvement was achieved in the first 30 min, with only minor further improvements after 60 min. However, most samples submitted to 120 min of exposure showed neither signs of further improvement nor of degradation in quality.

4.5.2 Passivated Films from Inks Prepared from Cyclopentasilane

In the following, the effects of submitting a series of a-Si:H layers to increasingly longer $\mathrm{H}^{\bullet}$ treatment times are described. The films are spin coated on glass and c-Si substrates using a sonochemically prepared ink with CPS as precursor. The ink was prepared using a 12.6 wt% CPS/CO solution sonicated for 280 min at 65–70 °C. The passivation parameters were $T_{\mathrm{w}} = 1300\,^{\circ}\mathrm{C}$, $T_{\mathrm{heater}} = 450\,^{\circ}\mathrm{C}$, with $t_{\mathrm{H}} = 0, 30, 60$ and 120 min. The samples are analysed characterised by profilometry to determine their thickness d and FTIR is used to study their morphology via the microstructure factor R, and in conjunction with the measured d, to estimate their hydrogen content c_{H}. PDS measurements are carried out on similar samples deposited on glass. In addition, electrical conductivity measurements are also done to determine the optoelectronic performance of the films.

As depicted in *Figure* 4.26 **(a)**, the layers are progressively etched with increasing $\mathrm{H}^{\bullet}$ exposure. It should be pointed out that the 60 min sample exhibits an anomalously reduced d which is explained by rather pronounced thickness inhomogeneity from sample to sample, as well as within the films themselves. The morphology of the samples, however, shows a clear improvement with increasing t_{H}. Here, the untreated film possesses an $R = 75\,\%$, while the film passivated for

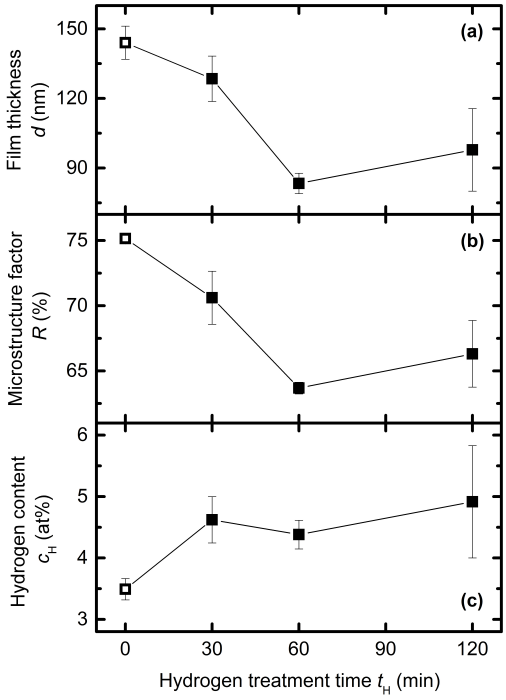

Figure 4.26: *Plots depicting changes in film thickness d, microstructure factor R and hydrogen content c_H as a function of hydrogen treatment time t_H for layers deposited via spin coating using a sonochemically prepared ink with CPS as precursor. In general, d decreases with increasing t_H due to H etching. R is also seen to continuously decrease indicating that preferentially more H is incorporated into monovalent dangling bonds in dense bulk material rather than at the internal surfaces of microvoids (refer to Figure 4.27a for the corresponding FTIR spectra). c_H reaches a maximum of about* 5.5 at% *for* $t_H = 60$ min*, thereafter diminishing slightly for the* 120 min *sample.*

60 min shows the best value of R at around 64 %. The 120 min sample exhibits a slightly increased R, nonetheless it remains low at 66 %. Interestingly, and as was the case for R, the amount of rehydrogenation of the films appears to make its most drastic improvement within the first 30–60 min of $H^{\bullet}$ treatment. A hydrogen concentration of 4.6 at% is reached for $t_{\mathrm{H}} = 30$ min and a quadrupling of t_{H}

does not result in much further H incorporation, where c_H is seen to increase only slightly to 4.9 at% for the 120 min sample.

The data points in **(b)** and **(c)** of *Figure* 4.26 (and in conjunction with the separately measured d) are derived from an analysis of the FTIR spectra shown in *Figure* 4.27a. The FTIR signals have been normalised in order to highlight the microstructural changes that occur in the films upon $H^\bullet$ treatment. Evidently, the relative growth of the 2000 cm^{-1} mode is in general agreement with the R vs. t_H trend in the central plot of *Figure* 4.26.

The plot in *Figure* 4.27b shows PDS spectra illustrating the corresponding changes in the absorption coefficient α as a function of photon energy $h\nu$ for twin layers deposited on glass substrates and subjected to $H^\bullet$ treatment for the times shown. The 30 and 60 min samples show similar behaviour with slightly reduced defect densities in the band gap between 1.0–1.4 eV. The 120 min sample, however, appears to have degenerated somewhat during passivation compared to the $t_H \leq 60$ min samples.

Lastly, the optoelectrical characterisation of the films via lateral electrical conductivity measurements are considered. Plotted in *Figure* 4.28 are the photoconductivity σ_{ph} on the left (blue) and dark conductivity σ_d (black) on the right as a function of t_H. As was the case for the microstructure and the hydrogen concentration, the most significant improvement in optoelectrical performance is reached after 30 min of $H^\bullet$ treatment in this series of measurements. Both σ_d and σ_{ph} improve by about an order of magnitude after passivation. Although the 120 min sample lost a third of its thickness upon passivation, it exhibited the highest σ_{ph} of 2.4×10^{-8} S cm^{-1} and the second lowest σ_d of 1.1×10^{-11} S cm^{-1}. Only minor variations in the conductivity values are evident after 30 min of treatment. The slight scattering in the values after treatment is attributed to inhomogeneities in film thickness and quality and not to actual improvements with increasing t_H.

In general, spin coated samples using CPS based inks prepared via sonication are found to attain a σ_d of 1×10^{-9}–9×10^{-11} S cm^{-1} and a σ_{ph} ranging from 1×10^{-8}–1×10^{-9} S cm^{-1}. This results in a σ_{PR} ranging from 1–10^2. After undergoing hydrogen radical treatment, the σ_d usually decreases to even lower values in

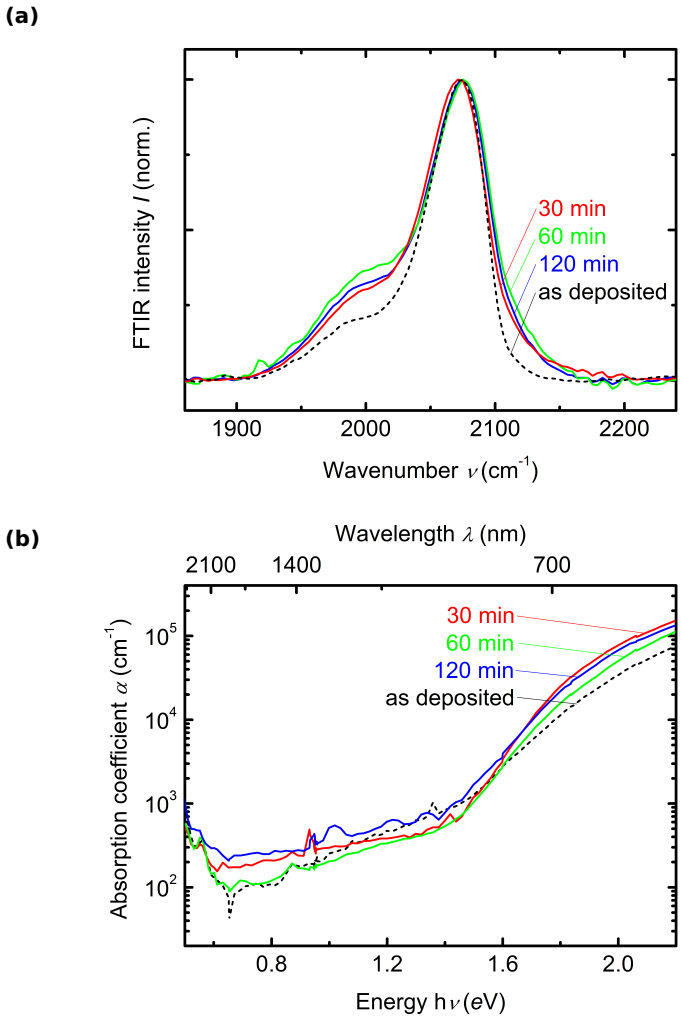

Figure 4.27: *The plot on the left shows the normalised FTIR spectra of the layers corresponding to the data presented in Figure 4.26. The spectra demonstrate the relative growth of the* $2000\,\mathrm{cm}^{-1}$ *mode upon H passivation for all samples. The plot on the right displays the PDS spectra for twin samples deposited on glass. There is a discernible improvement in the defect density between* 1.0–1.4 eV *for as well as slightly steeper band edge slopes for the 30 and* 60 min *samples. However, the* 120 min *sample appears to have deteriorated somewhat in these two respects. Note that the* 120 min *blue PDS curve has been smoothed for clarity.*

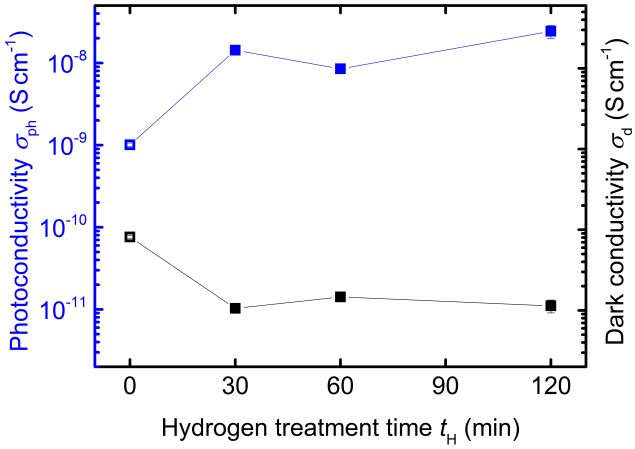

Figure 4.28: *Semi-logarithmic plot of the photoconductivity σ_{ph} in blue and dark conductivity σ_d in black versus hydrogen treatment time t_H. Most of the improvement is observed to take place within the first* 30 min *of passivation where σ_{ph} and σ_d are seen to increase and decrease by about an order of magnitude, respectively. Quadrupling the t_H to* 120 min *does not result in significant further improvements.*

the range of $3.0 \times 10^{-11}\,\mathrm{S\,cm^{-1}}$ and σ_{ph} increases only slightly to $2.4 \times 10^{-8}\,\mathrm{S\,cm^{-1}}$ for the best films. The σ_{PR} is hence improved to $\sim 10^3$ and a value of 2×10^3 was reached by the best sample. The values of σ_{ph} prior to and after hydrogen radical treatment lag behind known literature photoconductivities for spin coated films using CPS monomer by a factor of 10^2, where the literature standards lie in the range 5×10^{-6}–$9 \times 10^{-6}\,\mathrm{S\,cm^{-1}}$ [13]. This deficiency may be due to suboptimal hydridosilane polymer properties for optimal cross-linking, unoptimised passivation parameters or point to impurities in the CPS monomer batch.

4.5.3 Passivated Films from Inks Prepared from Trisilane

4.5.3.1 Spin Coated Films

The present section follows a similar structure to the previous one except that here films fabricated using a sonophotolytically synthesised ink with TS as precursor

are analysed. The ink was prepared using a 40 wt% TS/CO solution sonicated for 80 min at between−3–1 °C and subsequently irradiated with 365 nm UV light at room-temperature for ca. 40 hr. The passivation parameters used for these experiments were $T_{\mathrm{w}} = 1350\,^{\circ}\mathrm{C}$, $T_{\mathrm{heater}} = 450\,^{\circ}\mathrm{C}$, with $t_{\mathrm{H}} = 0, 30, 60$ and 120 min.

Once again, the thickness d of the samples is determined by profilometry. FTIR is used to derive the microstructure factor R, and in conjunction with the measured d, to estimate their hydrogen content c_{H}. On similar samples deposited on glass substrates PDS and electrical conductivity measurements are carried out.

Depicted in *Figure* 4.29 are the results of the H passivation experiments. In plot **(a)** once more it can be seen that exposure to atomic hydrogen leads to detrimental etching of the layers. The loss in d, however, is at most 25 nm as measured for the 120 min sample. This is significantly less than the $\sim$ 50 nm measured for the most highly etched CPS samples. As t_{H} is increased a continuous improvement of the morphology of the material is observed. Here $R = 62\,\%$ for the 60 min sample and after doubling t_{H} to 120 min, R drops to the very low value of 54 %. It should be pointed out that the intensity of the FTIR signal for the 120 min sample (see *Figure* 4.30a below) was considerably lower than for the other samples, in spite of the fact that its d was not significantly thinner. This is evident from the slightly larger signal-to-noise ratio of the normalised (blue) curve corresponding to the 120 min sample in the figure. Consequently, the hydrogen concentration in the films is not observed to continuously increase as was the case for the CPS layers, but rather it reaches a maximum of 7.7 at% after 60 min, thereafter falling sharply to 4.4 at% when t_{H} is doubled to 120 min.

Depicted in the plots of *Figure* 4.30a are the FTIR and PDS spectra corresponding to the same series under discussion. The normalised FTIR plot on the left makes evident the substantial evolution of the microstructure of the layers upon hydrogenation. Replicating the decreasing trend in R plotted in the central graph of *Figure* 4.29, a systematic growth of the 2000 cm^{-1} stretching mode relative to the one at 2080 cm^{-1} is observed. The as-deposited sample has an $R = 87\,\%$, which after 120 min of $\mathrm{H}^{\bullet}$ exposure decreases to the lowest value hitherto reported in the known literature for a spin coated layer of 54 %.

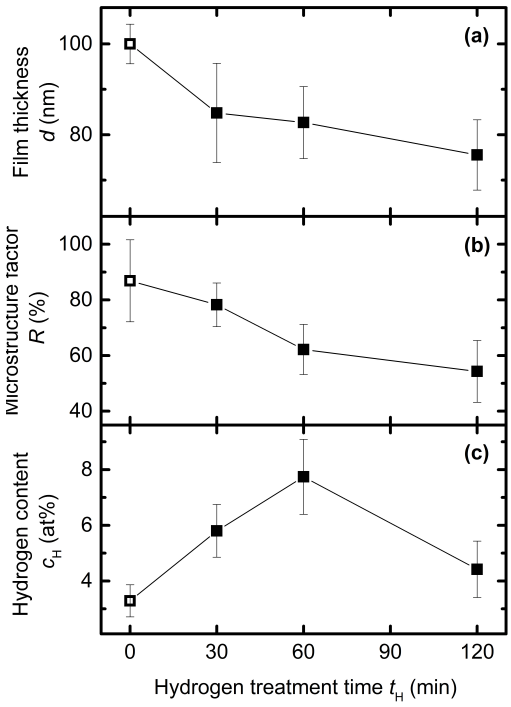

Figure 4.29: *Plots depicting changes in film thickness d, microstructure factor R and hydrogen content c_H as a function of hydrogen treatment time t_H for layers deposited via spin coating using a sonophotolytically prepared ink with TS as precursor. As t_H is increased, d decreases due to H etching as was the case for the CPS samples of Figure 4.26. R is also seen to continuously decrease, this being indicative of the saturation of dangling bonds in dense bulk material rather than at the internal surfaces of microvoids (refer to Figure 4.30a for the corresponding FTIR spectra). The c_H reaches a maximum of* 7.7 at% *for* $t_H = 60\,\text{min}$*, thereafter it diminishes significantly to* 4.4 at% *for the* 120 min *sample.*

The microstructural changes indicate that much of the atomic hydrogen that is incorporated into the a-Si matrix finds its way to Si dangling bond monovacancy sites in dense regions of the material and in so doing passivating unsaturated defects. Presented in *Figure* 4.30b are PDS spectra of similar films deposited on glass rather than on c-Si substrates. Here, however, a somewhat different picture

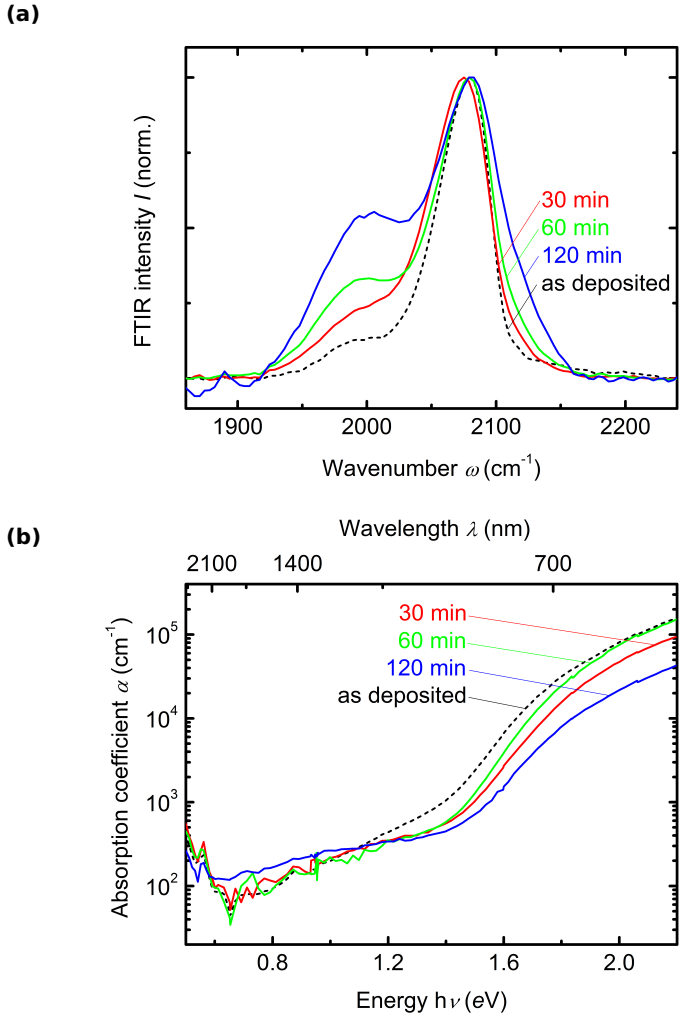

Figure 4.30: *(a) Plot of the normalised FTIR spectra of the layers corresponding to the data presented in Figure 4.29. The spectra demonstrate the systematic relative growth of the* $2000\,\mathrm{cm}^{-1}$ *mode upon H passivation for all samples. Note the slightly higher signal-to-noise ratio of the blue curve stemming from its much lower original intensity.* ***(b)*** *Plot displaying the PDS spectra for twin samples deposited on glass. There is a minor improvement in the defect density between* 1.0–1.4 eV *and the band edge slopes are slightly steeper for the* 30 *and* 60 min *samples. The band edge slope of the* 120 min *sample remains essentially unchanged. Also evident is the increase in band gap of the material after H passivation.*

as to the structural changes in the layers upon $H^{\bullet}$ treatment is observed. The absorption in the sub band gap region between 1.0–1.4 eV associated with dangling bond defects is only minimally reduced after passivation and even less so for the 120 min, which in the above account showed the highest relative passivation of dangling bonds as inferred via FTIR spectroscopy. These seemingly contradictory observations may be clarified by considering the fact that the measurements stem from two different samples, one spin coated in glass, the other on c-Si. The second thing to notice in the plots of the films after passivation is the increase in their E_{04}, i.e. the value of the band gap at $\alpha = 10^4\,\mathrm{cm}^{-1}$. The untreated layer has an $E_{04} = 1.64\,\mathrm{eV}$ and the one for the $t_\mathrm{H} = 120\,\mathrm{min}$ sample grows to 1.84 eV. It thus appears that although the 120 min sample did not possess the greatest concentration of H, its assimilation into the amorphous network and the associated passivation of dangling bonds resulted in the largest band gap increase of 0.2 eV. Finally, only for the 30 and 60 min samples does the slope of the band edge increase slightly, steeper slopes being associated with an enhanced near range order.

Lastly, the results of the optoelectrical characterisation of the TS-derived films via lateral electrical conductivity measurements are considered. Plotted in *Figure* 4.31 are the photoconductivity σ_ph (blue) and dark conductivity σ_d (black) as a function of t_H. Analogously to the case of CPS-derived films, the most significant improvement in optoelectrical performance is reached after 30 min of $H^{\bullet}$ treatment. Here, however, σ_d decreases by a factor of ~ 0.9 and σ_ph improves by almost two orders of magnitude after 30 min of passivation. In this series, the highest σ_ph was attained in the 120 min sample ($2.5 \times 10^{-7}\,\mathrm{S\,cm}^{-1}$). Only minor improvements in σ_ph are measured after 30 min of treatment and in terms of σ_PR, the layers are best for $t_\mathrm{H} \leq 60\,\mathrm{min}$. The accompanying increase in σ_d to $3.8 \times 10^{-10}\,\mathrm{S\,cm}^{-1}$ for the 120 min sample could not be fully explained.

Figure 4.32 includes plots for films fabricated from CPS based inks **(a)** and TS based inks **(b)** summarising the σ_d and σ_ph measurements for films with a variety of different thicknesses after $H^{\bullet}$ treatment. Immediately apparent is the broader scattering of the σ_d data points (grey shading) and the higher σ_ph reached with TS based inks (higher-lying light blue shading in **(b)**).

With reference to the hollow data points in *Figure* 4.32, untreated films prepared from TS-based inks typically have a σ_d in the range 1×10^{-8}–$5 \times 10^{-9}\,\mathrm{S\,cm}^{-1}$

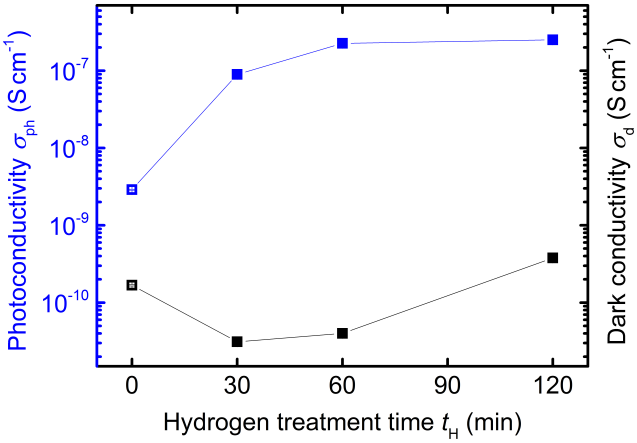

Figure 4.31: *Semi-logarithmic plot of the photoconductivity σ_{ph} in blue and dark conductivity σ_d in black versus hydrogen treatment time t_H for spin coated films using a TS based ink. Most of the improvement is observed to take place within the first* 30 min *of passivation, where σ_d reaches its lowest value and σ_{ph} has already improved by a factor of 30. Quadrupling t_H to* 120 min *results in a higher σ_d and a maximum improvement of σ_{ph} where it reaches* $2.5 \times 10^{-7}\,\mathrm{S\,cm^{-1}}$.

which is up to two orders of magnitude higher than their CPS counterparts. The σ_{ph} of untreated films is similar to that of layers fabricated from CPS based inks and lies in the range 2×10^{-8}–$6 \times 10^{-10}\,\mathrm{S\,cm^{-1}}$.

In general, prior to $\mathrm{H}^{\bullet}$ treatment the layers have a very poor initial σ_{PR} in the limited range of 0.1–10^1. Surprisingly, it is only after hydrogen passivation that the TS based films demonstrate their superior optoelectronic behaviour. While σ_{d} can decrease further to about $\sim 3.0 \times 10^{-11}\,\mathrm{S\,cm^{-1}}$, the σ_{ph} increases up to $2.8 \times 10^{-7}\,\mathrm{S\,cm^{-1}}$ for the best sample. Consequently, σ_{PR} reaches 5.7×10^3 which is a factor of roughly 2.9 better than films fabricated from CPS-based inks. It is, however, the higher σ_{ph} which is a factor of 12 greater that demonstrates that inks prepared from TS can be used to fabricate good quality a-Si:H thin films. The σ_{ph} of this films is, for instance, only a factor of ~ 9 lower than that of films fabricated from NPS based inks [14].

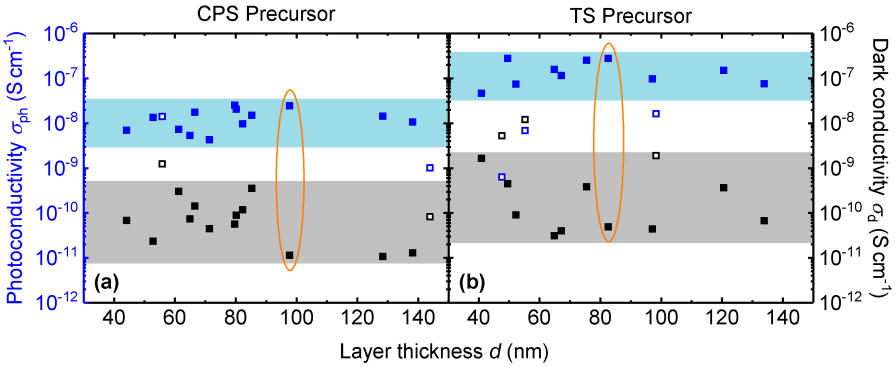

Figure 4.32: *Summary of dark (σ_d) and photoconductivity (σ_{ph}) measurements of spin coated samples of varying thickness after hydrogen radical treatment for inks prepared using CPS* ***(a)*** *and TS* ***(b)*** *as precursor. The empty squares represent exemplary untreated films and the orange ellipsoids indicate the films that attained the best photoresponse (σ_{ph}/σ_d).*

4.5.3.2 APCVD Films

In the following, the influence of the APCVD deposition temperature and H$^{\bullet}$ post-treatment on the optoelectronic quality of TS-derived films is addressed. As explained in *Chapter* 3, the APCVD deposition procedure involves preheating the substrates on the hot plate and covering them with an inverted petri dish previously coated with some ink and thereby creating a vaporised hydridosilane atmosphere within the enclosed space.

Figures 4.33 and 4.34 summarise an APCVD deposition series using a sonophotolytically synthesised ink and where the substrate temperature T_{sub} was varied between 325–450 °C. In *Figure* 4.33, the samples were characterised using profilometry to measure their thickness d and FTIR was employed to infer the morphology of the material in terms of the microstructure factor R. The concentration of hydrogen c_{H} in the films was estimated using d and the FTIR signal intensity as outlined in *Section* 2.3.2. Plot 28a) clearly shows that d increases with increasing T_{sub} which suggests that film growth via APCVD may be, at least partially, thermally driven. One would hence expect that as T_{sub} is raised that an increased number of decomposition reactions take place at the substrate surfaces which in

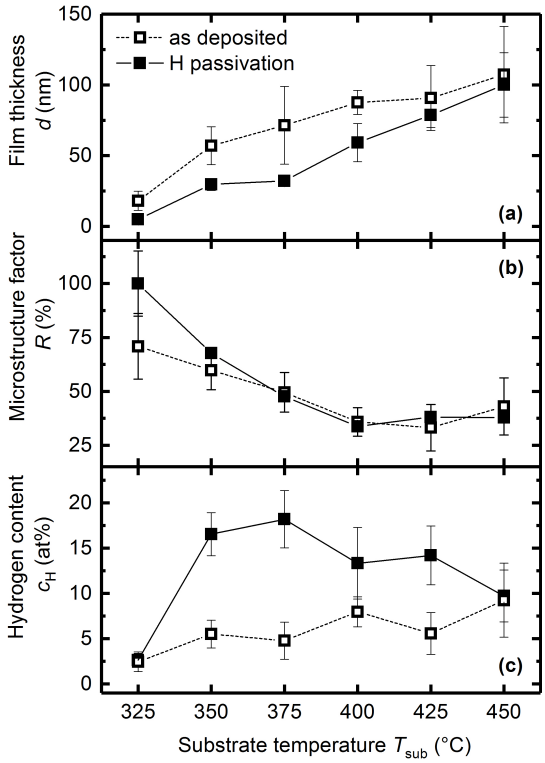

Figure 4.33: *Plots depicting changes in* **(a)** *film thickness d,* **(b)** *microstructure factor R and* **(c)** *hydrogen content c_H as a function of substrate temperature T_{sub} for layers deposited via APCVD before (dashed lines) and after (solid lines) $H^\bullet$ treatment at $T_{heater} = 450\,°C$. In general, d and c_H increase, while R decreases with increasing T_{sub}. Upon $H^\bullet$ treatment, the layers experience a reduction in d due to H etching. For T_{sub} between 350–425 °C, c_H increases substantially up to about 18 at% for the 375 °C sample. For $T_{sub} \geq 400\,°C$, R remains essentially unchanged.*

turn should lead to an increased growth rate. In addition, since the deposition is strictly speaking not a "closed-space" CVD technique, the precursor vapour can easily escape from the confines of the petri dish through the dish edge in contact with the hot plate. Thus if T_{sub} is not sufficiently high so as to promote film growth, the precursor vapour has a higher probability of leaking out of the reaction space before taking part in a reaction at the substrate. Also evident in the plot is

an average decrease of about 20 nm in film thickness over the whole temperature range after $H^{\bullet}$ treatment at a substrate heater tempearuture $T_{\text{heater}} = 450\,^{\circ}\text{C}$ due to $H^{\bullet}$ etching of the surface during passivation. In general, however, the relative loss in d, i.e. $(d_{\text{before}} - d_{\text{after}})/(d_{\text{before}} + d_{\text{after}})$, decreases from 56 rel% for the 350 °C sample to a mere 3.5 rel% for the 475 °C sample. This observation suggests that layers deposited at higher temperatures are denser and hence more resistant to unintentional $H^{\bullet}$ etching. It should be pointed out that APCVD films deposited (or spin coated films converted) at temperatures $< 350\,^{\circ}\text{C}$ possess very low conductivities with $\sigma_{\text{d}} \approx \sigma_{\text{ph}} \sim 10^{-10}\,\text{S}\,\text{cm}^{-1}$ and consequently have correspondingly low σ_{PR} in the range 0.5–5.

Plot **(b)** of *Figure* 4.33 reveals that R decreases to about 33 % as T_{sub} is increased up to around 400 °C. This indicates that the relative intensity of the monohydride stretching mode at $2000\,\text{cm}^{-1}$ is at its highest value in this temperature range. The reader will recall that this mode is associated with Si-H bonds where the H has passivated a previously unsaturated Si dangling bond at a monovacancy/divacancy site in a compact amorphous network. For $T_{\text{sub}} \geq 375\,^{\circ}\text{C}$ the value of R remains relatively constant at values between 50–33 % and is not strongly influenced by $H^{\bullet}$ treatment. This suggests that no major additional reconstruction of the a-Si matrix likely takes place for these temperatures during passivation. It should be noted that previous experience with substrate heating shows that $T_{\text{heater}} = 450\,^{\circ}\text{C}$ corresponds $T_{\text{sub}} \approx 300\,^{\circ}\text{C}$, i.e. roughly 2/3 of the heater temperature. This means that the samples deposited at $\leq 350\,^{\circ}\text{C}$ were submitted to similar temperatures during $H^{\bullet}$ treatment as during their actual fabrication. These two samples are also the ones exhibiting the most pronounced change in R after $H^{\bullet}$ treatment.

Finally, the hydrogen content c_{H} in the films before and after $H^{\bullet}$ treatment is shown in *Figure* 4.33 **(c)**. The analysis shows that as the deposition temperature is increased, the as-deposited layers are able to incorporate increasingly higher amounts of H during growth, where c_{H} exceeds the 9 at% mark at $T_{\text{sub}} = 450\,^{\circ}\text{C}$. The H content prior to and after H passivation is in films deposited at 325 °C and 450 °C remains constant at approximately 2.5 at% and 9.5 at%, respectively.

For the 325 °C sample this might be due to a polymer-like microstructure that does not respond well to hydrogenation upon $H^{\bullet}$ exposure but rather, prone to

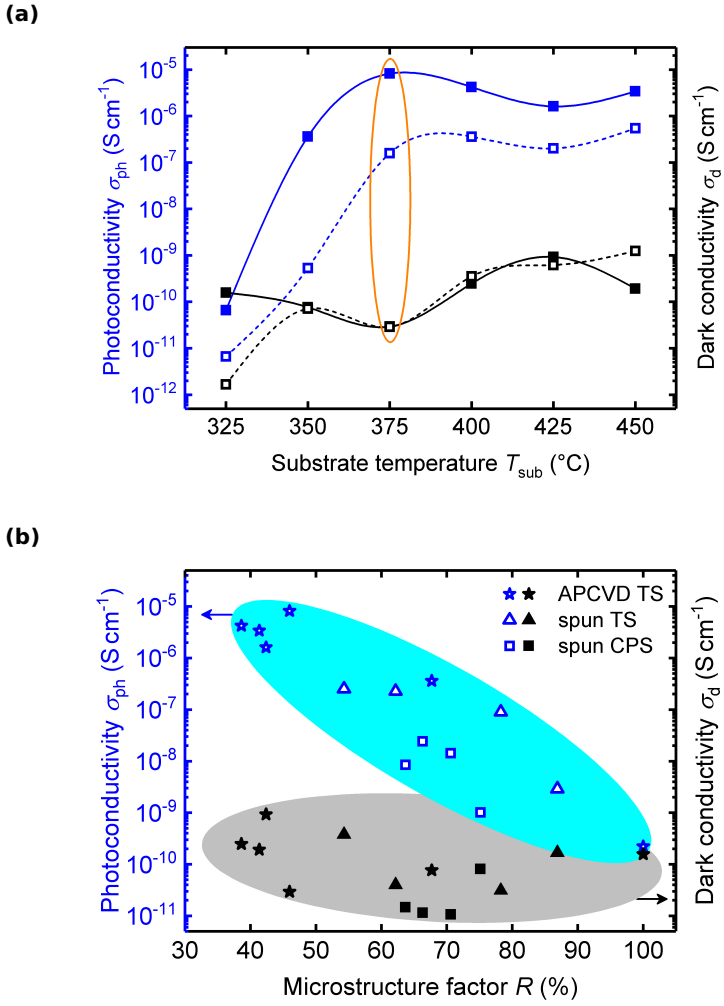

Figure 4.34: *(a) Plots of the photoconductivity σ_{ph} (blue data points) and dark conductivity σ_d as a function of substrate temperature T_{sub} for the same APCVD layers of Figure 4.33 before (dashed lines) and after (solid lines) $H^{\bullet}$ treatment. The orange ellipsoid highlights the film that attained the best photoresponse of 3×10^5. (b) Plot of σ_{ph} and σ_d versus microstructure factor R after $H^{\bullet}$ treatment for the APCVD TS samples of Figure 4.33, as well as the spun CPS and TS samples of Figures 4.26 and 4.29. Clearly apparent is the correlation between R and σ_{ph}, where independent of film fabrication technique or precursor ink, films with a more compact morphology (lower R) have higher σ_{ph}. No such trend is discernible for σ_d.*

$H^{\bullet}$ etching. The 450 °C film is presumably denser and less receptive to additional hydrogenation. Nonetheless, R does improve slightly after treatment which might be due to either the etching away of a predominantly microvoid rich surface or the additional diffusion of hydrogen to dangling bond sites at dense regions of the films or out-diffusion from voids. For intermediate temperatures between 350–425 °C the films respond strongly to $H^{\bullet}$ exposure where on average c_{H} increases by a factor 2.8 after treatment. Reference to *Figure* 4.33 **(b)** reveals that the significant additional incorporation of H into the films is not reflected in any systematic manner in the inferred morphology as estimated by the microstructure, since R remains stable within experimental uncertainty.

In *Figure* 4.34 the results of the optoelectrical performance characterisation by dark (σ_{d}) and photoconductivity (σ_{ph}) measurements is presented. The σ_{d} ranges from 10^{-9}–$10^{-11}\,\mathrm{S\,cm^{-1}}$ for unpassivated films and remains unaffected after H treatment for all temperatures except for the 325 °C and 450 °C samples. As evident from the FTIR measurements, both the 325 °C and the 325 °C sampled have rather poor microstructure factors both prior to and after $H^{\bullet}$ treatment. This microvoid-rich and presumably defect-rich morphology correlates well with the very low conductivities of the films. The correspondingly low σ_{ph} for this sample can also be explained by considering the fact that the films were partially transparent and hence possessed poor light absorbance. It should also be mentioned that the 325 °C films were very thin and their thickness was difficult to measure ($d_{\mathrm{before}} = 18\,\mathrm{nm}$, $d_{\mathrm{after}} = 5\,\mathrm{nm}$) so that the calculated conductivities are associated with rather large uncertainties.

For the 450 °C sample the σ_{d} is reduced by almost an order of magnitude reflecting the improvement in R seen in the central plot of *Figure* 4.33 as well as a slightly steeper band edge slope and a lower band gap defect density (see discussion of PDS measurements). For all other samples in the range $350\,^{\circ}\mathrm{C} \leq T_{\mathrm{sub}} \leq 425\,^{\circ}\mathrm{C}$, σ_{d} remains practically unchanged and the chief improvement is seen in the marked increase in σ_{d}, and in turn, in σ_{PR}. The improvement in σ_{ph} is seen to diminish in absolute magnitude as T_{sub} is raised, for instance the σ_{ph} of the 350 °C samples improves by a factor of 6.7×10^{2}, while that of the 425 °C sample by a mere 6.2.

In this series σ_{ph} appears to remain at a fairly flat maximum above $T_{\mathrm{sub}} = 350\,^{\circ}\mathrm{C}$. A maximum value of $8.2 \times 10^{-6}\,\mathrm{S\,cm^{-1}}$ is attained for the $T_{\mathrm{sub}} = 375\,^{\circ}\mathrm{C}$ sample.

The general decreasing trend in σ_{ph} and rising σ_d above 375 °C appears to correlate with the falling c_H found in *Figure* 4.34 **(b)** and not with the microstructure since R remains relatively constant throughout this temperature range. A summary of the optoelectronic performance of the best films fabricated in this work using inks prepared from CPS (spin coated) and TS (spin coated, APCVD, and p-type APCVD) as well as various state-of-the-art reference values from the literature is given in *Table* 4.3.

In order to highlight the material properties of the APCVD layers as they compare to PECVD films, *Figure* 4.35 shows the FTIR, PDS, and Raman spectra of the samples deposited at 400 °C which appear in *Figures* 4.33 and 4.34.

The FTIR spectra in *Figure* 4.35a show that there is still a significant contribution from the SiH/SiH_2 stretching mode at 2080 cm^{-1}, even after post-treatment with H radicals. The origin of this residual component, which is associated with H vibrations at the inner surface of microvoids. This morphology might be caused by insufficient mobility of reactive species (e.g. SiH_3 and H) in the vicinity of the film boundary during deposition which would hinder them from reaching docking sites that would otherwise lead to denser bulk material. Another plausible explanation is the deposition of larger silicon clusters or polymers which are already present in the vapourised ink. Since these would presumably already have a pre-existing morphology and a low mobility due to their size, they may not be easily assimilated into the growing film. Note that the curve after passivation appears to have a broadened right slope at $\sim$ 2100 cm^{-1}, which on account of the emergence of modes (not shown) in the range 840–910 cm^{-1} (refer to *Table* 4.1) is attributed to the formation of various polyhydrides at the surface of the film or at microvoids in the bulk.

As evident from the PDS spectra in *Figure* 4.35b, the as-deposited APCVD film is found to have an E_{04} optical band gap of ca. 1.79 eV, which increases slightly to 1.85 eV after $H^{\bullet}$ treatment due to more bonded hydrogen in the bulk. The absorption coefficient α is $\sim$ 50 cm^{-1} at 1.1 eV prior to and $\sim$ 20 cm^{-1} after passivation. This value of α is associated with dangling bond defects and is about a factor of 6 higher than that of state-or-the-art PECVD thin films. The shallower slope of the band tail or edge between 1.5–1.9 eV compared to the PECVD reference

Table 4.3: *Summary of the electrical conductivity performance of thin films made from CPS and TS based inks after pyrolytic conversion and hydrogen radical treatment. The PECVD reference values shown are the same as those given in [14]. All photoconductivity values are calculated from measurements carried out under approx. AM 1.5 illumination conditions.*

Material	Deposition method	Photoconductivity σ_{ph} ($S\,cm^{-1}$)	Dark conductivity σ_d ($S\,cm^{-1}$)	Photoresponse σ_{ph}/σ_d
CPS	Spin coating	2.4×10^{-8}	1.1×10^{-11}	2.2×10^{3}
TS	Spin coating	2.8×10^{-7}	4.8×10^{-11}	5.7×10^{3}
CPS[13]	Spin coating	9.0×10^{-6}	2.0×10^{-11}	4.5×10^{5}
NPS[14]	Spin coating	2.5×10^{-6}	3.3×10^{-11}	7.7×10^{4}
TS	Petri dish APCVD	8.2×10^{-6}	2.9×10^{-11}	2.8×10^{5}
CPS[66]	APCVD	1.1×10^{-5}	1.7×10^{-11}	6.4×10^{5}
Monosilane	PECVD	3.4×10^{-5}	1.4×10^{-10}	2.4×10^{5}
p-type TS	Petri dish APCVD	-	4.6×10^{-4}	-
p-type NPS[14]	Spin coating	-	1.1×10^{-3}	-
p-type CPS[65]	Petri dish APCVD	-	1.4×10^{-4}	-

suggests that the APCVD films have a higher degree of near range disorder as well as a higher concentration of charge carrier trapping states. The higher dangling bond defect density and shallower band tails are believed to be responsible for the slightly lower optoelectrical performance of the APCVD films as compared to solar grade PECVD material.

Lastly, the Raman spectra shown in *Figure* 4.35c give insights into the changes in atomic bonding brought about after exposure to H radicals. The as deposited film (dashed blue curve) exhibits three main phonon modes, namely the ω_{LA}, ω_{LO}, and ω_{TO} at $\sim 310\,cm^{-1}$, $\sim 400\,cm^{-1}$, and $470.1\,cm^{-1}$, respectively. The ω_{TO} phonon peak has a half width at half maximum (HWHM) calculated using the right half of the peak of $35.2\,cm^{-1}$. After passivation (solid blue curve), the ω_{TO} peak maximum and HWHM change to $474.9\,cm^{-1}$ and $33.5\,cm^{-1}$, respectively. Furthermore, the intensities of the ω_{LA} and ω_{LO} modes significantly decrease in intensity relative to ω_{TO}. The changes in peak position, width, and relative intensities are ascribed to modifications to the a-Si:H matrix brought about by rearrangement of weak Si-Si bonds and/or formation of new, more stable ones. The shift of ω_{TO} to higher wavenumbers is associated with a more relaxed network (i.e. less strained or stressed bonds).

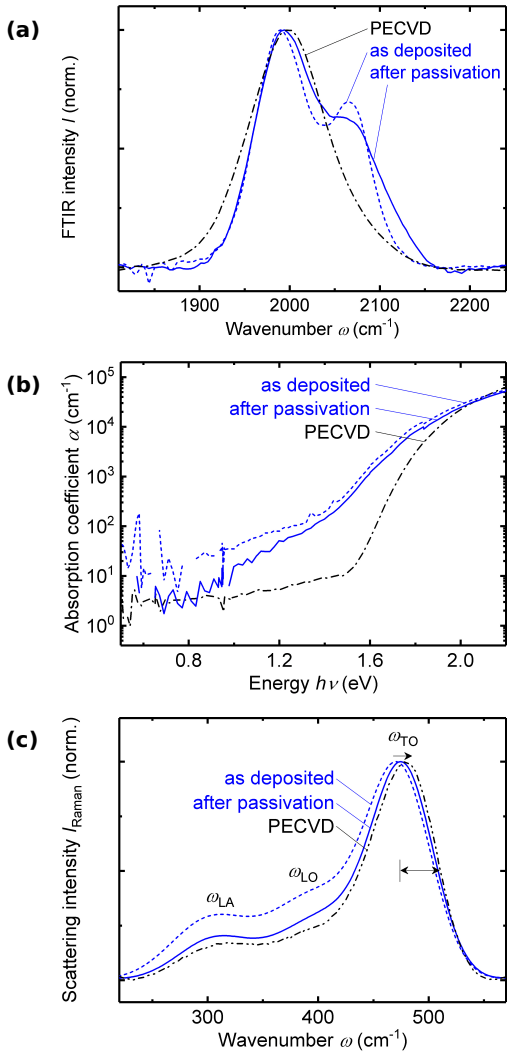

Figure 4.35: *Spectroscopic measurements corresponding to the APCVD samples from Figures 4.33 and 4.34 deposited at* 375 °C *prior to and after H passivation.* ***(a)*** *Normalised FTIR spectra depicting the Si-H stretching modes at* $\sim 2000\,\mathrm{cm}^{-1}$. ***(b)*** *PDS spectra of the sub band gap and band edge regions.* ***(c)*** *Normalised Raman spectra showing the* ω_{LA}, ω_{LO}, *and* ω_{TO} *phonon modes. For comparison, the plots also include reference curves for state-of-the-art PECVD layers.*

The accompanying narrowing is attributed to an increase in short range structural order due to a narrower distribution of strain and Si-Si bond angles as a result of matrix reconstruction upon exposure to atomic hydrogen. In accordance with Bronger at al. [14], the decrease in ω_{LO} points to enhanced medium range order (MRO) after passivation. For comparison, the state-of-the-art PECVD reference (black dot-dash curve) has a ω_{TO} peak maximum at higher wavenumber ($479.4\,\mathrm{cm}^{-1}$) and a narrower HWHM ($31.3\,\mathrm{cm}^{-1}$). The intensity of the ω_{LO} phonon is also weaker than for passivated APCVD material, indicating material with still higher MRO.

4.5.4 Summary of Film Post-Treatment and Characterisation

The post treatment of the a-Si:H thin films entailed their exposure to hydrogen radicals generated via hot-wire which, in general, resulted in a significant improvement of their optoelectronic properties. The characterisation involved spectroscopic techniques such as Fourier infrared spectroscopy and photothermal deflection spectroscopy. In addition, the layers were characterised optoelectrically by way of dark and photoconductivity measurements.

The results demonstrate that the polysilane inks prepared from both cyclopentasilane and trisilane can be successfully used to fabricate a-Si:H thin films suitable for application in semiconductor optoelectronic devices. In general, the films fabricated from cyclopentasilane-based inks demonstrated poorer optoelectronic performance compared to similarly spun films using trisilane-based inks. The disparity in quality was explained by, for instance, differences in film morphology and higher dangling bond defect densities as inferred from higher sub band gap absorption. This in turn may have its origins in the unoptimised nature of the ultrasonically synthesised polymer from cyclopenasilane monomer or, since the monomer is not of semiconductor-grade purity, in the presence of impurities.

While the spin coated layers fabricated from the trisilane-based ink are yet to attain the optoelectronic quality of films prepared from cyclopentasilane or

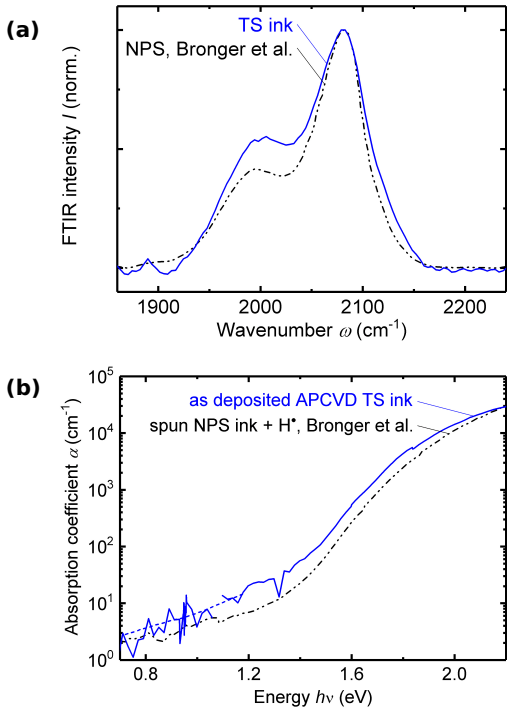

Figure 4.36: *(a) FTIR spectra depicting the Si−H stretching modes at* 2000–2080 cm^{-1} *for the best spin coated film using an ink prepared from TS (blue curve, same sample depicted in Figure 4.30a) compared to one prepared from a neopentasilane (NPS) based ink by Bronger et al. (black curve). Note that both films were been subjected to hydrogen radical treatment prior to measurement.* ***(b)*** *PDS spectra depicting the absorption coefficient* α *as a function of energy* $h\nu$ *for an as-deposited APCVD film (blue curve) compared to a spin coated film fabricated by Bronger et al. from a NPS based ink after hydrogen radical treatment (black curve). The dashed blue line between* 0.7–1.2 cm^{-1} *is simply a guide to the eye. Both NPS references are taken from [14].*

neopentasilane, it is believed that certain aspects of the films, such as the morphology, are on par with the state-of-the-art. *Figure* 4.36a shows two FTIR spectra of films deposited via spin coating, one using the trisilane-based ink (blue curve) and another using a neopentasilane (NPS) based ink (red curve). The red curve is quoted as having a microstructure factor (R) of 52 %, while the blue curve has $R = 54\,\%$. The similarity of their infrared morphologies, with significantly more

contribution from the 2000 cm^{-1} mode than was found for cyclopentasilane-derived material, leads us to infer that the higher silicon hydride polymer synthesised from trisilane and neopentasilane monomer is rather similar since the inks evidently lead to excellent cross-linking (i.e. to compact material with low R values) upon pyrolytic conversion and post-treatment with atomic hydrogen.

On the other hand, films deposited via APCVD yielded far superior material compared to that of spin coated layers. As of this writing, the best films deposited by APCVD have a band gap structure close to that of the best known solution-processed films where a band structure has been published, namely of spin coated neopentasilane-based inks by Bronger et al. Shown in *Figure* 4.36b are the PDS spectra of the best film to date (blue) compared to the film by Bronger et al. (red). Note that as opposed to the spun film, this APCVD film was measured as-deposited without any hot-wire $H^{\bullet}$ treatment. For this APCVD film, $E_{04} = 1.93$ eV compared to 1.98 eV for the reference. Also, the band tail of the APCVD film is slightly broader. The sub band gap absorption at 1.1 eV is roughly a factor of 2 higher for the APCVD film. Notwithstanding, this film possessed a high photoconductivity of 10^{-6} S cm^{-1}. It is hence believed that further optimisation of the APCVD technique should eventually permit the deposition of films with sufficiently high optoelectronic quality to discard with the need for post-depositional $H^{\bullet}$ treatment.

4.6 Optoelectronic Applications

4.6.1 Photovoltaic Devices

To test the utility of the intrinsic layers for optoelectronic applications, thin-film a-Si:H solar cells were fabricated. Since only undoped inks were available at the time of the experiments, the intrinsic absorber layer was solution-processed and the n and p-doped layers were deposited via PECVD. Since the n-type layer is known to be less affected by high temperature annealing than the p-layer, the layer stack was chosen in the n-i-p configuration. This allowed for the preparation of the i-layer, whose deposition by spin coating or APCVD requires $\sim 400\,^{\circ}\mathrm{C}$, on top of the n-layer without detrimentally affecting its electrical performance. *Figure* 4.37 shows a current density J versus voltage V (or JV) plot of two solar cells, where the i-layer was deposited via spin coating (red) or APCVD (blue).

Evident from the curves is the significant difference in photovoltaic performance between the two devices. With the exception of the absorber layer and its deposition method, both cells where identically processed and hence the differences are attributable to the thickness and optoelectrical quality of the i-layers. The spin coated layer had an estimated thickness of $\sim 80\,\mathrm{nm}$, while the APCVD layer was $\sim 120\,\mathrm{nm}$. The thicker APCVD absorber partly explains the higher I_{SC} of $10.0\,\mathrm{mA\,cm^{-2}}$ compared to the $2.85\,\mathrm{mA\,cm^{-2}}$ of the cell with the spun i-layer, since more light can be absorbed and hence more charge carriers can be generated in the former. More importantly, however, is the superior quality of APCVD material demonstrated in previous sections. The performance of APCVD was shown to supersede that of spun layers in practically every aspect, including microstructure, sub band gap defect density, and near-range order. This is reflected, for instance, in a lower series resistance R_{S} of $106\,\Omega$ (vs. $661\,\Omega$) and higher shunt resistance R_{Sh} of $2146\,\Omega$ (vs. $1457\,\Omega$) for the APCVD-layer device. Also apparent are the lower V_{oc}, J_{sc} and FF of the spun cell which can be ascribed to suboptimal film homogeneity, the presence of pinholes, and a comparatively low photoresponse.

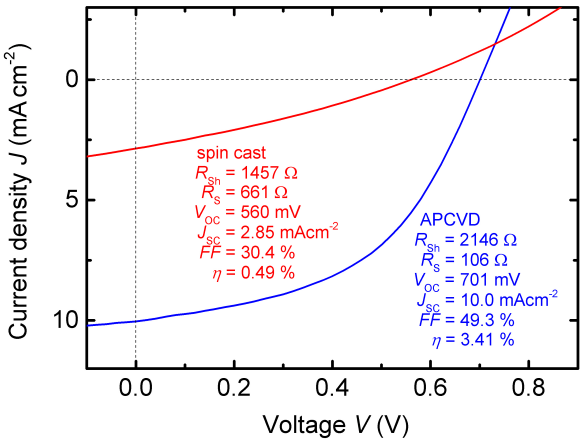

Figure 4.37: *JV curves of n-i-p type thin-film solar cells with PECVD n and p-doped layers and a solution-processed intrinsic absorber layer deposited via spin coating (red) or APCVD (blue) and submitted to $H^{\bullet}$ treatment. Both cells had an area of* $25\,\mathrm{mm}^2$ *and an effective area of* $19.8\,\mathrm{mm}^2$ *when shadowing from the Ag contact grid is taken into account. The quality of the APCVD cell is clearly superior, exhibiting an efficiency* η *of* $3.41\,\%$ *compared to* $0.49\,\%$ *for the spin cast cell.*

4.6.2 Passivation Layers

The high purity of the ink as well as the excellent surface coverage and the controllable growth rates possible with APCVD enabled the material to be used for the deposition of surface passivation layers.

Shown in *Figure* 4.38 are selected properties of an n-type c-Si wafer sample with both its front and rear faces passivated with thin 10–20 nm APCVD layers as described in *Section* 3.3.2. *Figure* 4.38a shows a log-log plot of effective minority carrier lifetime τ_{eff} versus Δp for the as-deposited (0 min) sample and after annealing at 220 °C for 30, 60 and 120 min. The arrow at $\Delta p = 10^{15}\,\mathrm{cm}^{-3}$ indicates the slightly decreasing value of τ_{eff} at a minority carrier density Δp of $10^{15}\,\mathrm{cm}^{-3}$ with increasing annealing time t_{A}. The data points and arrow labelled iV_{oc} show where the values of the implied open circuit voltage iV_{oc} were estimated.

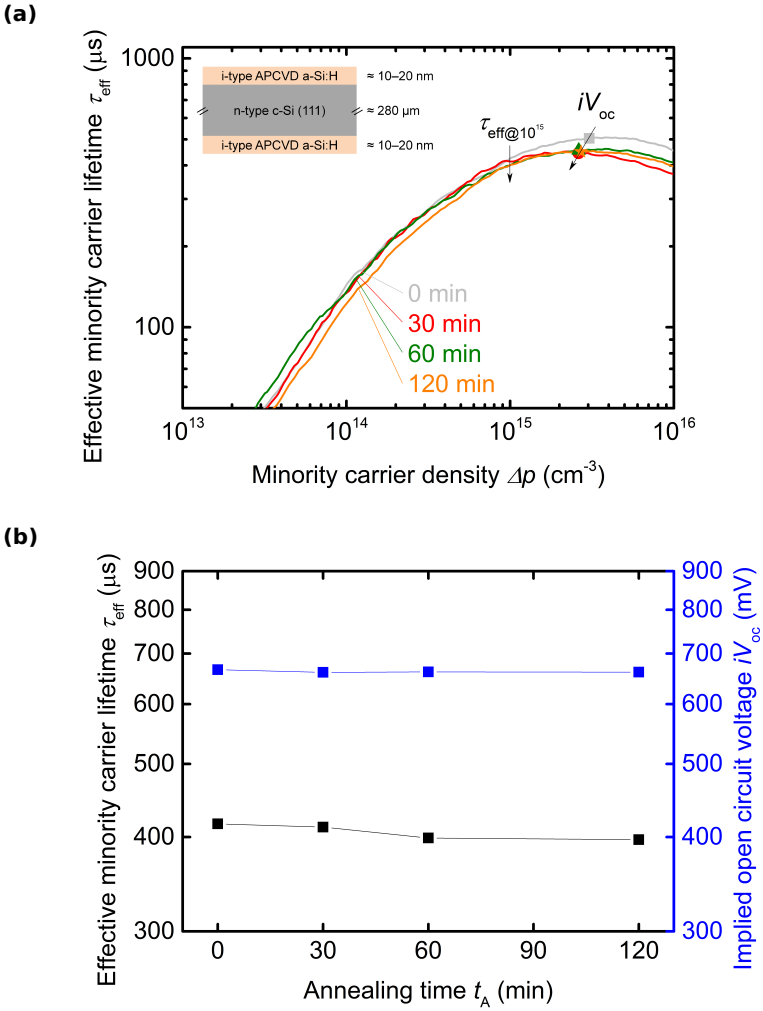

Figure 4.38: *Plots depicting selected passivation layer properties as a function of minority carrier density Δp and annealing time t_A.* ***(a)*** *Log-log plot of effective minority carrier lifetime τ_{eff} versus Δp for the as-deposited (0 min) sample and after 30, 60 and 120 min annealing at 220 °C. The layer stack is reproduced schematically in the inset. The arrow at $\Delta p = 10^{15}\,\mathrm{cm}^{-3}$ and the arrow labelled iV_{oc} indicate where the values for τ_{eff} and iV_{oc} were taken, respectively.* ***(b)*** *Half-logarithmic plot of τ_{eff} and iV_{oc} versus t_A. Here, both quantities reach their maximum values prior to annealing, namely 412 µs and 667 mV, respectively.*

Plotted in *Figure* 4.38b is a half-logarithmic plot of τ_{eff} and iV_{oc} as a function of t_{A}. Here, both quantities are highest prior to annealing, decreasing slightly, but remaining stable with increasing t_{A}. The best values of τ_{eff} and iV_{oc} are 412 µs and 667 mV, respectively. This value of τ_{eff} yields an effective surface recombination velocity $S_{\text{eff}} = 340\,\text{cm}\,\text{s}^{-1}$. Evidently the additional annealing at 220 °C did not result in an improvement of the passivation quality, which may be related to the higher temperature at which the layers where deposited ($\sim 350\,°\text{C}$).

4.6.3 Summary of Optoelectronic Applications

The implementation of intrinsic hydrogenated amorphous silicon thin films in optoelectronic devices was successfully demonstrated.

The n-i-p type thin-film solar cells were fabricated with PECVD n and p-doped layers, and intrinsic absorber layers deposited via spin coating and APCVD. The best cells with spin coated and APCVD absorbers had efficiencies of 0.49 % and 3.41 %, respectively. The poorer performance of the latter is ascribed to a combination of the use of a thicker absorber layer and the superior optoelectronic properties of APCVD material demonstrated in previous sections such as microstructure and photoresponse. For instance, typical photoconductivities (directly related to the light absorption quality of the cells) of APCVD layers were shown to be of the order of $5 \times 10^{-6}\,\text{S}\,\text{cm}^{-1}$, compared to $4 \times 10^{-7}\,\text{S}\,\text{cm}^{-1}$ for spun films. In addition, spun films are known to suffer from micron-sized pinholes and more pronounced thickness inhomogeneities which also help explain the low shunt resistance of the cell with the spin coated absorber.

Considering the rudimentary nature of the deposition method, the passivation of pristine crystalline silicon surfaces using intrinsic APCVD a-Si:H yielded satisfactory results. An n-type c-Si wafer was coated on both sides with thin 10–20 nm films and found to have effective minority charge carrier lifetimes and implied open circuit voltages > 400 µs and > 660 mV, respectively. The highest value for the effective surface recombination velocity was calculated to be $340\,\text{cm}\,\text{s}^{-1}$. Upon post-treatment via annealing at 220 °C the sample remained stable, with only minor deterioration of the passivation quality.

Chapter 5

Summary and Outlook

Summary

A low-temperature and solution-processing sonochemical route for the synthesis of polymeric and nanoparticulate hydrogenated silicon using cyclopentasilane and trisilane as starting materials was demonstrated. The three basic ingredients needed to carry out the synthesis are a liquid silane, an ultrasonic horn and an inert atmosphere. The resulting solutions and suspensions were subsequently used to produce high-quality thin films of both a-Si:H and silicon nanoparticles.

Cyclopentasilane, the smallest stable cyclic silane at stp, was shown to undergo ring-opening polymerisation via sonication without the action of ultraviolet light in the temperature range from 20–75 °C. Moreover, the polymerisation process and subsequent polymer growth were shown not to be pyrolytically activated due to the actual "macroscopic" temperature of the solution during treatment. Instead, these findings suggested that the mechanism responsible for the bond scission reactions must necessarily arise from the microscopic effects associated with acoustic cavitation. These conclusions were drawn from several experimental observations, among them comparisons of sonicated and pyrolysed solutions via size-exclusion chromatography and optical transmission measurements. The utility of the ink was demonstrated through the fabrication of a-Si:H thin films via spin coating. The films exhibited comparable optoelectrical and microstructural properties to layers

prepared from photolytically synthesised polydihydrosilane precursor inks found in the literature. Fourier transform infrared spectra of the untreated a-Si:H layers revealed a microvoid-rich morphology, which significantly improved after exposure to H radicals. After hydrogen passivation, the infrared microstructure factor (R) was calculated to be 72 %, constituting the lowest value reported thus far for a-Si:H films fabricated from a spin coated cyclopentasilane-derived ink. The dark and photoconductivity were likewise improved to 1.1×10^{-11} and $2.4 \times 10^{-8}\,\mathrm{S\,cm^{-1}}$, respectively. This yielded a photoresponse of 2.2×10^{3} for the best films after hydrogen radical treatment.

The second silicon hydride investigated was trisilane, a linear, thermally stable, and highly volatile molecule. Its behaviour under ultrasonic treatment yielded results that were in stark contrast to those found for low-volatility cyclopentasilane. It was revealed that initially transparent solutions of trisilane turn different shades of brown upon sonication and that this colouration was due to the production of silicon nanoparticles. The synthesis of the particles was hypothesised to originate at or in the vicinity of hot spots created during the collapse of acoustically generated microbubbles. It was also experimentally demonstrated that neither thermal treatment nor photolytically generated reactive species can be used to replicate the essentially immediate production of particles observed upon sonication. Furthermore, the observation of discrete and compact particles was attributed to a "fusion" effect during single cavitational collapse events rather than particles growing as a result of radicals undergoing subsequent nucleation reactions in the bulk of the liquid.

Detailed analysis using electron energy loss, photoluminescence, x-ray photoelectron, Fourier transform infrared, and Raman spectroscopy, as well as TEM, STEM, and SEM studies was carried out. It was found that variation of the concentration of trisilane in the solution or of the amplitude of the ultrasonic waves lead to the fusion of unoxidised, hydrogenated, and amorphous particles of tuneable size in the range 1.5–50 nm. The hydrogen content and surface hydride termination could also be modified by annealing the particles at different temperatures. Using a tip amplitude of 48 µm and a trisilane concentration of 47 wt% monodisperse particles of 2.96 ± 0.82 nm in diameter were synthesised. In contrast, similar solutions submitted to ultrasound generated using a higher tip amplitude of 192 µm were

shown to yield larger, more polydisperse particles in the range 10–50 nm. In addition, sustained ultrasonic irradiation under these conditions was demonstrated to result in highly porous, nanoscopic high surface area sponge or coral-like silicon nanoparticle agglomerates.

One of the properties of pristine trisilane that was remarked upon in the work was its transparency to ultraviolet light. Using gas chromatography - mass spectrometry sonication of trisilane solutions was found to produce higher order branched and linear silanes from tetrasilanes Si_4H_{10} through to octasilanes Si_8H_{18}, which were otherwise not observed in solutions submitted to irradiation with 365 nm light for the same amount of time. In a similar way, solutions submitted to thermal treatment at the highest temperatures typically reached during sonication of $\sim 65\,^{\circ}C$ did not undergo any colour changes , nor did they produce coatable inks. On the other hand, trisilane solutions pre-treated with ultrasound were found to be significantly more absorbing in the ultraviolet-to-visible range. After filtering, solutions submitted to a combined sonophotolytic treatment were shown to take on a clear lemon-yellow colour that was associated with a silicon sub-hydride polymer of the form $-(SiH_x)_n-$ with $1 < x < 2$. Nuclear magnetic resonance spectroscopy enabled a branched molecular structure to be established with an average ratio of SiH_3, SiH_2, and SiH silicon hydride groups of ca. 4:4:1. Since the filtering did not remove particles smaller that ca. 100 nm, inks prepared in this sonophotolytic manner were shown to constitute silicon hydride polymer - silicon nanoparticle composite mixtures.

The ink was subsequently used to deposit thin films of a-Si:H via spin coating and atmospheric pressure chemical vapour deposition (APCVD) using an inverted petri dish. Dark and photoconductivity of spun films after hydrogen radical treatment were 4.8×10^{-11} and $2.8 \times 10^{-7}\,S\,cm^{-1}$, respectively. The calculated photoresponse of 5.7×10^3 exceeded that of the best films prepared from the cyclopentasilane-derived ink. After hydrogen radical treatment a value for R of 54 % was attained, which is comparable to state-of-the-art films prepared from neopentasilane by Bronger et al. [14]. This indicated that good polymer cross-linking and reduced microvoid formation during pyrolytic conversion on the hot plate were achieved. The dark and photoconductivity of APCVD films reached

after hydrogen radical treatment were 2.9×10^{-11} and 8.2×10^{-6} S/cm, respectively. The resulting photoresponse of 2.8×10^{5} and R of 30–45 % indicated material with optoelectronic properties approaching those of solar-grade a-Si:H prepared via plasma enhanced chemical vapour deposition.

The high quality of this material enabled its implementation as the intrinsic absorber layer in n-i-p type thin-film solar cells and as passivation layer for clean c-Si wafer surfaces. The best cell exhibited a photovoltaic efficiency of 3.4 % over an area of 25 mm^2, while the best passivation layers yielded an effective lifetime of 412 µs and a surface recombination velocity of 34 cm s^{-1}.

Outlook

With the foundations now laid, the effects of other variables on the synthesis such as process temperature, tip amplitude and precursor concentration can now be studied more systematically. The sonication in this work was carried out using 26 kHz ultrasound, however, there is nothing impeding the use of ultrasonic horns vibrating at different frequencies. An investigation of the effects of alternative silanes and solvents, and their influence on the various synthesis products would certainly merit consideration. Throughout the work, relatively small volumes of $\sim$ 1.5 mL were used, however, the method is easily up-scalable to larger volumes using probes with larger tip area or multiple ultrasonic horns.

Compared to existing silicon nanoparticle synthesis methods, the method developed herein offers convenient simplifications such as vacuum-free processing and the requirement of only two substances, a liquid silane and a solvent (granting the availability of sufficient material, the sonication of undiluted silanes is also possible). While nanoparticles could be prepared with surprisingly narrow monodispersity, no special care was taken to attain this. Should the need arise, more involved sampling, filtering or centrifugation methods could be applied to improve the size distribution of the collected particles. Several issues concerning the silicon nanoparticles have thus far eluded clarification. For example: what role do the particles play in the enhancement of the photoreactivity of sonicated

solutions upon subsequent exposure to ultraviolet light? What are the conditions during particle "fusion"? And, how does one explain the presence of bonded hydrogen? In any case, the solution-processing nature of the synthesis may find use in biomedical applications such as nanoparticle-based drug delivery systems, where the direct embedment of the active substances during synthesis might be possible. Furthermore, the hydrogen termination and hydrogenated nature of the particles offer the easy option of subsequent surface functionalisation. The highly porous, sponge or coral-like silicon nanoparticle agglomerates are interesting in their own right and may find application in devices and processes requiring non-crystalline, nanoscopic high specific surface area architectures. One such example for their implementation would be as the basis of new anode materials in lithium-ion batteries.

As a proof-of-concept, a p-doped formulation of a trisilane-derived ink was successfully synthesised using decaborane. However, no variation of the preparation conditions were undertaken. Future work could focus on optimising this ink and developing n-type formulations using, e.g. white phosphorous. Doped inks would be of great value since they could be used, for instance, to print localised dot or stripe electrodes in back-contacted c-Si heterojunction solar cells. As reported by Masuda and co-workers [132, 161], another interesting extension to the work would be the fabrication of silicon carbide copolymer inks by carrying out the sonication in a partially reactive solvent such as cyclohexene, instead of inert cyclooctane. These considerations apply equally well to the preparation of p and n-doped silicon nanoparticles or silicon carbide composite particles.

The good performance of the optoelectronic applications considered in this work are encouraging, but there is still potential for improvement. For the best n-i-p cell, although only the absorber layer was solution-processed, the photovoltaic efficiency is on par with state-of-the-art devices made from liquid precursors [14, 65, 66]. On the other hand, the quality of the surface passivation using ultra-thin APCVD films actually exceeds that of similar solution-processed samples found in the literature [20]. The high quality of APCVD a-Si:H material makes an obvious case for its application in other devices such as thin-film transistors and HIT solar cells.

One of the virtues of solution-processing techniques is their associated circumvention of the use of expensive high-vacuum systems or energy intensive fabrication methods. Admittedly, however, a N_2-filled glove box does not constitute truly low-cost equipment. The rather large volume of the glove box could, in principle, be replaced by more affordable glass or plastic constructions based on Schlenk line technology or hermetic reaction vessels where the ultrasonic waves are transmitted from the outside into the interior through the casing.

The main factor driving up the cost of commercially available high-purity liquid silanes is chemical purity, which is a strict requirement for most applications in the semiconductor or photovoltaic industry. Another factor is the molecular or structural purity of the silane which, in the case of trisilane for instance, entails filtering out higher order silanes such as tetrasilane and pentasilane from the final product. While an exact analysis of the polymeric content of the trisilane-derived ink developed in this work is still lacking, it was nevertheless shown to consist of a mixture of higher order silanes, silicon sub-hydrides and silicon nanoparticles. This result raises questions as to the necessity of having to use solutions of pure monomer as opposed to a blend of silanes, since that is precisely what is produced during the preparation of the ink. The use of crude silane mixtures (analogous to crude oil) in the fabrication of printable inks could significantly reduce the costs of the raw silicon hydride precursor, since no fractionation or isolation of individual silanes would be required. This is particularly interesting with regard to the synthesis of silicon nanoparticles since, as was demonstrated with trisilane, with the correct choice of solvent the silanes could be deliberately allowed to diffuse into the microbubbles and "fused" into compact particles upon cavitational collapse, irrespective of their chain length.

In conclusion, the findings and methods presented in this work have the potential to boost the prospects for affordable silicon inks and make the synthesis of silicon nanoparticles more accessible to scientists working in ordinary chemistry labs around the world. Moreover, I trust that the use of ultrasound and liquid silicon hydrides will serve to stimulate exciting new developments in silicon sonochemistry and materials engineering for, among others things, energy generation and storage applications.

Acknowledgements

Where to begin? So many people accompanied and helped me in so many different ways that I can without a doubt state that I would not be writing this had it not been for them.

I'd like to start by thanking Prof. Bernhard Hidding and Dr. Friedhelm Finger for their original conception of the HITEC PhD topic to which I applied and whose assistance during the selection process helped me secure the fellowship. Many thanks also to Prof. Georg Pretzler from the HH University of Düsseldorf, and to Prof. Martin Möller and Dr. Xiaomin Zhu at the DWI-Leibniz Institute in Aachen for their supervision and allowing me to use their facilities during the first couple of months of my doctorate.

I am deeply indebted to my two direct supervisors Dr. Stefan Muthmann and Prof. Reinhard Carius for giving me such freedom to explore and develop my ideas without ever setting unreasonable constraints (but thank goodness they did set *some* limits) and for always encouraging me to keep on at it, especially when life was throwing me way too many lemons. Also, the many papers, posters, and presentations, let alone my thesis, would not have taken their final forms without their input. A huge thank you to Prof. Uwe Rau, for not only being my doctoral advisor, but especially for his continual academic support, keen personal interest in my work, and for the many amusing discussions during "fresh air breaks", be it in the Alps or outside our building.

Both personally and academically my time at the institute was immensely rewarding. I had the great fortune of having amazingly friendly, interesting, gifted, and culturally diverse colleagues. I'd like to thank Markus Hülsbeck for the really

fun times in the lab setting up experiments and our e-cigarettes discussions, Jan Flohre and Félix Urbain for making life in the office feel like being outdoors, Tobias Dyck, Bugra Turan, Samia Nadi, Aryak Singh, Pascal Kaienburg, Alexei Richter, Manuel Pomaska, Florian Staub, Chao Zhang, Andre Hoffmann, and Jan Mock for their friendship, especially outside of the institute. An astronomical thank you to Beatrix Blank for, among other things, her patience and advice using her acute sense for scientific presentation and communication. Special thanks go to Dai Trieu for entrusting me with the supervision of his thesis and the exciting time we spent working together. Those intense couple of months have, in fact, become the fondest memory I have of my research phase! My gratitude also goes to Joseph Klomfaß and Oliver Thimm for the help with all things technical and for the many PDS measurements. Thank you to Frank Pennartz, with whom I shared my first office, for the fun conversations and for his help with the PECVD layers, to Benjamin Klingebiel for the many "Ruhrpott" conversations and insights into the wonderful world of chemistry, and to Dr. Wolfhard Beyer for sharing some of his seemingly inexhaustible knowledge on hydrogen and silicon.

A very special thank you to my two sets of "German host parents" Conny & Klaus and Elke & Stephan for the many wonderful memories and support and encouragement throughout the years.

Finalmente, a mamá y papá, a mis hermanas Daniella y Javiera "Luigi" Luisina, y a mi sobrino Rocco quienes nunca han dejado de ser una presencia e inspiración indispensable en mi vida. Los amo tanto! No les puedo agradecer suficiente por todo el apoyo que me han brindado, especialmente durante los últimos años y a pesar de estar tan lejos, gracias totales!

Bibliography

1. Liu, N., Lu, Z., Zhao, J., McDowell, M. T., Lee, H.-W., Zhao, W. & Cui, Y. A pomegranate-inspired nanoscale design for large-volume-change lithium battery anodes. *Nat. Nanotechnol.* **9,** 187–192 (2014) (cit. on p. 1).
2. Wu, H., Zheng, G., Liu, N., Carney, T. J., Yang, Y. & Cui, Y. Engineering Empty Space between Si Nanoparticles for Lithium-Ion Battery Anodes. *Nano Lett.* **12,** 904–909 (2012) (cit. on p. 1).
3. McDowell, M. T., Lee, S. W., Harris, J. T., Korgel, B. A., Wang, C., Nix, W. D. & Cui, Y. In Situ TEM of Two-Phase Lithiation of Amorphous Silicon Nanospheres. *Nano Lett.* **13,** 758–764 (2013) (cit. on p. 1).
4. Delpuech, N., Mazouzi, D., Dupré, N., Moreau, P., Cerbelaud, M., Bridel, J. S., Badot, J.-C., De Vito, E., Guyomard, D., Lestriez, B. & Humbert, B. Critical Role of Silicon Nanoparticles Surface on Lithium Cell Electrochemical Performance Analyzed by FTIR, Raman, EELS, XPS, NMR, and BDS Spectroscopies. *J. Phys. Chem. C* **118,** 17318–17331 (2014) (cit. on p. 1).
5. O'Farrell, N., Houlton, A. & Horrocks, B. R. Silicon nanoparticles: applications in cell biology and medicine. *Int. J. Nanomedicine* **1,** 451–72 (2006) (cit. on p. 1).
6. Park, J.-H., Gu, L., von Maltzahn, G., Ruoslahti, E., Bhatia, S. N. & Sailor, M. J. Biodegradable luminescent porous silicon nanoparticles for in vivo applications. *Nat. Mater.* **8,** 331–336 (2009) (cit. on p. 1).
7. Osminkina, L., Nikolaev, A., Sviridov, A., Andronova, N., Tamarov, K., Gongalsky, M., Kudryavtsev, A., Treshalina, H. & Timoshenko, V. Porous silicon nanoparticles as efficient sensitizers for sonodynamic therapy of cancer. *Microporous Mesoporous Mater.* **210,** 169–175 (2015) (cit. on p. 1).

8. Holmes, J. D., Ziegler, K. J., Doty, R. C., Pell, L. E., Johnston, K. P. & Korgel, B. A. Highly Luminescent Silicon Nanocrystals with Discrete Optical Transitions. *J. Am. Chem. Soc.* **123,** 3743–3748 (2001) (cit. on p. 1).

9. Park, N.-M., Kim, T.-S. & Park, S.-J. Band gap engineering of amorphous silicon quantum dots for light-emitting diodes. *Appl. Phys. Lett.* **78,** 2575 (2001) (cit. on p. 1).

10. Eckhoff, D. A., Sutin, J. D. B., Clegg, R. M., Gratton, E., Rogozhina, E. V. & Braun, P. V. Optical Characterization of Ultrasmall Si Nanoparticles Prepared through Electrochemical Dispersion of Bulk Si. *J. Phys. Chem. B* **109,** 19786–19797 (2005) (cit. on p. 1).

11. Gupta, A., Swihart, M. T. & Wiggers, H. Luminescent Colloidal Dispersion of Silicon Quantum Dots from Microwave Plasma Synthesis: Exploring the Photoluminescence Behavior Across the Visible Spectrum. *Adv. Funct. Mater.* **19,** 696–703 (2009) (cit. on pp. 1, 22).

12. Shimoda, T., Matsuki, Y., Furusawa, M., Aoki, T., Yudasaka, I., Tanaka, H., Iwasawa, H., Wang, D., Miyasaka, M. & Takeuchi, Y. Solution-processed silicon films and transistors. *Nature* **440,** 783–786 (2006) (cit. on pp. 2, 8, 11, 13).

13. Masuda, T., Sotani, N., Hamada, H., Matsuki, Y. & Shimoda, T. Fabrication of solution-processed hydrogenated amorphous silicon single-junction solar cells. *Appl. Phys. Lett.* **100** (2012) (cit. on pp. 2, 14, 60, 99, 105, 117).

14. Bronger, T., Wöbkenberg, P. H., Wördenweber, J., Muthmann, S., Paetzold, U. W., Smirnov, V., Traut, S., Dagkaldiran, Ü., Wieber, S., Cölle, M., Prodi-Schwab, A., Wunnicke, O., Patz, M., Trocha, M., Rau, U. & Carius, R. Solution-Based Silicon in Thin-Film Solar Cells. *Adv. Energy Mater.* **4,** 1301871 (2014) (cit. on pp. 2, 11–14, 24, 60, 110, 117, 119, 120, 129, 131).

15. Sontheimer, T., Amkreutz, D., Schulz, K., Wöbkenberg, P. H., Guenther, C., Bakumov, V., Erz, J., Mader, C., Traut, S., Ruske, F., Weizman, M., Schnegg, A., Patz, M., Trocha, M., Wunnicke, O. & Rech, B. Solution-Processed Crystalline Silicon Thin-Film Solar Cells. *Adv. Mater. Interfaces* **1,** 1–6 (2014) (cit. on pp. 2, 11, 14).

16. Han, S., Dai, X., Loy, P., Lovaasen, J., Huether, J., Hoey, J. M., Wagner, A., Sandstrom, J., Bunzow, D., Swenson, O. F., Akhatov, I. S. & Schulz, D. L. Printed silicon as diode and FET materials - Preliminary results. *J. Non. Cryst. Solids* **354,** 2623–2626 (2008) (cit. on p. 2).

17. Ishihara, R., Zhang, J., Trifunovic, M., Van der Zwan, M., Takagishi, H., Kawajiri, R., Shimoda, T. & Beenakker, C. I. M. Single-grain Si TFTs fabricated by liquid-Si and long-pulse excimer-laser. *ECS Trans.* **50,** 49–53 (2012) (cit. on pp. 2, 11).

18. Zhang, J., Trifunovic, M., Van Der Zwan, M., Takagishi, H., Kawajiri, R., Shimoda, T., Beenakker, C. I. M. & Ishihara, R. Single-grain Si thin-film transistors on flexible polyimide substrate fabricated from doctor-blade coated liquid-Si. *Appl. Phys. Lett.* **102,** 1–5 (2013) (cit. on pp. 2, 14).

19. Mews, M., Mader, C., Traut, S., Sontheimer, T., Wunnicke, O., Korte, L. & Rech, B. Solution-processed amorphous silicon surface passivation layers. *Appl. Phys. Lett.* **105** (2014) (cit. on p. 2).

20. Guo, C., Ohdaira, K., Takagishi, H., Masuda, T., Shen, Z. & Shimoda, T. Formation of amorphous silicon passivation films with high stability against postannealing, air exposure, and light soaking using liquid silicon. *Jpn. J. Appl. Phys.* **55,** 04ES12 (2016) (cit. on pp. 2, 131).

21. Masuda, T., Takagishi, H., Yamazaki, K. & Shimoda, T. Direct Imprinting of Liquid Silicon. *ACS Appl. Mater. Interfaces* **8,** 9969–76 (2016) (cit. on p. 2).

22. Wöhler, F. & Buff, H. Über eine Verbindung von Silicium mit Wasserstoff. *Ann. der Chemie und Pharm.* **103,** 218–229 (1857) (cit. on p. 7).

23. Friedel, C. & Ladenburg, A. Ueber das Siliciumchloroform und dessen Derivate. *Ann. der Chemie und Pharm.* **143,** 118–128 (1867) (cit. on p. 7).

24. Moissan, H. & Smiles, S. Preparation et proprietis d'un nouvel hydriure de silicium. *J. Compt. Rend .* **134,** 569–575 (1902) (cit. on p. 7).

25. Stock, A. Bor- und Silicium-Chemie. Die experimentelle Erforschung leichtflüchtiger Stoffe. *Berichte der Dtsch. Chem. Gesellschaft* **54,** A142–A158 (1921) (cit. on p. 8).

26. Stock, A., Stiebeler, P. & Zeidler, F. Siliciumwasserstoffe, XVI.: Die höheren Siliciumhydride. *Berichte der Dtsch. Chem. Gesellschaft* **56,** 1695–1705 (1923) (cit. on pp. 8, 44).

27. Stock, A. Siliciumwasserstoffe. *Berichte der Bunsengesellschaft für Phys. Chemie* **32,** 341–349 (1926) (cit. on p. 8).

28. Fehér, F., Kuhlbörsch, G. & Luhleich, H. Beiträge zur Chemie des Siliciums und Germaniums. V. Über eine neue, einfache Arbeitstechnik zur Handhabung der Silane und anderer luft-oder feuchtigkeitsempfindlicher Flüssigkeiten. *Zeitschrift für Anorg. und Allg. Chemie* **303,** 294–302 (1960) (cit. on p. 8).

29. Fehér, F., Kuhlbörsch, G. & Luhleich, H. Beiträge zur Chemie des Siliciums und Germaniums. IV. Über die Darstellung des Rohsilas. *Zeitschrift für Anorg. und Allg. Chemie* **303,** 283–293 (1960) (cit. on p. 8).

30. Fehér, F. & Strack, H. Die gaschromatographische Trennung von Siliciumwasserstoffen an Squalan-Kieselgur-Trennsäulen. *Naturwissenschaften* **50,** 570–571 (1963) (cit. on pp. 8, 56).

31. Fehér, F. & Fischer, H. Raman- und ultrarotspektroskopische Untersuchungen an Silanen. *Naturwissenschaften* **51,** 461–461 (1964) (cit. on p. 8).

32. Fehér, F. *Kernresonanzspektroskopische Untersuchungen auf dem Gebiet der präparativen Chemie höherer Silane* (VS Verlag für Sozialwissenschaften, Wiesbaden, 1976) (cit. on pp. 8, 9, 12, 52, 53).

33. Hengge, E. & Bauer, G. Cyclopentasilane, the First Unsubstituted Cyclic Silicon Hydride. *Angew. Chemie Int. Ed. English* **12,** 316–316 (1973) (cit. on p. 8).

34. Vanderwielen, A. J., Ring, M. A. & O'Neal, H. E. Kinetics of the thermal decomposition of methyldisilane and trisilane. *J. Am. Chem. Soc.* **97,** 993–998 (1975) (cit. on pp. 8, 9, 59, 64, 74).

35. Tebben, E. M. & Ring, M. A. Pyrolysis of disilane and trisilane. *Inorg. Chem.* **8,** 1787–1789 (1969) (cit. on pp. 8, 59, 74, 95).

36. Alkorta, I. & Elguero, J. Theoretical study of the bond energy in n-silanes and n-germanes: Comparison with n-alkanes. *Chem. Phys. Lett.* **429,** 58–61 (2006) (cit. on pp. 8, 96).

37. Chung, K. H., Yao, N., Benziger, J., Sturm, J. C., Singh, K. K., Carlson, D. & Kuppurao, S. Ultrahigh growth rate of epitaxial silicon by chemical vapor deposition at low temperature with neopentasilane. *Appl. Phys. Lett.* **92,** 90–92 (2008) (cit. on pp. 8, 96).

38. Schmidt, D., Böhme, U., Seidel, J. & Kroke, E. Cyclopentasilane Si_5H_{10}: First single crystal X-ray structure of an oligosilane Si_xH_y and thermal analysis with TG/MS. *Inorg. Chem. Commun.* **35,** 92–95 (2013) (cit. on pp. 8, 9).

39. Guruvenket, S., Hoey, J. M., Anderson, K. J., Frohlich, M. T., Sailer, R. A. & Boudjouk, P. Aerosol assisted atmospheric pressure chemical vapor deposition of silicon thin films using liquid cyclic hydrosilanes. *Thin Solid Films* **589,** 465–471 (2015) (cit. on pp. 9, 13, 14).

40. Spanier, E. J. & MacDiarmid, A. G. The Conversion of Silane to Higher Silanes in a Silent Electric Discharge. *Inorg. Chem.* **1,** 432–433 (1962) (cit. on p. 9).

41. Fischer, I. *Beiträge zur präparativen Photochemie höherer Siliciumwasserstoffe* PhD (University of Cologne, 1976) (cit. on pp. 9, 11, 44, 56, 61).

42. Skrodzki, H. D. *Pyrolyse reiner Silane und des Rohsilans und molekülspektroskopische Untersuchungen an höheren Silanen* PhD (University of Cologne, 1974) (cit. on pp. 9, 59, 64).

43. Hengge, E. & Kovar, D. Preparation of Cyclohexasilane, Si_6H_{12}. *Angew. Chemie Int. Ed. English* **16,** 403–403 (1977) (cit. on p. 9).

44. Choi, S.-B., Kim, B.-K., Boudjouk, P. & Grier, D. G. Amine-Promoted Disproportionation and Redistribution of Trichlorosilane: Formation of Tetradecachlorocyclohexasilane Dianion 1. *J. Am. Chem. Soc.* **123,** 8117–8118 (2001) (cit. on p. 9).

45. Schott, G. Über die Farbe von Polysilanen. *Z. Chem.* **3,** 41–47 (1963) (cit. on pp. 9, 70, 74).

46. Schott, G. Aus der Chemie der Polysilane. *Z. Chem.* **2,** 194–200 (2010) (cit. on pp. 9, 44, 62).

47. Schott, G. & Hirschmann, E. Über Polysilane. II. Eigenschaften und Struktur von Polysilan(I). *Zeitschrift für Anorg. und Allg. Chemie* **288,** 9–14 (1956) (cit. on p. 9).

48. Hidding, B. *Untersuchung der Eignung von Silanen als Treibstoffe in der Luft-und Raumfahrt* MSc (Universität der Bundeswehr München, 2004) (cit. on pp. 9, 30).

49. Hidding, B., Pfitzner, M., Simone, D. & Bruno, C. Review of the potential of silanes as rocket/scramjet fuels. *Acta Astronaut.* **63,** 379–388 (2008) (cit. on p. 9).

50. Fehér, F., Hädicke, P. & Frings, H. Beiträge zur chemie des siliciums und germaniums, XXIII (1) physikalisch-chemische eigenschaften der silane von trisilan bis heptasilan. *Inorg. Nucl. Chem. Lett.* **9,** 931–936 (1973) (cit. on pp. 9, 69).

51. Lam, P. T., Sugiyama, A., Masuda, T., Shimoda, T., Otsuka, N. & Chi, D. H. Ab-initio study of intermolecular interaction and structure of liquid cyclopentasilane. *Chem. Phys.* **400,** 59–64 (2012) (cit. on p. 9).

52. Sugiyama, A., Shimoda, T. & Chi, D. H. Ab initio study of the polymerisation of cyclopentasilane. *Mol. Phys.* **108,** 1649–1653 (2010) (cit. on p. 9).

53. Dung, P. V., Lam, P. T., Duc, N. D., Sugiyama, A., Shimoda, T. & Chi, D. H. First-principles study of the thermally induced polymerization of cyclopentasilane. *Comput. Mater. Sci.* **49,** S21–S24 (2010) (cit. on p. 9).

54. Masuda, T., Matsuki, Y. & Shimoda, T. Pyrolytic transformation from polydihydrosilane to hydrogenated amorphous silicon film. *Thin Solid Films* **520,** 6603–6607 (2012) (cit. on pp. 9, 12, 13).

55. Masuda, T., Matsuki, Y. & Shimoda, T. Spectral parameters and Hamaker constants of silicon hydride compounds and organic solvents. *J. Colloid Interface Sci.* **340,** 298–305 (2009) (cit. on pp. 11, 13).

56. Masuda, T., Matsuki, Y. & Shimoda, T. Stability of polydihydrosilane liquid films on solid substrates. *Thin Solid Films* **520,** 5091–5096 (2012) (cit. on pp. 11, 13).

57. Shimoda, T. & Masuda, T. Liquid silicon and its application in electronics. *Jpn. J. Appl. Phys.* **53,** 02BA01 (2014) (cit. on pp. 11, 30, 66).

58. Furusawa, M. & Tanaka, H. in *Solut. Process. Inorg. Mater.* 131–155 (John Wiley & Sons, Inc., Hoboken, NJ, USA, 2008) (cit. on p. 11).

59. Kim, D. L., Pak, S. H., Kim, S. J., Park, S.-K. & Kim, H. J. The Effect of Ultraviolet Exposure on Solution Process of Silicon Thin Film. *Electrochem. Solid-State Lett.* **12,** E23 (2009) (cit. on p. 11).

60. Iyer, G. R. S., Hobbie, E. K., Guruvenket, S., Hoey, J. M., Anderson, K. J., Lovaasen, J., Gette, C., Schulz, D. L., Swenson, O. F., Elangovan, A. & Boudjouk, P. Solution-based synthesis of crystalline silicon from liquid silane through laser and chemical annealing. *ACS Appl. Mater. Interfaces* **4,** 2680–2685 (2012) (cit. on pp. 11, 12, 14).

61. Hengge, E. & Bauer, G. Darstellung und Eigenschaften von Cyclopentasilan. *Monatshefte für Chemie* **106,** 503–512 (1975) (cit. on pp. 12, 30).

62. Tanaka, H., Iwasawa, H., Wang, D., Toyoda, N., Aoki, T., Yudasaka, I., Matsuki, Y., Shimoda, T. & Furusawa, M. Spin-on n-Type Silicon Films Using Phosphorous-doped Polysilanes. *Jpn. J. Appl. Phys.* **46,** L886–L888 (2007) (cit. on p. 12).

63. Cádiz Bedini, A. P., Muthmann, S., Allgaier, J., Bittkau, K., Finger, F. & Carius, R. Liquid hydridosilane precursor prepared from cyclopentasilane via sonication at low temperatures without the action of light. *Ultrason. Sonochem.* **34,** 289–293 (2017) (cit. on pp. 13, 24, 70).

64. Cádiz Bedini, A. P., Muthmann, S., Flohre, J., Thiele, B., Willbold, S. & Carius, R. Sonophotolytically Synthesized Silicon Nanoparticle-Polymer Composite Ink from a Commercially Available Lower Silane. *Macromol. Chem. Phys.* **217,** 1655–1660 (2016) (cit. on pp. 13, 24, 44, 70, 74).

65. Masuda, T., Takagishi, H., Shen, Z., Ohdaira, K. & Shimoda, T. Phosphorus- and boron-doped hydrogenated amorphous silicon films prepared using vaporized liquid cyclopentasilane. *Thin Solid Films* **589,** 221–226 (2015) (cit. on pp. 14, 32, 98, 117, 131).

66. Shen, Z., Masuda, T., Takagishi, H., Ohdaira, K. & Shimoda, T. Fabrication of high-quality amorphous silicon film from cyclopentasilane by vapor deposition between two parallel substrates. *Chem. Commun.* **51,** 4417–4420 (2015) (cit. on pp. 14, 117, 131).

67. Wanka, H. N. & Schubert, M. B. High silicon etch rates by hot filament generated atomic hydrogen. *J. Phys. D. Appl. Phys.* **30,** L28–L31 (1997) (cit. on pp. 14, 34).

68. Murayama, H., Ohyama, T., Terakawa, A., Takagishi, H., Masuda, T., Ohdaira, K. & Shimoda, T. Effects of catalyst-generated atomic hydrogen treatment on amorphous silicon fabricated by Liquid-Si printing. *Jpn. J. Appl. Phys.* **53,** 05FM06 (2014) (cit. on pp. 14, 34).

69. Sakuma, Y., Ohdaira, K., Masuda, T., Takagishi, H., Shen, Z. & Shimoda, T. Effect of annealing and hydrogen radical treatment on the structure of solution-processed hydrogenated amorphous silicon films. *Jpn. J. Appl. Phys.* **53,** 04ER07 (2014) (cit. on pp. 14, 16, 34, 99).

70. Trifunovic, M., Shimoda, T. & Ishihara, R. Solution-processed polycrystalline silicon on paper. *Appl. Phys. Lett.* **106** (2015) (cit. on p. 14).

71. Chittick, R. C., Alexander, J. H. & Sterling, H. F. The Preparation and Properties of Amorphous Silicon. *J. Electrochem. Soc.* **116,** 77 (1969) (cit. on p. 15).

72. Street, R. A. *Hydrogenated Amorphous Silicon* (Cambridge University Press, Cambridge, 1991) (cit. on pp. 15, 16, 26).

73. Schülke, W. Structural investigation of hydrogenated amorphous silicon by X-ray diffraction. *Philos. Mag. Part B* **43,** 451–468 (1981) (cit. on p. 15).

74. Williamson, D. L., Mahan, A. H., Nelson, B. P. & Crandall, R. S. Microvoids in amorphous $Si_{1-x}C_x$:H alloys studied by small-angle x-ray scattering. *Appl. Phys. Lett.* **55,** 783 (1989) (cit. on pp. 15, 16).

75. Brodsky, M. H., Cardona, M. & Cuomo, J. J. Infrared and Raman spectra of the silicon-hydrogen bonds in amorphous silicon prepared by glow discharge and sputtering. *Phys. Rev. B* **16,** 3556–3571 (1977) (cit. on pp. 16, 36, 84).

76. Wagner, H. & Beyer, W. Reinterpretation of the silicon-hydrogen stretch frequencies in amorphous silicon. *Solid State Commun.* **48,** 585–587 (1983) (cit. on pp. 16, 17, 80).

77. Jousse, D., Bustarret, E. & Boulitrop, F. Disorder and defects in sputtered a-Si:H from subgap absorption measurements. *Solid State Commun.* **55,** 435–438 (1985) (cit. on p. 16).

78. Bhattacharya, E. & Mahan, A. H. Microstructure and the light-induced metastability in hydrogenated amorphous silicon. *Appl. Phys. Lett.* **52,** 1587 (1988) (cit. on p. 16).

79. Smets, A. H. M., Kessels, W. M. M. & van de Sanden, M. C. M. Vacancies and voids in hydrogenated amorphous silicon. *Appl. Phys. Lett.* **82,** 1547 (2003) (cit. on p. 17).

80. Beyer, W. & Ghazala, M. A. Absorption Strengths of Si-H Vibrational Modes in Hydrogenated Silicon. *MRS Proc.* **507,** 601 (1998) (cit. on p. 17).

81. Müllerová, J., Šutta, P., van Elzakker, G., Zeman, M. & Mikula, M. Microstructure of hydrogenated silicon thin films prepared from silane diluted with hydrogen. *Appl. Surf. Sci.* **254,** 3690–3695 (2008) (cit. on p. 17).

82. Langford, A. A., Fleet, M. L., Nelson, B. P., Lanford, W. A. & Maley, N. Infrared absorption strength and hydrogen content of hydrogenated amorphous silicon. *Phys. Rev. B* **45,** 13367–13377 (1992) (cit. on pp. 17, 18).

83. Maley, N. Critical investigation of the infrared-transmission-data analysis of hydrogenated amorphous silicon alloys. *Phys. Rev. B* **46,** 2078–2085 (1992) (cit. on p. 18).

84. Rech, B. & Wagner, H. Potential of amorphous silicon for solar cells. *Appl. Phys. A Mater. Sci. Process.* **69,** 155–167 (1999) (cit. on p. 18).

85. Pokhrel, N., Vabbina, P. K. & Pala, N. Sonochemistry: Science and Engineering. *Ultrason. Sonochem.* **29,** 104–128 (2016) (cit. on pp. 20, 75).

86. Leong, T., Ashokkumar, M. & Sandra, K. The fundamentals of power ultrasound - A review. *Acoust. Aust.* **39,** 54–63 (2011) (cit. on p. 20).

87. Wood, R. & Loomis, A. L. XXXVIII. The physical and biological effects of high-frequency sound-waves of great intensity. *London, Edinburgh, Dublin Philos. Mag. J. Sci.* **4,** 417–436 (1927) (cit. on p. 20).

88. Richards, W. T. & Loomis, A. L. The chemical effects of high frequency sound waves I. A preliminary survey. *J. Am. Chem. Soc.* **49,** 3086–3100 (1927) (cit. on p. 20).

89. Suslick, K. S. Sonochemistry. *Science.* **247,** 1439–1445 (1990) (cit. on p. 20).

90. T. J. Mason, D. P. *Practical Sonochemistry: Power Ultrasound Uses and Applications* 2nd ed. (Woodhead Publishing, Cambridge, 2011) (cit. on pp. 20, 75).

91. Cravotto, G. & Cintas, P. in *Handb. Appl. Ultrasound Sonochemistry Sustain.* (eds Chen, D., Sharma, S. K. & Mudhoo, A.) 23–40 (Taylor & Francis Group, LLC, Florida, 2012) (cit. on p. 20).

92. Price, G. J. Recent developments in sonochemical polymerisation. *Ultrason. Sonochem.* **10,** 277–283 (2003) (cit. on p. 20).

93. Price, G. J. Synthesis and modification of silicon-containing polymers using ultrasound. *Polym. Int.* **58,** 290–295 (2009) (cit. on p. 20).

94. Doktycz, S. & Suslick, K. Interparticle collisions driven by ultrasound. *Science.* **247,** 1067–1069 (1990) (cit. on pp. 20, 48).

95. Flint, E. B. & Suslick, K. S. The Temperature of Cavitation. *Science.* **253,** 1397–1399 (1991) (cit. on p. 21).

96. Mangolini, L. & Kortshagen, U. Plasma-Assisted Synthesis of Silicon Nanocrystal Inks. *Adv. Mater.* **19,** 2513–2519 (2007) (cit. on pp. 22, 75, 80).

97. Holm, J. & Roberts, J. T. Thermal Oxidation of 6 nm Aerosolized Silicon Nanoparticles: Size and Surface Chemistry Changes. *Langmuir* **23,** 11217–11224 (2007) (cit. on pp. 22, 80, 82).

98. Bywalez, R., Karacuban, H., Nienhaus, H., Schulz, C. & Wiggers, H. Stabilization of mid-sized silicon nanoparticles by functionalization with acrylic acid. *Nanoscale Res. Lett.* **7,** 76 (2012) (cit. on pp. 22, 85).

99. Wiggers, H., Starke, R. & Roth, P. Silicon Particle Formation by Pyrolysis of Silane in a Hot Wall Gasphase Reactor. *Chem. Eng. Technol.* **24,** 261–264 (2001) (cit. on p. 22).

100. Körmer, R., Jank, M., Ryssel, H., Schmid, H.-J. & Peukert, W. Aerosol synthesis of silicon nanoparticles with narrow size distribution,ÄîPart 1: Experimental investigations. *J. Aerosol Sci.* **41,** 998–1007 (2010) (cit. on p. 22).

101. Scriba, M., Arendse, C., Härting, M. & Britton, D. Hot-wire synthesis of Si nanoparticles. *Thin Solid Films* **516,** 844–846 (2008) (cit. on p. 22).

102. Furukawa, S. & Miyasato, T. Quantum size effects on the optical band gap of microcrystalline Si:H. *Phys. Rev. B* **38,** 5726–5729 (1988) (cit. on p. 22).

103. Seto, T., Kawakami, Y., Suzuki, N., Hirasawa, M. & Aya, N. Laser Synthesis of Uniform Silicon Single Nanodots. *Nano Lett.* **1,** 315–318 (2001) (cit. on p. 22).

104. Baldwin, R. K., Pettigrew, K. A., Ratai, E., Augustine, M. P. & Kauzlarich, S. M. Solution reduction synthesis of surface stabilized silicon nanoparticles. *Chem. Commun.* 1822–1823 (2002) (cit. on p. 22).

105. Neiner, D., Chiu, H. W. & Kauzlarich, S. M. Low-Temperature Solution Route to Macroscopic Amounts of Hydrogen Terminated Silicon Nanoparticles. *J. Am. Chem. Soc.* **128,** 11016–11017 (2006) (cit. on p. 22).

106. Wang, L., Lin, N., Zhou, J., Zhu, Y. & Qian, Y. Silicon nanoparticles obtained via a low temperature chemical "metathesis" synthesis route and their lithium-ion battery properties. *Chem. Commun.* **51,** 2345–2348 (2015) (cit. on p. 22).

107. Arul Dhas, N., Raj, C. P. & Gedanken, A. Preparation of Luminescent Silicon Nanoparticles: A Novel Sonochemical Approach. *Chem. Mater.* **10,** 3278–3281 (1998) (cit. on p. 22).

108. Heinrich, J. L., Curtis, C. L., Credo, G. M., Sailor, M. J. & Kavanagh, K. L. Luminescent Colloidal Silicon Suspensions from Porous Silicon. *Science.* **255,** 66–68 (1992) (cit. on p. 22).

109. Li, X., He, Y., Talukdar, S. S. & Swihart, M. T. Process for Preparing Macroscopic Quantities of Brightly Photoluminescent Silicon Nanoparticles with Emission Spanning the Visible Spectrum. *Langmuir* **19,** 8490–8496 (2003) (cit. on pp. 22, 87).

110. Li, X., He, Y. & Swihart, M. T. Surface Functionalization of Silicon Nanoparticles Produced by Laser-Driven Pyrolysis of Silane followed by $HF-HNO_3$ Etching. *Langmuir* **20,** 4720–4727 (2004) (cit. on p. 22).

111. Gedanken, A. Using sonochemistry for the fabrication of nanomaterials. *Ultrason. Sonochem.* **11,** 47–55 (2004) (cit. on p. 22).

112. Bang, J. H. & Suslick, K. S. Applications of Ultrasound to the Synthesis of Nanostructured Materials. *Adv. Mater.* **22,** 1039–1059 (2010) (cit. on p. 22).

113. Masuda, T., Matsuki, Y. & Shimoda, T. Characterization of polydihydrosilane by SEC-MALLS and viscometry. *Polym. (United Kingdom)* **53,** 2973–2978 (2012) (cit. on p. 24).

114. Berek, D. Size exclusion chromatography - A blessing and a curse of science and technology of synthetic polymers. *J. Sep. Sci.* **33,** 315–335 (2010) (cit. on p. 24).

115. Hübschmann, H.-J. *Handbuch der GC/MS* (Wiley-VCH Verlag GmbH & Co. KGaA, Weinheim, FRG, 1996) (cit. on pp. 24, 38).

116. Gottwald, W. *GC für Anwender* (VCH-Verlag, Weinheim, 1995) (cit. on pp. 24, 38).

117. Schomburg, G. *Gas Chromatography: A practical course* (VCH-Verlag, Weinheim, 1990) (cit. on pp. 24, 38).

118. Kintzinger, J.-P. & Marsmann, H. *Oxygen-17 and Silicon-29* 65–235 (Springer Berlin Heidelberg, Berlin, Heidelberg, 1981) (cit. on p. 24).

119. Derome, A. E. *Modern NMR Techniques for Chemistry Research* (Pergamon Press Ltd, Oxford, 1987) (cit. on p. 24).

120. Bermejo, D. & Cardona, M. Raman scattering in pure and hydrogenated amorphous germanium and silicon. *J. Non. Cryst. Solids* **32,** 405–419 (1979) (cit. on pp. 25, 84).

121. Hishikawa, Y. Raman study on the variation of the silicon network of a-Si:H. *J. Appl. Phys.* **62,** 3150–3155 (1987) (cit. on p. 25).

122. Gerbi, J. E., Voyles, P. M., Treacy, M. M. J., Gibson, J. M. & Abelson, J. R. Increasing medium-range order in amorphous silicon with low-energy ion bombardment. *Appl. Phys. Lett.* **82,** 3665–3667 (2003) (cit. on pp. 25, 84).

123. Muthmann, S., Köhler, F., Carius, R. & Gordijn, A. Structural order on different length scales in amorphous silicon investigated by Raman spectroscopy. *Phys. status solidi* **207,** 544–547 (2010) (cit. on p. 25).

124. Mahan, A. H., Carapella, J., Nelson, B. P., Crandall, R. S. & Balberg, I. Deposition of device quality, low H content amorphous silicon. *J. Appl. Phys.* **69,** 6728 (1991) (cit. on p. 26).

125. Carlson, D. E. in *Polycryst. Amorph. thin Film. devices* (ed Kazmerski, L. L.) 175–227 (Academic Press, New York, 1980) (cit. on p. 26).

126. Sproul, A. B. Dimensionless solution of the equation describing the effect of surface recombination on carrier decay in semiconductors. *J. Appl. Phys.* **76,** 2851–2854 (1994) (cit. on p. 27).

127. Hoex, B., Schmidt, J., Pohl, P., van de Sanden, M. C. M. & Kessels, W. M. M. Silicon surface passivation by atomic layer deposited Al_2O_3. *J. Appl. Phys.* **104,** 044903 (2008) (cit. on p. 27).

128. Kämpken, B. *Untersuchungen zur Herstellung höherer Silane für die Si-CVD* PhD (Goethe University of Frankfurt am Main, 2014) (cit. on p. 29).

129. Finke, H. L., Scott, D. W., Gross, M. E., Messerly, J. F. & Waddington, G. Cycloheptane, Cyclooctane and 1,3,5-Cycloheptatriene. Low Temperature Thermal Properties, Vapor Pressure and Derived Chemical Thermodynamic Properties. *J. Am. Chem. Soc.* **78,** 5469–5476 (1956) (cit. on p. 30).

130. Trenzado, J. L., Matos, J. S. & Alcalde, R. Volumetric properties and viscosities of the methyl butanoate + n-heptane + cyclo-octane ternary system at 283.15 and 313.15 K and its binary constituents in the temperature range from 283.15 to 313.15 K. *Fluid Phase Equilib.* **200,** 295–315 (2002) (cit. on p. 30).

131. Sigma-Aldrich. *Safety Data Sheet: Cyclooctane* 2014 (cit. on p. 30).

132. Masuda, T., Shen, Z., Takagishi, H., Ohdaira, K. & Shimoda, T. Amorphous silicon carbide films prepared using vaporized silicon ink. *Jpn. J. Appl. Phys.* **53,** 031304 (2014) (cit. on pp. 32, 131).

133. Umemoto, H., Ohara, K., Morita, D., Nozaki, Y., Masuda, A. & Matsumura, H. Direct detection of H atoms in the catalytic chemical vapor deposition of the SiH_4/H_2 system. *J. Appl. Phys.* **91,** 1650 (2002) (cit. on p. 34).

134. Matsumura, H. & Ohdaira, K. *Cat-CVD (Catalytic-CVD); Its Fundamentals and Application* in *ECS Trans.* (ECS, 2009), 53–63 (cit. on p. 34).

135. Pollard, W. B. & Lucovsky, G. Phonons in polysilane alloys. *Phys. Rev. B* **26,** 3172–3180 (1982) (cit. on p. 36).

136. Boccara, A. C., Fournier, D. & Badoz, J. Thermo-optical spectroscopy: Detection by the "mirage effect". *Appl. Phys. Lett.* **36,** 130 (1980) (cit. on p. 37).

137. Boccara, A. C., Jackson, W., Amer, N. M. & Fournier, D. Sensitive photothermal deflection technique for measuring absorption in optically thin media. *Opt. Lett.* **5,** 377 (1980) (cit. on p. 37).

138. Jackson, W. B., Amer, N. M., Boccara, A. C. & Fournier, D. Photothermal deflection spectroscopy and detection. *Appl. Opt.* **20,** 1333 (1981) (cit. on p. 37).

139. Höhne, N. *PDS als Charakterisierungsmethode für Dünnschichtsolarzellen aus amorphem Silizium* Diplom (RWTH Aachen, 1997) (cit. on p. 37).

140. Beckers, F. *Ladungsträgertransport- und Rekombinationsunterschungen an pin-Dioden aus amorphem Silizium (a-Si:H) im Vorwärtsstrombetrieb* PhD (University of Düsseldorf, 1994) (cit. on p. 37).

141. Hilgenberg, B. *Photothermische Deflektionsspektroskopie an amorphem Silizium* Diplom (Marburg, 1986) (cit. on p. 37).

142. Sinton, R. A. & Cuevas, A. Contactless determination of current-voltage characteristics and minority-carrier lifetimes in semiconductors from quasi-steady-state photoconductance data. *Appl. Phys. Lett.* **69,** 2510–2512 (1996) (cit. on p. 42).

143. Fehér, F., Schinkitz, D. & Schaaf, J. Ein Verfahren zur Darstellung höherer Silane. *Zeitschrift für Anorg. und Allg. Chemie* **383,** 303–313 (1971) (cit. on p. 56).

144. Zou, J., Baldwin, R. K., Pettigrew, K. A. & Kauzlarich, S. M. Solution Synthesis of Ultrastable Luminescent Siloxane-Coated Silicon Nanoparticles. *Nano Lett.* **4,** 1181–1186 (2004) (cit. on p. 75).

145. Marra, D. C. Silicon hydride composition of plasma-deposited hydrogenated amorphous and nanocrystalline silicon films and surfaces. *J. Vac. Sci. Technol. A Vacuum, Surfaces, Film.* **16,** 3199 (1998) (cit. on p. 80).

146. Burrows, V. A., Chabal, Y. J., Higashi, G. S., Raghavachari, K. & Christman, S. B. Infrared spectroscopy of Si(111) surfaces after HF treatment: Hydrogen termination and surface morphology. *Appl. Phys. Lett.* **53,** 998 (1988) (cit. on p. 80).

147. Knights, J., Street, R. & Lucovsky, G. Electronic and structural properties of plasma-deposited a-Si:O:H - The story of O_2. *J. Non. Cryst. Solids* **35-36,** 279–284 (1980) (cit. on p. 82).

148. Dutta Gupta, N. & Chaudhuri, P. Effect of oxygen contamination on the properties of the silicon hydrogen alloy materials deposited under conditions near the microcrystalline silicon formation region. *J. Non. Cryst. Solids* **289,** 168–174 (2001) (cit. on p. 82).

149. Kravets, V. G., Meier, C., Konjhodzic, D., Lorke, A. & Wiggers, H. Infrared properties of silicon nanoparticles. *J. Appl. Phys.* **97,** 084306 (2005) (cit. on p. 82).

150. Ley, L., Reichardt, J. & Johnson, R. L. Static Charge Fluctuations in Amorphous Silicon. *Phys. Rev. Lett.* **49,** 1664–1667 (1982) (cit. on p. 85).

151. Cerofolini, G. F., Galati, C. & Renna, L. Si 2p XPS spectrum of the hydrogen-terminated (100) surface of device-quality silicon. *Surf. Interface Anal.* **35,** 968–973 (2003) (cit. on p. 85).

152. Banaszak Holl, M. M. & McFeely, F. R. Si/SiO_2 Interface: New Structures and Well-Defined Model Systems. *Phys. Rev. Lett.* 2441–2444 (cit. on p. 85).

153. Alam, A. U., Howlader, M. M. R. & Deen, M. J. Oxygen Plasma and Humidity Dependent Surface Analysis of Silicon, Silicon Dioxide and Glass for Direct Wafer Bonding. *ECS J. Solid State Sci. Technol.* **2,** P515–P523 (2013) (cit. on p. 85).

154. He, J.-W., Xu, X., Corneille, J. & Goodman, D. X-ray photoelectron spectroscopic characterization of ultra-thin silicon oxide films on a Mo(100) surface. *Surf. Sci.* **279,** 119–126 (1992) (cit. on p. 85).

155. Rochet, F., Poncey, C., Dufour, G., Roulet, H., Guillot, C. & Sirotti, F. Suboxides at the Si/SiO_2 interface: a Si 2p core level study with synchrotron radiation. *J. Non. Cryst. Solids* **216,** 148–155 (1997) (cit. on p. 85).

156. Poncey, C., Rochet, F., Dufour, G., Roulet, H., Sirotti, F. & Panaccione, G. Adsorption of water on Si(001)-2 × 1 and Si(111)-7 × 7 surfaces at 90 and 300 K: A Si 2p core-level and valence band study with synchrotron radiation. *Surf. Sci.* **338,** 143–156 (1995) (cit. on p. 85).

157. Oh, J. H., Yeom, H. W., Hagimoto, Y., Ono, K., Oshima, M., Hirashita, N., Nywa, M., Toriumi, A. & Kakizaki, A. Chemical Structure of the Ultrathin SiO_2/Si(100) interface: An Angle-Resolved Si 2p Photoemission Study. *Phys. Rev. B* **63,** 205310 (2001) (cit. on p. 85).

158. Sun, Y., Feldman, A. & Farabaugh, E. X-ray photoelectron spectroscopy of O 1s and Si 2p lines in films of SiO_x formed by electron beam evaporation. *Thin Solid Films* **157,** 351–360 (1988) (cit. on p. 87).

159. Mühlhoff, L. & Bolze, T. Surface analytical characterization of oxide-free Si(100) wafer surfaces. *Fresen. Z. Anal. Chem.* **333,** 527–530 (1989) (cit. on p. 87).

160. Anandan, C. & Williams, R. H. Investigation of HF etched hydrogenated amorphous silicon surfaces by X-ray photoelectron spectroscopy. *Semicond. Sci. Technol.* **5,** 265–268 (1990) (cit. on p. 87).

161. Masuda, T., Iwasaka, A., Takagishi, H. & Shimoda, T. Polymeric precursor for solution-processed amorphous silicon carbide. *J. Mater. Chem. C* **3,** 12212–12219 (2015) (cit. on p. 131).

Band / Volume 409
Reactions between nitrite and soil organic matter and their role in nitrogen trace gas emissions and nitrogen retention in soil
J. Wei (2018), XXII, 160 pp
ISBN: 978-3-95806-299-3

Band / Volume 410
The impact of soil water distribution on root development and root water uptake of winter wheat
G. Cai (2018), xviii, 143 pp
ISBN: 978-3-95806-303-7

Band / Volume 411
Charakterisierung und Optimierung der Grenzfläche Elektrolyt/Kathode in metallgestützten Festelektrolyt-Brennstoffzellen
D. Udomsilp (2018), XI, 176 pp
ISBN: 978-3-95806-304-4

Band / Volume 412
Formation of Secondary Organic Aerosol from Photo-Oxidation of Benzene: a Chamber Study
S. H. Schmitt (2018), III, 250 pp
ISBN: 978-3-95806-305-1

Band / Volume 413
Mechanismen der chrombasierten Degradation von metallgestützten Festoxid-Brennstoffzellen
A. Beez (2018), VIII, 144 pp
ISBN: 978-3-95806-306-8

Band / Volume 414
Entwicklung eines Werkzeugs zur Modellierung der Nettoerosion im Hauptraum der Brennkammer eines Tokamaks und Studium der Plasma-Wand-Wechselwirkung an DEMO1
M. Beckers (2018), XIX, 150 pp
ISBN: 978-3-95806-307-5

Band / Volume 415
Fehlstellendotierung von Eisenoxid- und Bismutsulfid-Nanopartikeln
J. P. Mock (2018), v, 187 pp
ISBN: 978-3-95806-309-9

Band / Volume 416
Nanocrystalline Silicon Oxide in Silicon Heterojunction Solar Cells
A. Richter (2018), 166 pp
ISBN: 978-3-95806-310-5

Band / Volume 417
Gas-to-Particle Partitioning of Major Oxidation Products from Monoterpenes and Real Plant Emissions
G. Gkatzelis (2018), xii, 128 pp
ISBN: 978-3-95806-314-3

Band / Volume 418
The Dynamics of Electrons in Linear Plasma Devices and its Impact on Plasma Surface Interaction
M. Hubeny (2018), 141 pp
ISBN: 978-3-95806-316-7

Band / Volume 419
Tomographic reconstruction of gravity wave parameters from satellite-borne airglow observations
R. Song (2018), 136 pp
ISBN: 978-3-95806-317-4

Band / Volume 420
Reduktion von Edelmetallen in der Wasserstoffelektrode bei der Polymerelektrolyt-Wasserelektrolyse
P. Paciok (2018), VII, 187 pp
ISBN: 978-3-95806-320-4

Band / Volume 421
Mechanismen des Hochtemperaturrisswachstums in einem ferritischen Stahl an Luft und in Wasserdampf
T. Fischer (2018), VIII, 216 pp
ISBN: 978-3-95806-326-6

Band / Volume 422
Selbstheilende plasmagespritzte $Mn_{1,0}Co_{1,9}Fe_{0,1}O_4$-Schutzschichten in Festoxidbrennstoffzellen
N. Grünwald (2018), viii, 137 pp
ISBN: 978-3-95806-327-3

Band / Volume 423
Sonochemical Synthesis of Silicon Hydride Polymers and Silicon Nanoparticles from Liquid Silanes
A. P. Cádiz Bedini (2018), viii, 132, XVIII pp
ISBN: 978-3-95806-329-7

Weitere ***Schriften des Verlags im Forschungszentrum Jülich*** unter
http://wwwzb1.fz-juelich.de/verlagextern1/index.asp

Energie & Umwelt / Energy & Environment
Band / Volume 423
ISBN 978-3-95806-329-7

Mitglied der Helmholtz-Gemeinschaft

JÜLICH
Forschungszentrum